EXTENDED THREE-DIMENSIONAL ADCIRC HYDRODYNAMIC MODEL TO INCLUDE BAROCLINIC FLOW AND SEDIMENT TRANSPORT

A Dissertation

by

WAHYU WIDODO PANDOE

Submitted to the Office of Graduate Studies of
Texas A&M University
in partial fulfillment of the requirements for the degree of

DOCTOR OF PHILOSOPHY

May 2004

Major Subject: Ocean Engineering

EXTENDED THREE-DIMENSIONAL ADCIRC HYDRODYNAMIC MODEL TO INCLUDE BAROCLINIC FLOW AND SEDIMENT TRANSPORT

A Dissertation

by

WAHYU WIDODO PANDOE

Submitted to Texas A&M University
in partial fulfillment of the requirements
for the degree of

DOCTOR OF PHILOSOPHY

Approved as to style and content by:

Billy L. Edge (Chair of Committee)	Robert E. Randall (Member)
Hamn-Ching Chen (Member)	David A. Brooks (Member)
	Paul Roschke (Head of Department)

May 2004

Major Subject: Ocean Engineering

ABSTRACT

Extended Three-Dimensional ADCIRC Hydrodynamic Model
to Include Baroclinic Flow and Sediment Transport. (May 2004)
Wahyu Widodo Pandoe, B.S., Institut Teknologi Bandung;
M.S., Texas A&M University
Chair of Advisory Committee: Dr. Billy L. Edge

The objective of this research is to identify the circulation patterns of the water and sediment fluxes in coastal and estuarine zones, where the shoaling processes correlate with tide generating flow patterns. The research provides a better understanding of the characteristics of spatial and temporal variability of currents.

An important deviation from previous research is the inclusion of the baroclinic term, which becomes very important in density driven flows. The understanding of this process provides a basis for determining how the water circulation three-dimensionally controls the hydrodynamics of the system and ultimately transports the suspended and soluble materials due to combined currents and waves.

A three-dimensional circulation model is used to calculate the water circulation. The model is based on the three-dimensional (3D) version of Advanced Circulation (ADCIRC) Hydrodynamic Model with extending the Sediment Transport module. The model is based on the finite element method on unstructured grids. The output of the hydrodynamic model is used to estimate spatial and temporal advections, dispersions and bottom shear stress for the erosion, suspension, deposition and transport of sediment.

The model development includes extending the existing three-dimensional (3D) ADCIRC Model with (1) baroclinic forcing term and (2) transport module of suspended and soluble materials. The transport module covers the erosion, material suspension and deposition processes for both cohesive and non-cohesive type sediments. The inclusion of the baroclinic demonstrates the potential of over or underpredicting the total net transport of suspended cohesive sediment under influence of currents.

The model provides less than 6% error of theoretical mass conservation for eroded, suspended and deposited sediment material. The inclusion of the baroclinic term in stratified water demonstrates the prevailing longshore sediment transport. It is shown that the model has an application to the transport of the cohesive sediments from the mouth of the Mississippi River along the north shore of the Gulf of Mexico towards and along the Texas coast. The model is also applicable to determine the design erosion thickness of a cap for isolating contaminated dredged material and to evaluate the appropriate grain size of cap sediments to minimize the erosion.

DEDICATION

Alhamdulillaahi Rabbil 'aalamin,

To my lovely wife Iroh and daughter Nabila,

for their endless love, patience, support, and smiles,

and also to my parents drh. Pandoe Soebhono (Alm.) and Hj. Tietah Retnadhie.

ACKNOWLEDGMENTS

So many nice people I have encountered along the way finishing my Ph.D. dissertation. I am indebted to my advisor, Dr. Billy L. Edge, for his guidance, discussions and advice. This research would not be possible without the financial support and kindest assistance that he provided. I also would like to express my appreciation for his efforts in correcting my poorly written manuscripts. I want to thank my other committee members, Dr. Robert E. Randall, Dr. Hamn-Ching Chen and Dr. David A. Brooks, for their time, helpful discussions, comments, and suggestions on my research.

I sincerely would like to thank to Dr. Janet Sprintall of the Scripps Institution of Oceanography, San Diego, CA, for the partial financial support that she provided through part of a joint Indonesian-American oceanographic research program. My cordial gratitude and appreciation is addressed to Mrs. Lori Garcia, Mrs. Lois Peters and Mrs. Shirley Button for their administrative support, and also to Johnie Reed, Thomas Mather, and Ronnie Eichler who have always been available to help me out with any computer and technical problems.

It is impossible to thank everybody who assisted me through this study. I sincerely have to thank my colleague in Indonesia, Dr. Ridwan Djamaluddin, for his kind help. I also have to thank all of my friends here at the Ocean Engineering Program, Civil Engineering Department, and the Bryan/College Station Indonesian Student Association, who have made my studies at Texas A&M University enjoyable.

Appreciation is further extended to my colleagues at Baruna Jaya Research Vessels Group of BPPT-Indonesia, who carried out the various stages of research and surveys at sea. Finally, I must also thank my family for their encouragement, support, and their endless love, which has motivated me to complete the study.

The study described in this Ph.D. dissertation has been supported in part by the U.S. Environmental Protection Agency through the South and Southwest Hazardous Substance Research Center, the National Science Foundation, and the Texas Engineering Experiment Station at Texas A&M University.

TABLE OF CONTENTS

Page

LIST OF FIGURES

FIGURE Page

FIGURE Page

LIST OF TABLES

CHAPTER I

INTRODUCTION

1.1. Background of Study

Over the past several years, a large number of hydrodynamic numerical models have been reported. The basic theme is to provide robust and comprehensive hydrodynamic circulation and transport models for use in pursuit of specific, focused engineering and scientific investigations. Development of coastal engineering projects, such as coastal management, dredging work, coastal protection, ship channel maintenance and sustainable coastal development requires a detailed knowledge of the hydrodynamic circulation. Some numerical models based on the two- or three-dimensional models have been widely developed.

A 2D (two-dimensional) depth-integrated approach is often considered suitable to model hydrodynamic and scalar transport in a non-stratified estuary. The effect of vertical variability inherent to a barotropic flow may be parameterized in a transport simulation, but the effect of stratification is more complex and not well suited for parameterization. Thus, when stratification effects become important in an estuary, the depth-integrated model might not fully adequate to perform the model simulation.

Solving horizontal and vertical velocities three-dimensionally is necessary for explaining the variability of the current shear, which may alter the velocity distribution vertically. Three-dimensional solution of the hydrodynamic flow can explain the relationship between periodic tide and the currents within the area of study (Blain, 1999; Bijvelds et al., 1999). This may lead to an explanation of both divergence and convergence zones and corresponding depositional area (Gross, et al., 1999; Ribbe and Holloway, 2001).

The main concern for the models is the significant discrepancies between the model

---

This dissertation follows the style and format of the Journal of Ocean Engineering.

and data, especially for long-period run time models. Blumberg et al. (1999) suggested the need for accurate and detailed information on boundary conditions. Otherwise, he suggests, computed hydrodynamic parameters might be significantly different from the actual field condition. Therefore, model calibration is required using available data. In order to assess the performance of a numerical model, the results might be validated with field measurement and analytical solution.

The equation of motion shows that water moves in response to differences in pressure, which are generated by two factors: water surface slope (barotropic) and horizontal water density differences (baroclinic). The determination of baroclinic flow is important since it may cause a convergence zone, where the converging pressure gradients drive internal circulation patterns into a common point. A convergence zone represents a location where substances tend to remain for a longer period and may accumulate, allowing increased concentrations to develop in the water column and in the bed. The baroclinic term may also cause dissimilarities between ebb and flood tidal currents. The magnitude of bottom stress also related with the baroclinic term associated with the vertical current shear. The presence of the baroclinic-forced currents may strengthen the existence of the reverse estuarine flow.

The density field that drives the baroclinic force is determined from the salinity, temperature, and suspended sediment concentraton. For three-dimensional domain, the depth-integrated baroclinic might not be suitable for explaining the variability of vertical current shear, which mostly varies vertically. In the case of density stratification as a result of either little tidal action or large fresh-water (river) flow, the flow profile can be separated into two portions in the seaward regions of the tidal intrusion: (a) the upper part is the fresh water flow to seaward, and (b) the lower part is the saline water practically similar to the ocean, so called the ‘salinity wedge’. With the inclusion of the baroclinic term in the model development, the existence of salinity wedge may penetrate upstream in the river.

The sediment movement in an estuary depends on the hydrodynamic forcing caused by currents, wave, pressure gradient, and on the graviatational forces on a sloping bed. A general hydrodynamic circulation model may be useful in the development of density driven flows that may arise in the case of suspension of high-density materials. The shoaling process in a bay is presumed to correlate with the flow pattern around the channel driven by tide generating current and wind stress. Sediment conveyed by river runoff to the estuary might also be one of the sedimentation sources.

Long-term stability is an important issue in the dredging works. The capping material must be stable against excessive erosion and resuspension. Palermo et al. (1998) and Gailani et al. (2001) suggested the implementation of numerical modeling to evaluate the erosion potential of the dredging material placement. Combined effects of current and wave could potentially cause resuspension and erosion of the mound cap.

1.2. Purpose of Study

This research involves the basic development of a three-dimensional model for sediment and material transport. The development extends the existing three-dimensional (3D) hydrodynamic Advanced Circulation (ADCIRC) Model with (1) baroclinic forcing term and (2) transport module of suspended and soluble materials.

The purpose of this research is to implement the coupled hydrodynamic and transport numerical model system as a step toward a natural estuary and harbor configuration. Several idealized test cases were performed to test the robustness of the model. Comparison of the results to the analytical solutions was also assessed to satisfy the reliability of the developed transport model.

1.3. Study Objectives

The first objective of this research is to understand the characteristics of spatial and temporal variability of vertical current shears, which are expected to be associated with period of ebb and flood tidal cycles. The understanding of these processes can provide a basis for determining how the three-dimensional water circulation controls the hydrodynamics of the system.

The second objective of this research is to implement and expand the hydrodynamic numerical modeling system to accommodate the density driven flows and estimate the contribution of the baroclinic term in the three-dimensional ADCIRC hydrodynamic model for coastal and estuarine systems. Thirdly, this research is to identify the circulation patterns of the water and sediment fluxes in an estuarine zone. Suspended materials in the water column are highly related to the hydrodynamic circulation. The interface of the salinity wedge or a convergence zone has been shown to be related to the presence of deposition of sediment (Van Rijn, 1993; Ippen, 1966; van Ledden, 2003). The sediment transport mode is limited to suspended sediment for cohesive and non-cohesive types. No bed-load transport has been incorporated and formulated in the research. The presence of suspended sediment in the water column will also increase the bulk density of the suspension. Thus, assessment of the erosion, transport and deposition of sediments will be coupled with the inclusion of baroclinic terms.

1.4. Advanced Circulation (ADCIRC) Hydrodynamic Model

The model used is the Advanced Circulation Model (ADCIRC) originally developed in the early 1990's (Luettich et al., 1992). ADCIRC is a two and three dimensional finite element model used for hydrodynamic circulation problems. The model is based on the finite element codes that solve the shallow water equation on unstructured grids. The finite element formulation has the advantage of flexibility in resolution over the area domain. Fine resolution can be specified locally to meet the accuracy requirements, and coarse resolution can be implemented in areas distant from the region of interest.

Grenier et al. (1995) studied a comparison between the two-dimensional depth-integrated (2DDI) and three-dimensional (3D) ADCIRC models. The ADCIRC 2DDI is a two-dimensional depth-integrated model that solves sea surface elevation η and depth-averaged velocity U and V. The model has been successfully implemented for estuaries, tidal inlets, navigation channel, harbor embayments, and many other coastal problems.

The three-dimensional model, ADCIRC 3D, applies a mode-splitting technique to solve the vertical profile of horizontal velocity (Luettich and Westerink; 1992; Luettich et al., 1994). This model is called a velocity solution or VS version, which completes the model for solving three-dimensional flow fields *u*, *v* and *w*.

Muccino et al. (1997) reported the development of methods for solving vertical velocity using the adjoint method. Their results are consistent with the analytical solutions. However, the elevation and horizontal velocity applied to compute the vertical velocity were obtained from the three-dimensional diagnostic model FUNDY5. In this research, the adjoint method is implemented in ADCIRC 3D-VS model for solving the vertical velocity.

1.5. Research Method

To achieve the objectives, it is required to extend the existing ADCIRC source code, which was originally written in Fortran code. Analytical and empirical comparisons are adequate for validation of the newly generated ADCIRC model. A newly developed 3D ADCIRC-Transport model integrates the hydrodynamic and transport modules. A schematic diagram of the integrated hydrodynamic-transport model is presented in Figs. 1.1 and 1.2. The input files for model setup and its output files are given in Appendix A.

The hydrodynamic module computes velocity fields *u*, *v* and *w*, and sea level η. The transport module does the computation of soluble and suspended sediment transport, density change, which is based on the change of salinity, temperature and sediment concentration in the water column, and determines the baroclinic forcing term. The computed baroclinic forcing is then fed back to the hydrodynamic module.

The sediment transport module covers both cohesive and non-cohesive types of sediments. It determines the change with time and spatially dependent variables: occurring erosion and deposition, the concentration of suspended sediment in the water column, and the depth change. Then, the occurring depth change is applied as a new depth in the hydrodynamic module. Unfortunately, the wetting-drying capability is not yet available in extended 3D ADCIRC-Transport model.

The study modifies and extends the existing 3D ADCIRC Hydrodynamic codes to include baroclinic and sediment transport modules. All numerical work was performed

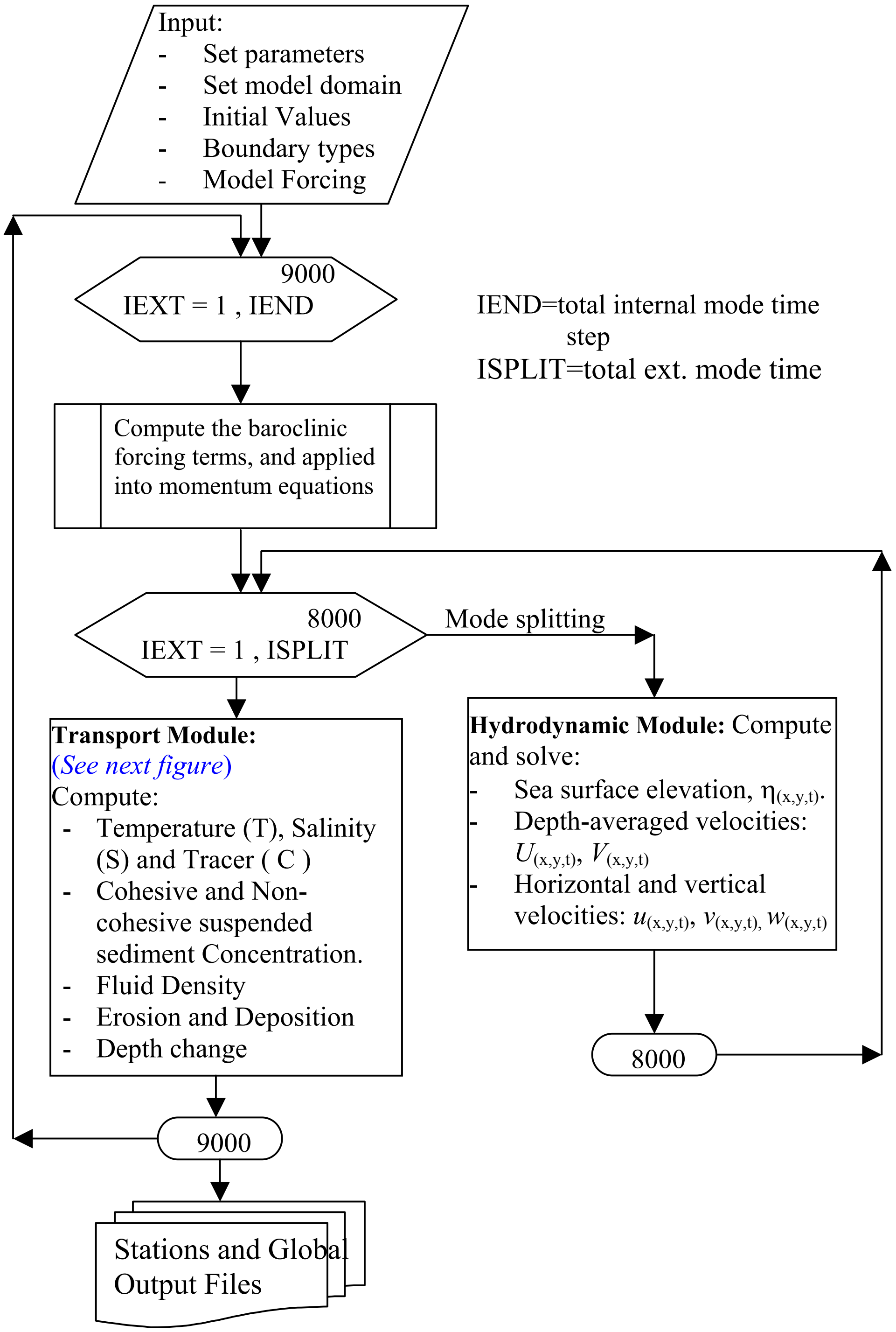

Fig. 1.1. Diagram of hydrodynamic module including the implementation of the baroclinic forcing term.

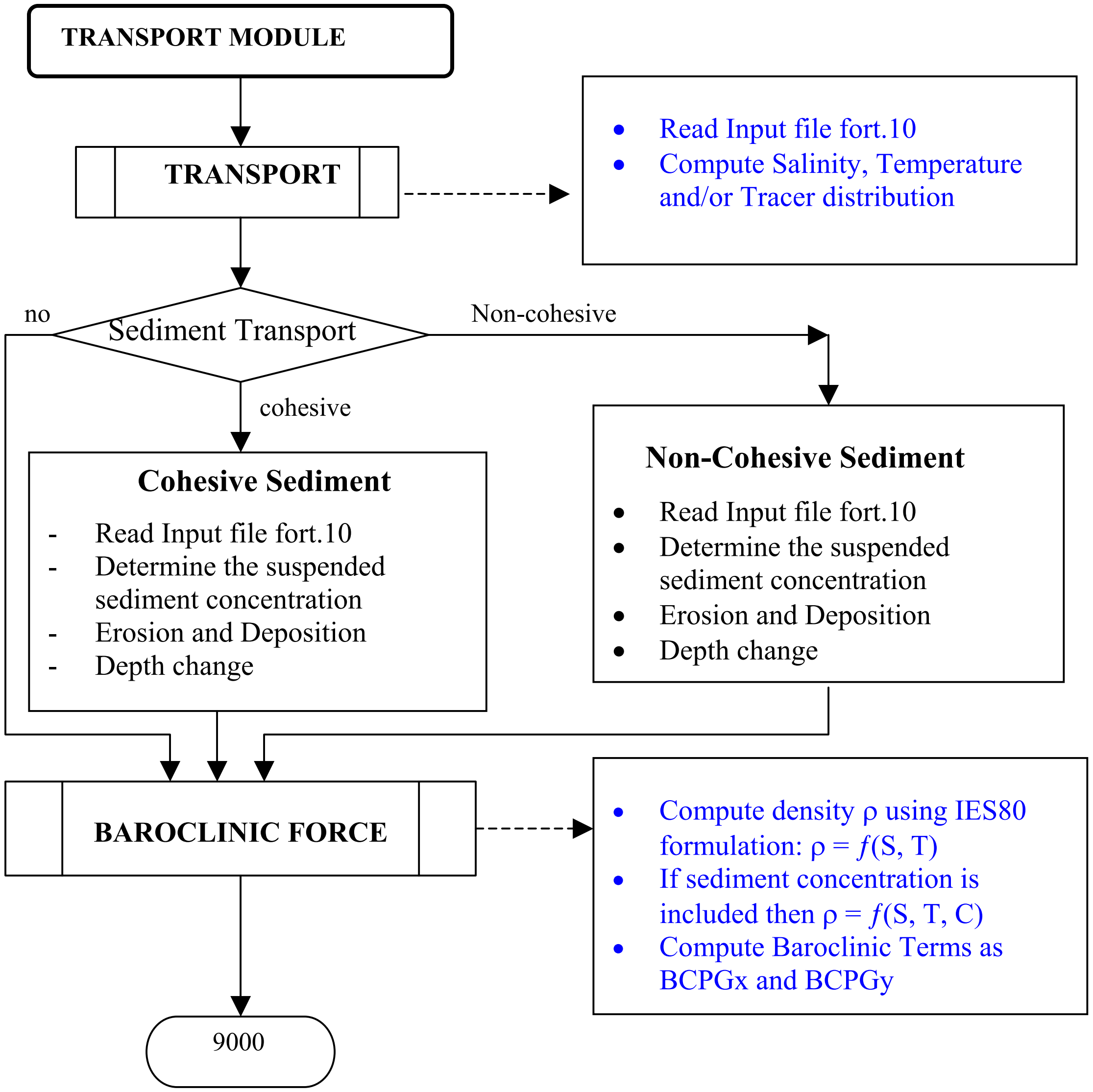

Fig. 1.2. Diagram of transport module including the implementation of the baroclinic forcing term.

in FORTRAN programming code. Pre-processing, model setup and grid generation were done in Surface Water Modeling System version 8.0 (SMS 8.0) software. Post processing of the model results was carried out using SMS 8.0 and MATLAB programming language code to include 2D and 3D displays and movie generation. All movies are saved in AVI video file format.

1.6. Scope of Research

The scope of work in this study includes a basic development of the hydrodynamic-transport model. The model results are compared to analytical and empirical formulations adopted from literature or other research results. Several idealized test cases simulating various real conditions were developed. No real estuary or coastal case was performed due to difficulties obtaining the observational or laboratory data. Those idealized cases are selected to test the model, including the quarter annular test problem (QATP), rectangular basin, barred rectangular channel, trenched channel, river-ocean system, tidal inlet and dredging disposal cap cases.

The assessment of the existing 3D-hydrodynamic module will be reviewed in Chapter II. For model verification, the computed velocity components from the model are compared to the analytical solution using a widely used test case domain called Quarter Annular Test Problem (QATP).

Chapter III discusses the three dimensional finite element formulations for the soluble material and tracer transport, such as salinity, temperature, soluble and suspended material concentration and water density. The basic approach of the baroclinic forcing terms is formulated from the computed density distribution. The dam break test problem demonstrates the successful implementation of the baroclinic terms into the momentum equations. The existing empirical formulation of arrested saline wedge verifies the implementation of the baroclinic forcing in the numerical model in an idealized riverine domain.

Several 3D sediment transport formulations are available from many sources and the literature. The selected formulations for both cohesive and non-cohesive sediment transport are applied to the numerical model. Chapter IV covers the complete formulations and implementation into the finite element model. Assessment of conservation of mass and verification with the analytical model are also performed to satisfy the model results.

In Chapter V, three idealized cases simulate the basic application of the developed sediment transport model including the baroclinic terms. Those idealized test cases include (a) riverine, (b) tidal inlet, and (c) dredging-cap. Chapter VI analyzes and discusses the model and simulation results, and Chapter VII completes the study with conclusions and recommendations.

CHAPTER II

THREE-DIMENSIONAL HYDRODYNAMIC MODEL

This study was performed using the ADCIRC 3D-VS circulation model that includes both two-dimensional depth integrated and three-dimensional solutions. The 3D-VS model is one version of the ADCIRC 3D that requires discrete representation of the horizontal velocity and so-called velocity solution or VS (Grenier et al., 1995). The mathematical model of hydrodynamic circulation in coastal water is based on the three-dimensional Navier-Stokes equations. The detailed explanations of the model are given in Luettich et al. (1992) and Luettich and Westerink (2003).

The quarter annular test problem (QATP) is used for a test case of comparison between ADCIRC 3D model and analytical solutions.

2.1. Overview of the Three-Dimensional Hydrodyamic ADCIRC Model (ADCIRC 3D-VS)

The computation of hydrodynamics is performed in a bottom and surface-following "σ" coordinate system shown in Fig. 2.1, in which:

$$\sigma = a + \frac{(a-b)(z-\eta)}{H} \tag{2.1}$$

$$x_\sigma = x$$

$$y_\sigma = y$$

where: $\sigma = a = 1$ at the free surface and $\sigma = b = -1$ at the bottom; $H = h + \eta$ = total water depth to the free surface; h is a bathymetric depth; and η is a free surface elevation relative to the geoid.

In this three-dimensional circulation model, the vertical finite element domain will be divided into a number of σ-layers ranging from –1 at the bottom to 1 at the surface. In some cases, high gradients may occur at the bottom and surface, thus normally the vertical grids have more layers around the bottom and surface than that of the mid column;

however, for the non-cohesive sediment transport model the uniformly distributed vertical layers are more likely to be used for model stability.

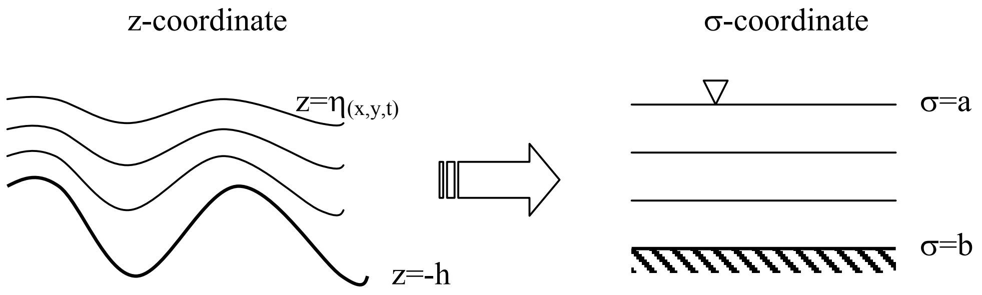

Fig. 2.1. Transformation from z-coordinate to σ-coordinate system.

The sigma coordinate system is probably appropriate in dealing with significant topographic variability such as that generally encountered in estuarine, continental shelf breaks and sloped bottom (Mellor, 1998; Blumberg et al., 1999). The σ-coordinate system has the same number of layers under each horizontal grid point regardless of the depth; therefore, some numerical problems with adding or subtracting layers can be reduced. The σ coordinate system is suitable for coastal and estuarine modeling as long as the transition from shallow water to deep water is gentle.

The applied chain rules that relates derivatives in the level (z) coordinate reference system to derivatives in the stretched (σ) coordinate system are given as follow:

$$\frac{\partial}{\partial x_z} = \frac{\partial}{\partial x_\sigma} - \left[\frac{(\sigma-b)}{(a-b)}\frac{\partial \eta}{\partial x_z} + \frac{(\sigma-a)}{(a-b)}\frac{\partial h}{\partial x_z} \right]\frac{\partial}{\partial z} \tag{2.2}$$

$$\frac{\partial}{\partial y_z} = \frac{\partial}{\partial y_\sigma} - \left[\frac{(\sigma-b)}{(a-b)}\frac{\partial \eta}{\partial y_z} + \frac{(\sigma-a)}{(a-b)}\frac{\partial h}{\partial y_z} \right]\frac{\partial}{\partial z} \tag{2.3}$$

$$\frac{\partial}{\partial z} = \frac{(a-b)}{H}\frac{\partial}{\partial \sigma} \qquad ; \; H \equiv h + \eta \tag{2.4}$$

$$\int \partial z = \frac{H}{a-b}\int \partial \sigma \tag{2.5}$$

2.1.1. Solving Sea Level η and Depth-averaged Velocity U and V

Water surface elevation is solved in a vertically integrated continuity equation utilizing the GWCE (Generalized Wave Continuity Equation) formulation. The modified GWCE is derived as a summation of the time derivative of the continuity equation and the spatial gradient of the momentum equations. The GWCE is used to solve the sea level elevations (Luettich et al., 1992).

$$\frac{\partial \eta}{\partial t}+\frac{\partial (UH)}{\partial x}+\frac{\partial (VH)}{\partial y}=0 \qquad (2.6)$$

where U and V are depth-averaged velocities, with:

$$U_{(x,y,t)}=\frac{1}{H}\int_{-h}^{\eta} u(z)\,dz \ = \text{depth-averaged } x\text{-horizontal velocity}$$

$$V_{(x,y,t)}=\frac{1}{H}\int_{-h}^{\eta} v(z)\,dz \ = \text{depth-averaged } y\text{-horizontal velocity}$$

The linearized GWCE is given in Hagen et al. (2001) and Luettich et al. (1992) as:

$$\frac{\partial^2 \eta}{\partial t^2}+\tau_o\frac{\partial \eta}{\partial t}-g\left[\frac{\partial}{\partial x}\left(H\frac{\partial \eta}{\partial x}\right)-\frac{\partial}{\partial y}\left(H\frac{\partial \eta}{\partial y}\right)\right]-(\tau-\tau_o)\left[\frac{\partial (UH)}{\partial x}-\frac{\partial (VH)}{\partial y}\right]=0 \qquad (2.7)$$

where τ_o is a weighting parameter in the GWCE that controls the portion of the primitive continuity. GWCE becomes primitive continuity as $\tau_o \rightarrow \infty$, and GWCE becomes pure wave equation as $\tau_o \rightarrow 0$.

2.1.2. Horizontal Velocity Components: u(z) and v(z)

The three-dimensional version of ADCIRC applies the non-conservative form of the momentum equations to solve horizontal velocity *u* and *v*. The free surface elevation as described in Eq.2.6 is solved by substituting the vertically-integrated momentum equations into the continuity equation to form the GWCE. The momentum equations applied in ADCIRC-3D are:

$$\frac{\partial u}{\partial t}+u\frac{\partial u}{\partial x}+v\frac{\partial u}{\partial y}+\omega\left(\frac{a-b}{H}\right)\frac{\partial u}{\partial \sigma}-fv=-g\frac{\partial \eta}{\partial x}+m_{x_\sigma}-b_{x_\sigma}+\left(\frac{a-b}{H}\right)\frac{\partial}{\partial \sigma}\left(\frac{\tau_{zx}}{\rho_0}\right) \qquad (2.8a)$$

$$\frac{\partial v}{\partial t}+u\frac{\partial v}{\partial x}+v\frac{\partial v}{\partial y}+\omega\left(\frac{a-b}{H}\right)\frac{\partial v}{\partial \sigma}+fu=-g\frac{\partial \eta}{\partial x}+m_{y_\sigma}-b_{y_\sigma}+\left(\frac{a-b}{H}\right)\frac{\partial}{\partial \sigma}\left(\frac{\tau_{zy}}{\rho_0}\right) \tag{2.8b}$$

where u and v are velocities in the x- and y- direction; ω is vertical velocity in σ-coordinate; f is the Coriolis force; g is the gravity acceleration; $m_{x\sigma}$ is a combined horizontal diffusion/dispersion momentum; $b_{x\sigma}$ and $b_{y\sigma}$ are baroclinic pressure term in x- and y-directions; τ_{zx} and τ_{zy} are components of vertical shear stress; and ρ_o is a reference density of water.

Velocities are determined from the non-conservative form of the momentum equation. The solution strategy for solving horizontal velocities u and v in Eqs. (2.8a,b) includes finite element method for spatial and finite difference for temporal. The vertical grid nodes are defined vertically at each horizontal node, thus the horizontal and vertical integrations can be performed independently. The detail of the 3D-VS formulations is given in Luettich and Westerink (2003).

2.1.3. Solving Vertical Velocity, w(z)

Vertical velocity is solved by the first derivative approach with the adjoint correction. Pandoe and Edge (2003) solved for ω in σ-coordinate, with essential boundary condition $\omega = 0$ at $\sigma = \mathrm{b}$, and natural boundary condition $\delta\omega=0$ at $\sigma=\mathrm{a}$:

$$\omega_{k+1}-\omega_k=-\frac{1}{(a-b)}\int_k^{k+1}\left(\frac{\partial \eta}{\partial t}+\frac{\partial(u\,H)}{\partial x}+\frac{\partial(v\,H)}{\partial y}\right)\partial\sigma \tag{2.9}$$

where k is a node number over vertical elements. The solution ω_k will satisfy the bottom boundary condition only. In order to satisfy the free surface, the adjoint correction is applied to Eq. (2.9) based on Luettich and Muccino (2001) and Muccino et al. (1997).

$$\omega_{adj}=\omega_\sigma-\omega_\sigma(\eta)\left[\frac{(\sigma-b)+\dfrac{HL}{a-b}}{(a-b)+\dfrac{2HL}{a-b}}\right] \tag{2.10}$$

where $\omega_\sigma(\eta)$ is the misfit of surface boundary condition at the free surface η, and L is the weight of the relative contribution of the boundary conditions versus the interior solution. The value L=0 is applied to the resulting ω_σ which is equal to adding a linear correction to the 1st order derivative equation that satisfies only the bottom boundary condition ($\omega_\sigma = 0$ at $\sigma = \text{b}$). This adjoint correction will give the solution exactly at the surface boundary condition, which in this case $\omega_{adj} = 0$ at $\sigma = \text{a}$.

The corresponding conversion of vertical velocity from sigma-level (ω) to z-level (w) is also given by Luettich and Muccino (2001):

$$w = \omega + \left(\frac{\sigma - b}{a - b}\right)\frac{\partial \eta}{\partial t} + u\left[\left(\frac{\sigma - b}{a - b}\right)\frac{\partial \eta}{\partial x} + \left(\frac{\sigma - a}{a - b}\right)\frac{\partial h}{\partial x}\right] + v\left[\left(\frac{\sigma - b}{a - b}\right)\frac{\partial \eta}{\partial y} + \left(\frac{\sigma - a}{a - b}\right)\frac{\partial h}{\partial y}\right] \quad (2.11)$$

The approach of computation follows three main steps: (1) compute the ω in σ-coordinate system; (2) apply adjoint correction in σ-level; and (3) transform ω from σ-coordinate into w in z-coordinate system. One may obtain vertical velocity solutions in either σ-coordinate or z-coordinate systems. The need of having vertical velocity solution in σ-coordinate is very important in the newly extended 3D-VS model that will be incorporated in the transport module.

2.2. Model Verification (QATP Case)

One example case is discussed here for model verification. The QATP (Quarter Annular Test Problem) case includes analytical solutions where the formulations are provided in the appendices of Muccino et al. (1997) and Luettich et al. (2002). The model was driven by one tidal component, the M2 periodic boundary forcing, with the amplitude of 0.1m. The quarter annular harbor (QATP) has a quadratic bathymetry as shown in Fig. 2.2. The results obtained from the ADCIRC model are compared to the analytical solution, as Luettich et al. (2002) investigated similar test case to another model, FUNDY5.

The QATP grid, which was generated using the SMS (Surface-water Modeling System) version 8.0, consists of 825 nodal points and 1536 triangular elements. The open boundary, located at r_2 =100km, is defined along the outer perimeter with uniform depth of 62.5m, and with 33 open boundary nodes. This boundary is forced by an M2 tide with frequency ω=1.40518917083x$10^{-4}$$\text{s}^{-1}$ and amplitude of 0.1m. One land boundary is also defined along the inner perimeter at r_1 =40km and both lateral boundaries θ=0 and θ=π/2. This land boundary consists of 81 land boundary nodes. ADCIRC allows an optional internal boundary with no normal flow as an essential boundary condition and allowing free tangential slip.

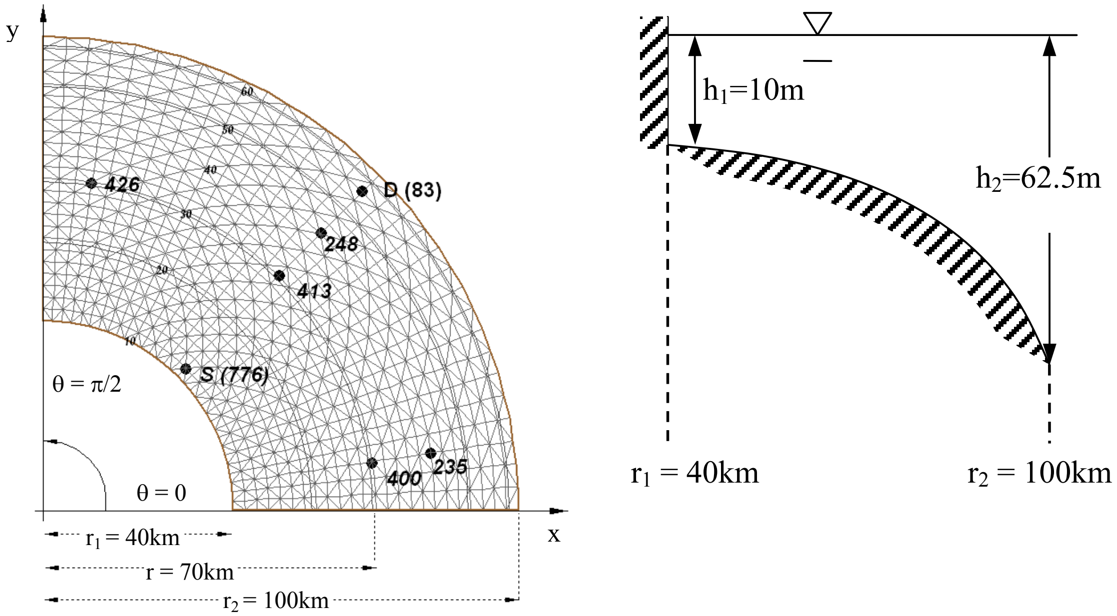
(a) Top view

(b) side view

Fig. 2.2. The quarter annular test problem (QATP) domain. (a) Top view of QATP elements grid. Open boundary is defined at $r=r_2$, and closed boundaries are at $\theta=0$, $\theta=\pi/2$ and $r=r_1$. Black nodes indicate selected points of interest. (b) Side view of QATP with minimum and maximum depths 10m and 62.5m, respectively. The bottom profile follows quadratic bottom.

For the vertical configuration of the QATP case, a slip bottom boundary condition is applied, thus u_b and v_b become non-zero. The selected free surface roughness is 0.0001, and the bottom roughness is 0.0015, both constant horizontally. The Coriolis force is neglected in all cases discussed in this chapter to avoid flow deviation in radial directions. Finite element vertical grid contains 9 nodes vertically at σ-values from bottom-up: -1.0, -0.87, -0.71, -0.5, 0.0, 0.5, 0.71, 0.87, and 1.0.

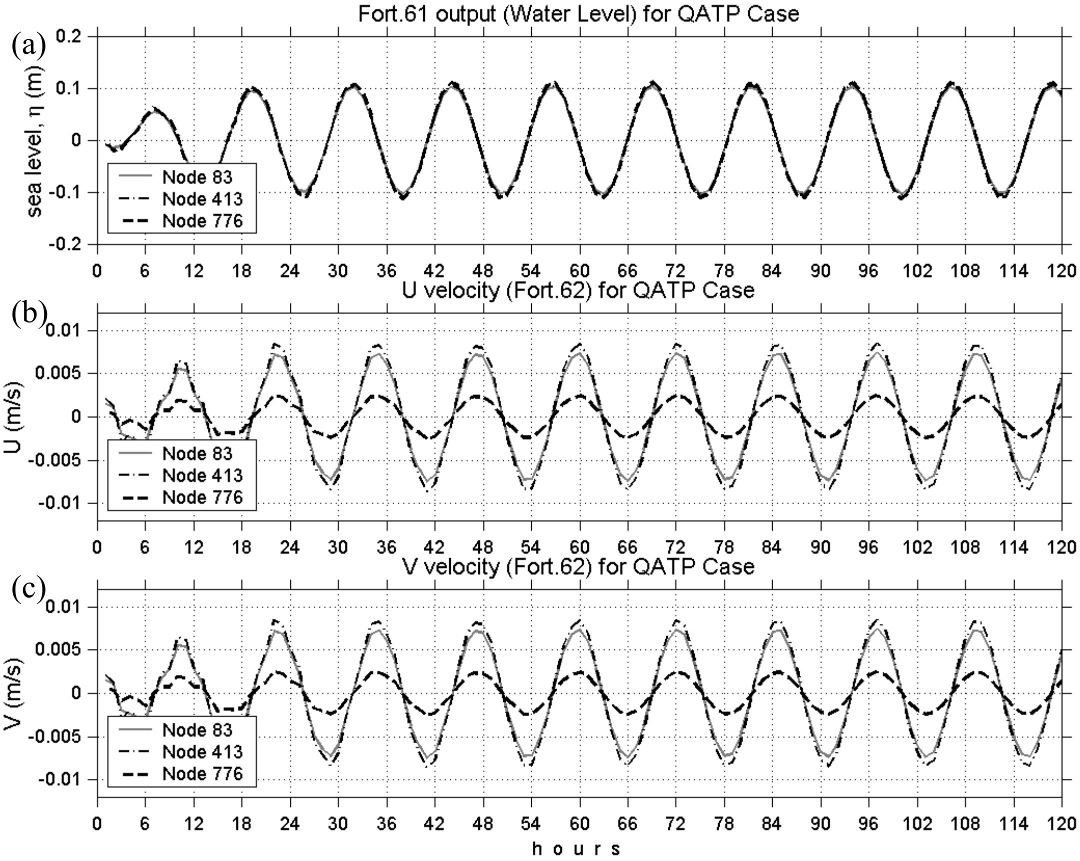

Fig. 2.3. Plot of (a) sea level height, η, (b) depth-averaged velocity U, and (c) depth averaged velocity V, for three selected points along radial direction: 83, 413 and 776.

Fig. 2.3 depicts the sea level height and normal components of depth-averaged velocity U and V from the deeper node (83) through the mid node 413 to the shallower node (776) for 5 days simulation. The model applies a one-day ramp function, thus the first 24-h plots should not be fully considered. Tidal heights are fairly uniform across the domain; with the shallowest node having a slightly higher tide. Maximum current occurs in the middle of the domain, in this case at r=70km (node 413), which is consistent with the conservation of mass for the flow propagating into the shallower water. The minimum current at node 776 is caused by the effect of the no-flow lateral boundary along the inner quarter circle of the domain.

The 3D-ADCIRC hydrodynamic model allows selection of the vertical eddy diffusivity (D_v) formulation. The simulation was performed in two cases based on the selected models of eddy viscosity: (1) the eddy viscosity remains constant vertically over the water depth (Lynch and Officer, 1985), and (2) the eddy viscosity is computed using a 2.5 Turbulence Closure Model (Mellor and Yamada, 1982; Blumberg and Mellor, 1987); herein after referred to as LO and MY, respectively. Appendix C provides the LO's formulation.

The LO vertical eddy diffusivity applied here; and also to be applied to the analytical solution; is assumed vertically uniform at each particular water depth and time invariant given as:

$$D_v = \Omega\, h^2 \tag{2.12}$$

where Ω is a constant for a specific parameter setup. For selected $\lambda = 9.206 + 9.206i$ and K = 2.836 (Muccino et al., 1997), the computed value for $\Omega = 0.829 \times 10^{-6}$ rad/s. The model solution over the incoming angle direction of the normal flow is very consistent. Fig. 2.4 shows a simulation of QATP case with a quadratic bottom (Fig. 2.2), herein after referred to as QATP-QUAD. The model applies linear slip bottom boundary condition formulated in Appendix C. The figure represents a time series of vertical profile of normal horizontal velocity over one semidiurnal tidal period (~12h) taken at node 400 with $\theta = 45°$ and node 413 with $\theta = 8.6°$. The plots is started at t = 88h during the water slack at low tide. Maximum flood tide occurs three hours later at t=91h, and maximum ebb tide occurs at t = 97h. The plots exhibit nearly coincidence solutions between those two points indicating that the normal flow solutions are uniformly in and out the domain independent on θ.

Nearly in all phases of tidal period, the vertical profiles close to the bottom of normal velocity exhibit a deviation profile from a logarithmic profile indicated by a bulged curve at near the bottom. The cause of the bulge is not clear, and Fredsoe and Deigaard (1992) suggest that those deviations are related to the selection of vertical eddy diffusivity. During one semidiurnal tide oscillation, the near bottom deviation curve tends to be insignificant at maximum flood and ebb tidal current (i.e. at t=91h and t=97h).

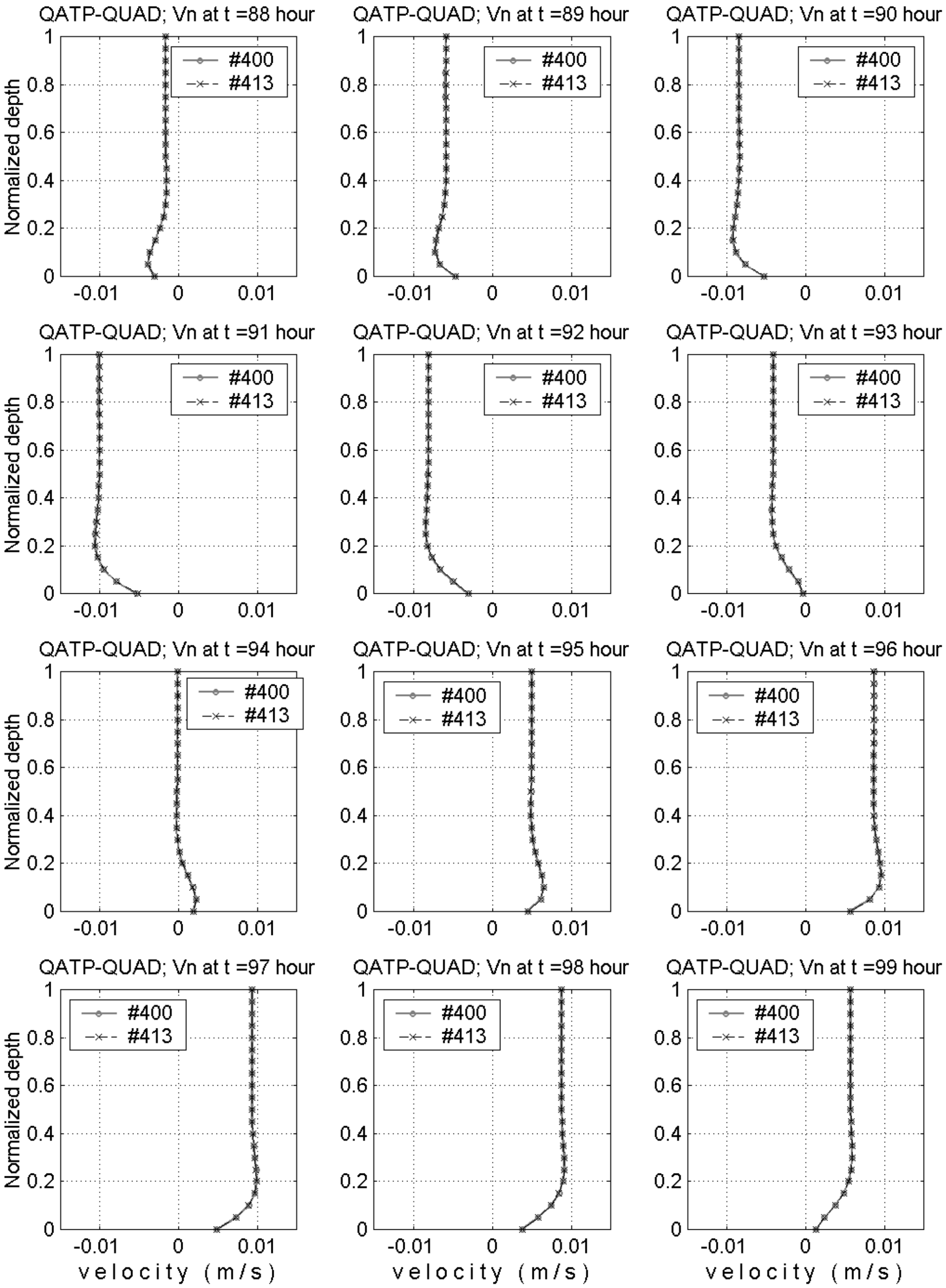

Fig. 2.4. One-tidal period plots of the normal-horizontal velocity computed with Lynch-Officer (LO) formulation at nodes 400 and 413. The plots are presented every one hour starting from t=88-h.

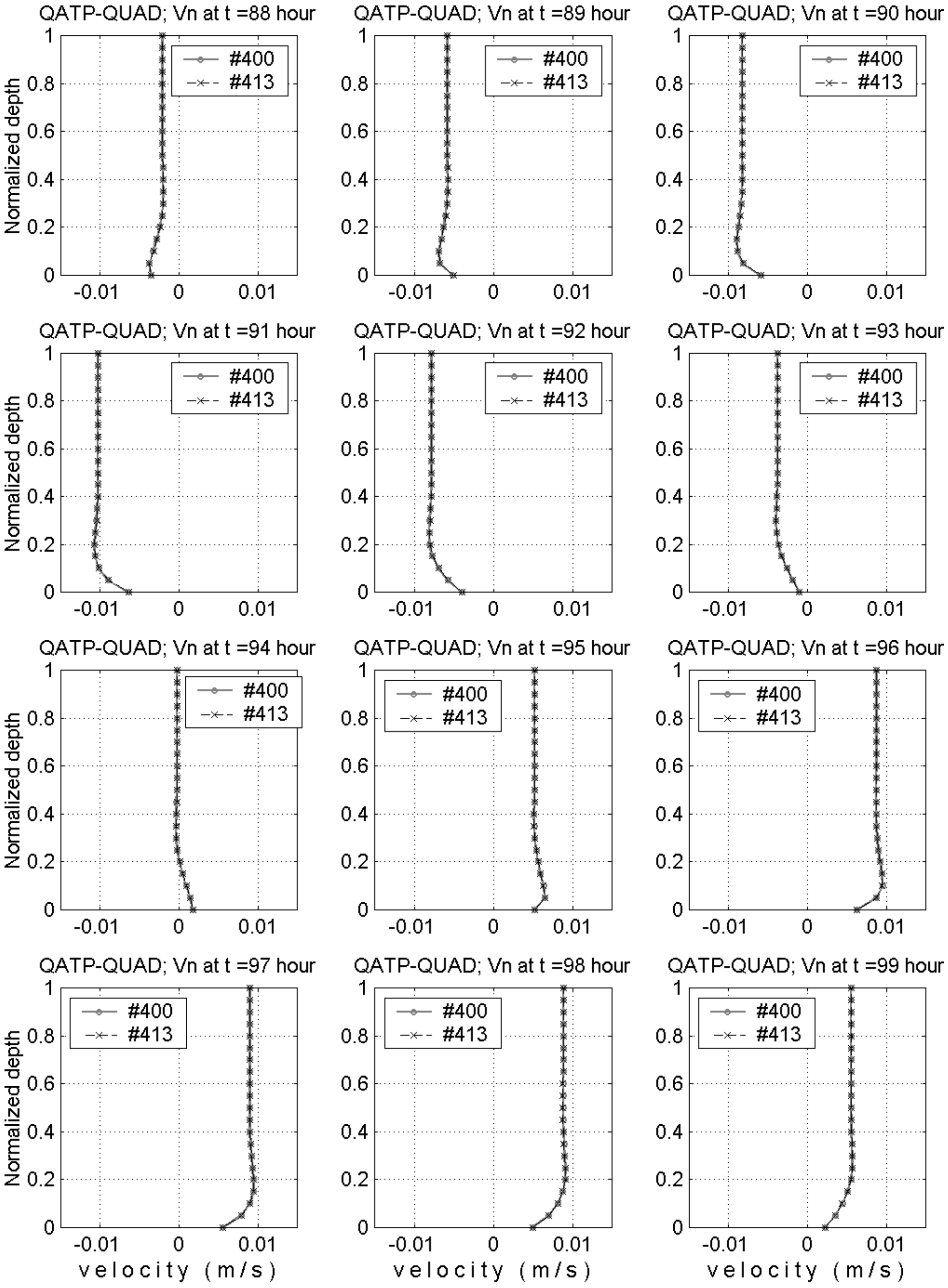

Fig. 2.5. One-tidal period plots of the normal-horizontal velocity computed with Mellor-Yamada (MY) formulation at nodes 400 and 413. The plots are presented every one hour starting from t = 88h.

Thus, the curve seems related to the transition of velocity from zero at bottom to some value at the mid layers and above. It is known that such turbulence flow occurs at near bottom layers, thus the effect of turbulence must be taken into account to determine the vertical eddy diffusivity, and the use of uniform eddy viscosity is not fully adequate to solve the velocity at near bottom layers.

Another simulation, similar to the previous case, was also performed with the MY vertical diffusivity formulation as shown in Fig. 2.5. The simulation applies a quadratic slip bottom boundary condition with C_d=0.0025. The vertical profiles of normal velocity are nearly similar to the LO profiles with smaller bulge at the near bottom solutions. The little bulge profile near the bottom is still present, but in this case it is more clearly seen the cause of those deviated bulge profiles, which is associated with the transition of the current profile from ebb to flood tide, and vice versa. Once the tidal current reaches its maximum at t = 91h (flood) and t = 97h (ebb), the vertical profiles become closer to the logarithmic profile, as expected. Thus, the choice of either LO or MY formulations seem fairly consistent and appropriate to develop a smooth vertical profile of horizontal velocity.

The results of the three dimensional velocity components obtained from QATP are compared to the analytical solution given in Lynch and Officer (1985) and Muccino et al. (1997). See Appendix C. The profiles are obtained at two instant in the tidal cycle with parameter set $\lambda = 9.206 + 9.206\,i$ and K = 2.836, similar to a set of parameter given in Muccino et al. (1997). Four points are selected in the QATP grid: #235 (r = 82.5 km, θ = 8.4°), #248 (r = 82.5 km, θ = 45°), #400 (r = 70 km, θ = 8.4°), and #413 (r = 70 km, θ = 45°). See Fig. 2.2 for node locations. The analytical solution assumes that the applied vertical eddy diffusivity is depth dependent and time independent. For comparison against the analytical solution, the results of numerical model being compared here is the first case previously discussed with LO vertical eddy diffusivity scheme given in Eq. 2.12.

The normal component of horizontal velocity solution u and v obtained from ADCIRC 3D-VS model, as shown in Fig. 2.6., is in fair agreement with the analytical solution except the near bottom, where the numerical solution gives slightly larger horizontal velocities than the analytical. This is probably because of the different approach applied in the solution. The numerical solution computes horizontal velocity solution from momentum equations in Eqs. 2.8a,b by integrating from bottom up in the discretized form of finite element method (Luettich and Westerink, 2003), while the analytical solution solves horizontal velocity solution directly from the linearized horizontal momentum equation in periodic form. During low tide (t = 88h) smaller deviations are observed in near bottom solutions, but during nearly zero tide (maximum flood tide) larger deviations between the two solutions are observed in the order of 10^{-4} m/s.

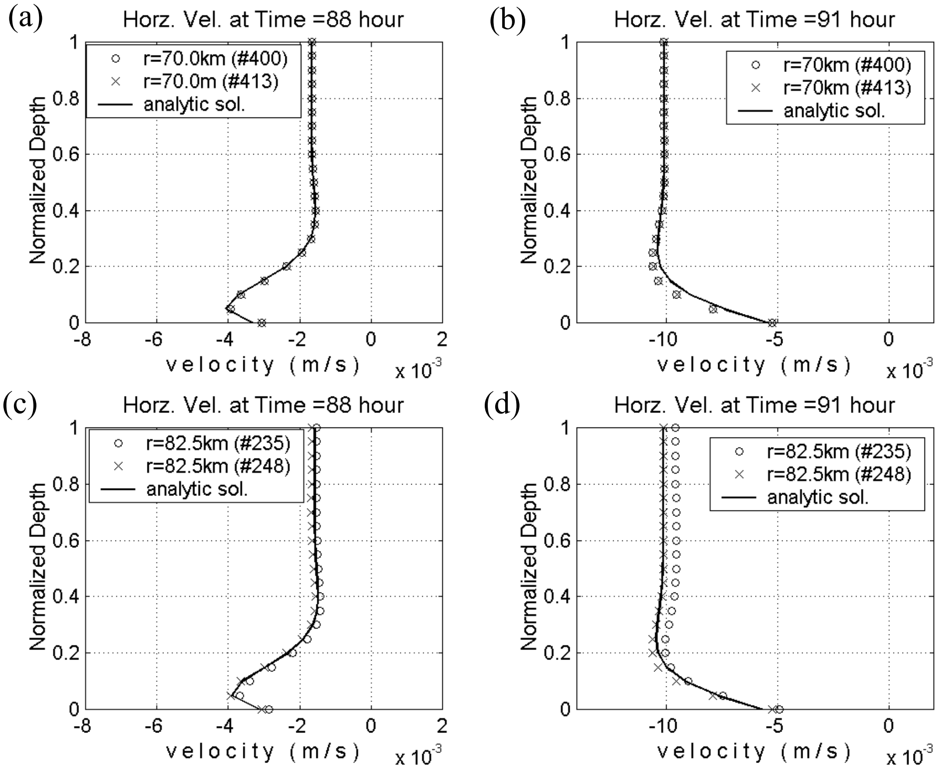

Fig. 2.6. Snapshot of amplitude of horizontal velocity solutions taken at t = 88h (water slack at low tide) and t = 91h (maximum flood tide at nearly zero tide level). The numerical solutions are compared with the analytical solutions: (a) at r = 70km, t = 88h; (b) at r = 70km, t = 91h; (c) at r = 82.5 km, t = 88h; (d) at r = 82.5km, t = 91h.

The numerical solution for the nodes at $\theta = 8.4°$ and 45° for both r = 70 km and r = 82.5 km give nearly similar solution indicating again that the solution is independent on θ. They differ up to $1\text{x}10^{-4}$m/s, indicating that consistent solutions have been fairly achieved.

Corresponding to the normal component of horizontal flow, the time series of vertical profiles of vertical velocity (w) over one tidal period taken at r=70km at node 400 with θ = 45° and node 413 with θ = 8.6° are given in Fig. 2.7 and 2.8 for LO and MY eddy diffusivities, respectively. The plots are started at t = 88h during the slack at low tide and indicate nearly zero vertical velocity at the surface. Maximum upward vertical velocity occurs three hours later during flood tide at t=91h, and maximum downward vertical velocity during ebb tide at t = 97h. The plots reveal consistent solutions between those two selected points indicating that the vertical velocity solutions are independent of θ.

Similar to the results on the horizontal velocity solution, the selection of either LO or MY exhibits fairly similar approximation of vertical velocity profiles. The profiles of mid layers and above seem not significantly different. The non-zero surface vertical velocity traces the oscillation of free surface boundary conditions associated with the sea surface tidal cycle.

Comparisons between analytical and numerical solutions of vertical velocity for QATP are represented at four nodes: nodes 400 and 413 (both at r=70km), and nodes 235 and 248 (both at r=82.5km) as shown in Fig.2.9. The plots are at the start of one tidal cycle at t = 88h (i.e. tidal current ≈ 0), and at maximum tidal current t = 91h (i.e. $\eta \approx 0$). Although the numerical solution indicates a slightly higher value than the analytical in the order of 10^{-6} m/s, in general the solution is in good agreement with the analytical solution. At the beginning of the tidal cycle, near the bottom, the numerical solution provides a lower velocity, which might be caused from the misfit of horizontal velocity solutions. Luettich et al. (2002) suggested another contribution to the vertical velocity deviation due to technique applied in the vertical velocity solution.

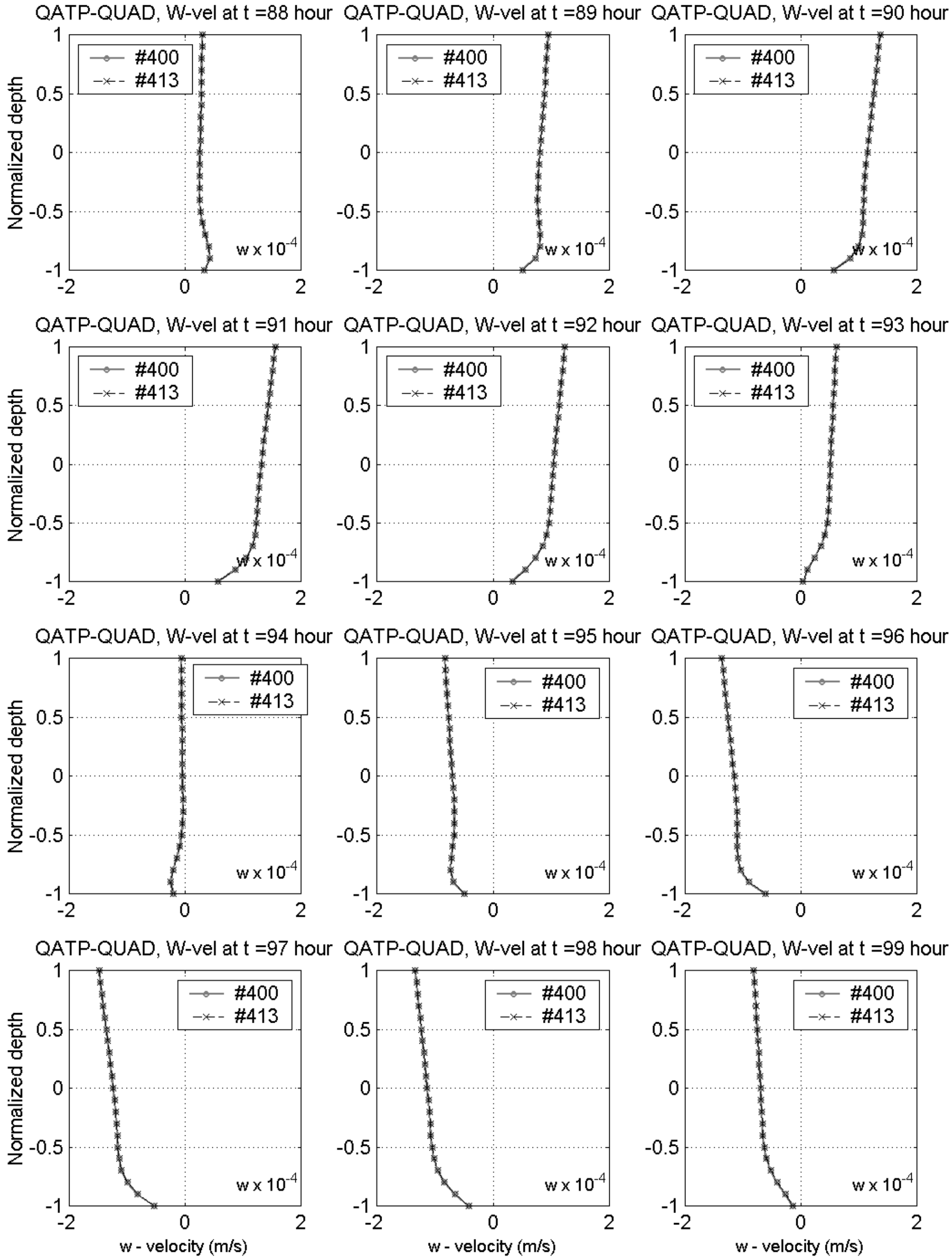

Fig. 2.7. One-semi diurnal tidal period plots of the vertical velocity, *w*, computed with Lynch-Officer (LO) vertical eddy diffusivity at nodes 400 and 413. The plots are presented every one hour starting from t = 88h.

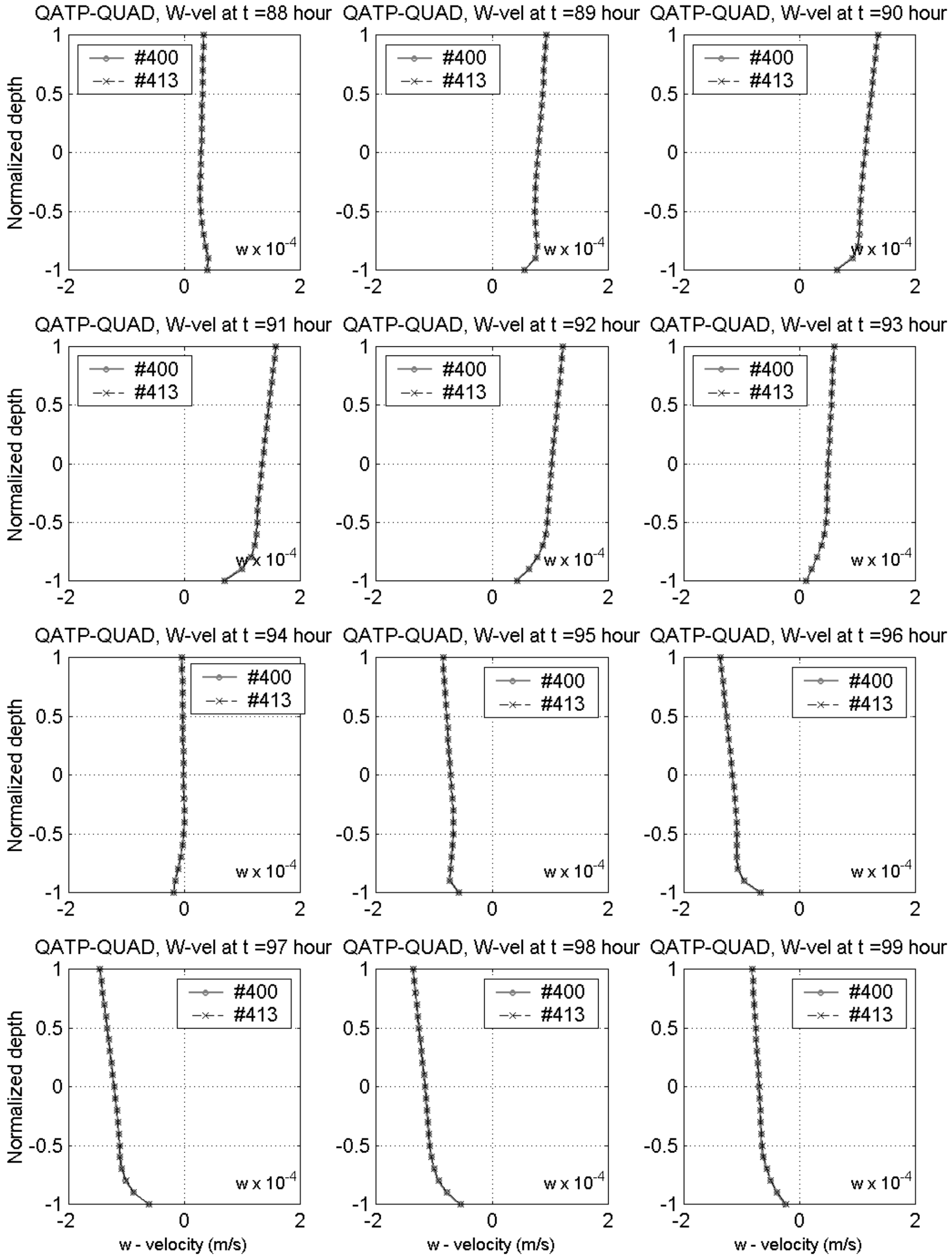

Fig. 2.8. One-semi diurnal tidal period plots of the vertical velocity, *w*, computed with Mellor-Yamada (MY) vertical eddy diffusivity at nodes 400 and 413. The plots are presented every one hour starting from t = 88h.

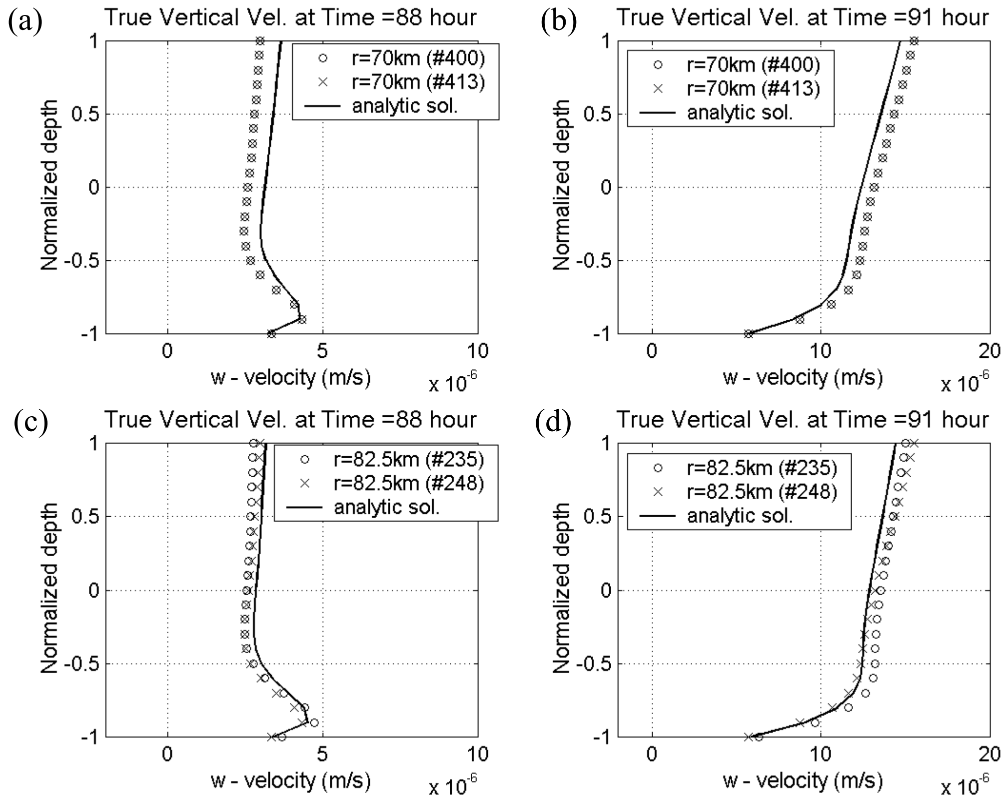

Fig. 2.9. Snapshot of amplitude of horizontal velocity solutions taken at t = 88h (water slack at low tide) and t = 91h (maximum flood tide at nearly zero tide level). The numerical solutions are compared with the analytical solutions: (a) at r = 70km, t = 88h; (b) at r = 70km, t = 91h; (b) at r = 82.5 km, t = 88h; (b) at r = 82.5km, t = 91h.

All selected points referenced here are similar to the points used by Muccino et al. (1997) and Luettich et al. (2002) for comparison of the three-dimensional FUNDY5 model to the analytical solutions. The results in this study are in good agreement with their results.

An interesting result is the three-dimensional profile of the flow along the radial distance. Fig. 2.10 shows two profiles of radial sections at θ=8.4° and θ=45°, with the arrows indicating the direction of flow and the contour lines indicating the magnitude of vertical velocity. Both profiles are quite similar and consistent providing independent solutions on θ. Consistent profiles (not shown) were also obtained for other θ values, with a slight difference in vertical velocity values that is likely due to numerical round off error. (Note that they are very exaggerated plots.)

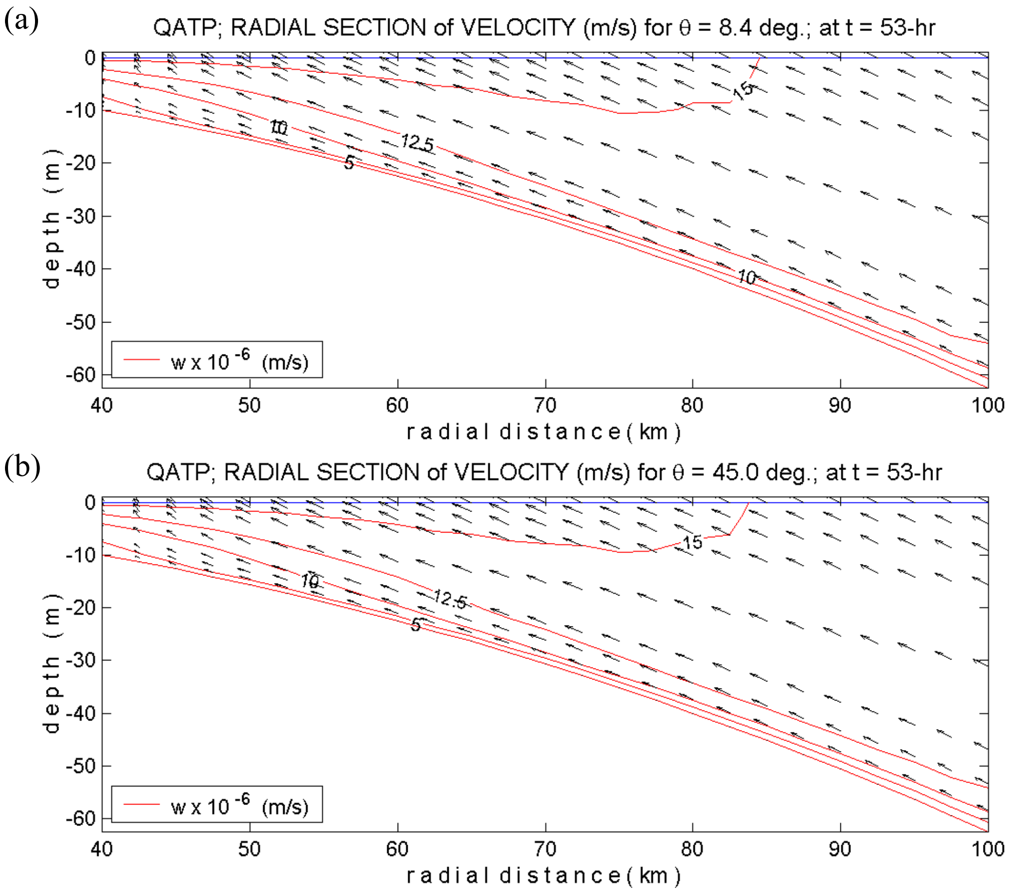

Fig. 2.10. A snapshot of **r**adial sections of three-dimensional velocity vector (arrows) at maximum upstream current t=53-hr for (a) θ=8.4°, and (b) θ=45°. Contour lines indicate the magnitude of vertical velocity in order of 10^{-6} m/s.

In the shallow area near the left end of the closed boundary the vertical velocity becomes significant in the flow field. Due to the presence of the wall, the horizontal current is quite small in the order of magnitude of the vertical velocity. Therefore, solving the vertical velocity in this region provides important information for better understanding of the flow as in near coastal, waterway or estuary zones.

The results of QATP have shown that the numerical model provides a reasonable three-dimensional velocity, and it is in accordance with the provided analytical solution. However, the horizontal velocity solution of the ADCIRC 3D-VS model exhibits doubtful results in the nodes near the lateral closed-boundary at both θ=0° and θ=90°. It is likely that the model will give zero tangential velocity along circular sections; but the numerical results reveal a significant tangential velocity mainly around the nodes near the lateral boundary (Pandoe and Edge, 2003).

An improvement in three-dimensional ADCIRC 3D-VS model has been made to include the vertical velocity solution. The accuracy of vertical velocity solution is critically dependent on the accuracy of the horizontal velocity solution. At some points from the QATP case, the presence of tangential velocity may lead to over determined vertical velocity solution.

In another experiment with a circular domain given in Pandoe and Edge (2003), so called ATP (Annular Test Problem), the result removes the presence of that error noted on the lateral boundaries. For this case at r=70km, the model demonstrates a significantly reduced tangential velocity near the “boundary” down to the order of 10^{-7}m/s. More uniform vertical flows along the circular section have been achieved in the ATP case rather than the profiles in the QATP. However, the cause of that tangential flow near the boundary has not been well studied yet. Practically it is recommended to define a boundary region many kilometers away from the specific area of study.

CHAPTER III

TRANSPORT/TRACERS MODULE AND THE BAROCLINIC FORCING TERMS

The barotropic term is constant with depth, in contrast to the baroclinic term which varies with depth (Fig. 3.1). The interaction of these two terms can create tidal asymmetry between the ebb and the flood of tidal cycle. During the flood current, the baroclinic and barotropic terms could be additive producing high acceleration near the bed, and vice versa during ebb current. In the regions where the thermal gradient of the sea are most pronounced such as in estuarine and coastal regions, the condition of baroclinicity is the most extreme. Generally, the baroclinic situation can be found in the surface layer with the barotropic conditions being approached at greater depth.

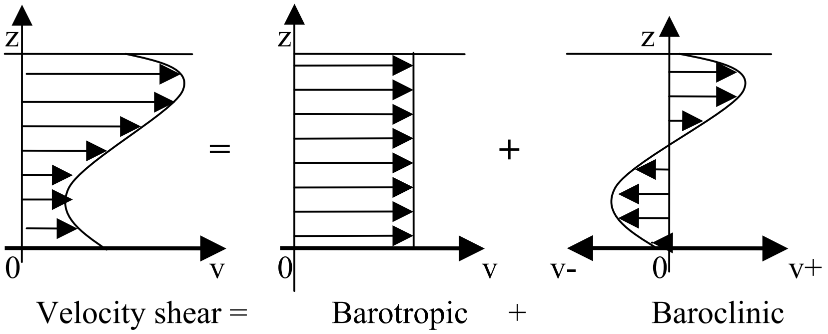

Fig. 3.1. The influence of the barotropic and baroclinic terms on the temporal acceleration.

3.1. Salinity/Tracer Transport Module

3.1.1 Governing Equations

The general governing equation for transport of salinity, temperature and tracer concentration (Blumberg and Mellor, 1987; Scheffner, 1999; Helfand et al., 1999; and HydroQual, 1998) is summarized as follows:

$$\frac{\partial R}{\partial t}+u\frac{\partial R}{\partial x}+v\frac{\partial R}{\partial y}+\omega\frac{(a-b)}{H}\frac{\partial R}{\partial \sigma}= \frac{\partial}{\partial x}\left(D_h\frac{\partial R}{\partial x}\right)+\frac{\partial}{\partial y}\left(D_h\frac{\partial R}{\partial y}\right)+\left(\frac{a-b}{H}\right)^2\frac{\partial}{\partial \sigma}\left[D_v\frac{\partial R}{\partial \sigma}\right] \tag{3.1}$$

where R is either salinity [psu], temperature [°C] or a tracer concentration [g/l)]; D_h and D_v are horizontal and vertical dispersion coefficients [m^2/s]; and ω is vertical velocities in σ-coordinate [m/s]. The surface and bottom boundary conditions for vertical salinity gradient are zero, while the surface boundary condition for temperature is given as:

$$\left(\frac{a-b}{H}\right)\left(D_v\frac{\partial R}{\partial \sigma}\right)=\frac{Q_{shf}}{\rho_o C_p} \qquad \text{at} \qquad z \rightarrow \eta \tag{3.2}$$

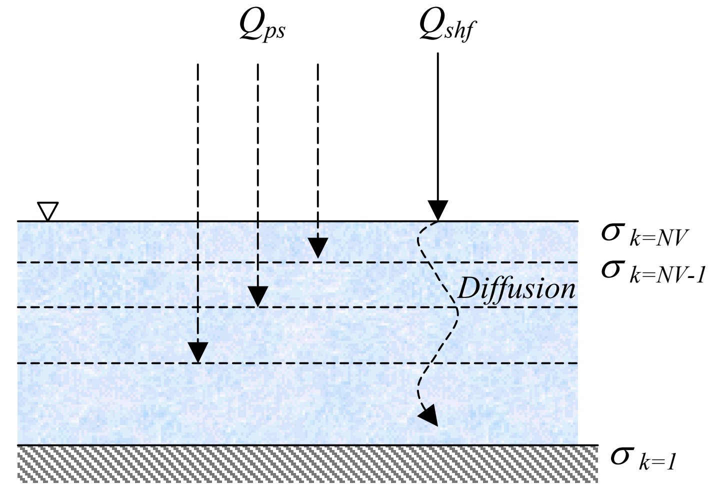

Fig. 3.2. The implementation of the penetrating solar radiation (Q_{ps}) and surface heat flux (Q_{shf}) into the temperature equations.

The temperature transport formulation differs slightly from that for salinity. In the temperature formulation, the external effect of solar radiation, called surface net heat flux (Q_{shf}) is included as (Hayes et al., 1991):

$$Q_{shf}=Q_{short}-Q_{long}-Q_{lat}-Q_{sen}-Q_{ps} \tag{3.3}$$

where it has been investigated that the mean value of net heat flux at the surface, Q_{shf}, is 165 W/m^2 with standard deviation of 10W/m^2. C_p is the specific heat of sea water at constant pressure [J/kg/°C] with bulk value $C_p \approx 4.00 \times 10^3$ J/kg/°C.

3.1.2 Eddy Diffusivity

In the development of the ADCIRC Transport, the horizontal diffusion coefficient, D_h, is assumed constant within the range of 0.1-10 m^2/s (Gross et al., 1999). The level-2.5 Turbulence Closure Model of Mellor-Yamada (1982) is used to calculate the vertical eddy diffusivity, D_v. It has been implemented by Blumberg et al. (1992) and Gross et al. (1999) with reasonably good results. The D_v is solved using the turbulence kinetic energy – $q^2/2$, and a turbulence macroscale, *l*.

3.1.3 Richardson Number (Ri)

The effect of density (i.e. salinity and temperature) variations gives a measure of stability. Turbulence occurrence will tend to mix the fluid, where light fluid is mixed down and the heavier fluid mixed up. A measure of relative importance between dynamic and density effects is the Richardson Number (*Ri*), which can be expressed as:

$$Ri = \frac{N^2}{\left(\left(\partial u / \partial z\right)^2 + \left(\partial v / \partial z\right)^2\right)} \tag{3.4}$$

Pond and Pickard (1995) suggested that if Ri < 0 then turbulence is enhanced by density variations; if Ri >0 they tend to reduce it. Empirically if Ri > ¼ then a stable stratified flow and turbulence cannot be generated by vertical gradients of horizontal velocity.

3.2. Solution Strategy

In general, the computed variables are determined from the non-conservative form of the momentum equation. Hereafter, an example of salinity solution in Eq.(3.1) is briefly provided, which involves finite element method for spatial and finite difference for temporal.

3.2.1. Weighted Residual

The weighted residual method for salinity is applied to Eq. (3.1) by replacing R with S, multiplying each term by a horizontal weighting function ϕ_j and integrating over the horizontal computational domain Ω, and then multiplying the results by a vertical weighting function ψ_k and integrating over the vertical domain Z.

$$\left\langle \left\langle \frac{\partial S}{\partial t}, \phi_j \right\rangle_\Omega, \psi_k \right\rangle_Z + \left\langle \left\langle \left(u\frac{\partial S}{\partial x} + v\frac{\partial S}{\partial y} + \omega\frac{(a-b)}{H}\frac{\partial S}{\partial \sigma} \right), \phi_j \right\rangle_\Omega, \psi_k \right\rangle_Z = \left\langle \left\langle \left[\frac{\partial}{\partial x}\left(D_h\frac{\partial S}{\partial x} \right) + \frac{\partial}{\partial y}\left(D_h\frac{\partial S}{\partial y} \right) \right], \phi_j \right\rangle_\Omega, \psi_k \right\rangle_Z + \left\langle \left\langle \left[\left(\frac{a-b}{H} \right)^2 \frac{\partial}{\partial \sigma}\left(D_v\frac{\partial S}{\partial \sigma} \right) \right], \phi_j \right\rangle_\Omega, \psi_k \right\rangle_Z \tag{3.5}$$

3.2.2. Horizontal Integration

Using similar rules provided by Luettich and Westerink (2002) for solving *u* and *v*, the horizontal discretization of salinity equation for each term yields:

- Horizontal integration of the *transient* term in Eq.3.5:

$$\left\langle \left\langle \frac{\partial S}{\partial t}, \phi_j \right\rangle_\Omega, \psi_k \right\rangle_Z = \frac{A_{NEj}}{3}\left\langle \frac{\partial S}{\partial t}, \psi_k \right\rangle_Z \tag{3.6a}$$

- Horizontal integration of the *horizontal advection* term in Eq.3.5:

$$\left\langle \left\langle \left(u\frac{\partial S}{\partial x} + v\frac{\partial S}{\partial y} \right), \phi_j \right\rangle_\Omega, \psi_k \right\rangle_Z = \left\langle \sum_{n=1}^{3} \frac{An}{3}\left(u_n\frac{\partial S_n}{\partial x} + v_n\frac{\partial S_n}{\partial y} \right), \psi_k \right\rangle_Z \tag{3.6b}$$

- Horizontal integration of the *vertical advection* term in Eq.3.5:

$$\left\langle \left\langle \left(\omega\left(\frac{a-b}{H} \right)\frac{\partial S}{\partial \sigma} \right)\phi_j \right\rangle_\Omega, \psi_k \right\rangle_Z = \frac{A_{NEj}}{3}\frac{(a-b)}{H}\left\langle \omega_j\frac{\partial S_j}{\partial \sigma}, \psi_k \right\rangle_Z \tag{3.6c}$$

- Horizontal integration of the *lateral diffusion* term in Eq.3.5:

$$\left\langle \left\langle \left[\frac{\partial}{\partial x}\left(D_h\frac{\partial S}{\partial x} \right) + \frac{\partial}{\partial y}\left(D_h\frac{\partial S}{\partial y} \right) \right], \phi_j \right\rangle_\Omega, \psi_k \right\rangle_Z = -\left\langle \left[D_h\sum_{n=1}^{NEj} A_n\left(\frac{\partial S}{\partial x}\frac{\partial \phi_j}{\partial x} + \frac{\partial S}{\partial y}\frac{\partial \phi_j}{\partial y} \right) \right], \psi_k \right\rangle_Z \tag{3.6d}$$

this term is obtained by assuming that the lateral diffusion is zero along external boundary segments.

- Horizontal integration of the <u>*vertical diffusion*</u> term in Eq.3.5:

$$\left\langle \left\langle \left[\left(\frac{a-b}{H} \right)^2 \frac{\partial}{\partial \sigma} \left(D_v \frac{\partial S}{\partial \sigma} \right) \right], \phi_j \right\rangle_{\Omega}, \psi_k \right\rangle_{Z} = \frac{A_{NEj}}{3} \left(\frac{a-b}{H} \right)^2 \left\langle \frac{\partial}{\partial \sigma} \left(D_v \frac{\partial S}{\partial \sigma} \right), \psi_k \right\rangle_{Z} \qquad (3.6e)$$

where: $A_{NEj} = \sum_{n=1}^{NEj} A_n$ is an area of all elements surrounding node-*j;* A_n is an area of element n; and NE_j is number of elements containing node j

3.2.3. Vertical Integration

A one-dimensional FEM vertical discretization provides the following rules (Luettich and Westerink, 2003):

$$\langle \gamma, \psi_k \rangle_Z = \begin{cases} \gamma_{k-1} \int_{\sigma_{k-1}}^{\sigma_k} \gamma_{k-1} \gamma_k d\sigma + \gamma_k \int_{\sigma_{k-1}}^{\sigma_k} \gamma_k \gamma_k d\sigma & k = NV \\ \gamma_{k-1} \int_{\sigma_{k-1}}^{\sigma_k} \gamma_{k-1} \gamma_k d\sigma + \gamma_k \int_{\sigma_{k-1}}^{\sigma_{k+1}} \gamma_k \gamma_k d\sigma + \gamma_{k+1} \int_{\sigma_k}^{\sigma_{k+1}} \gamma_{k+1} \gamma_k d\sigma & 1 < k < NV \\ \gamma_k \int_{\sigma}^{\sigma_{k+1}} \gamma_k \gamma_k d\sigma + \gamma_{k+1} \int_{\sigma_k}^{\sigma_{k+1}} \gamma_{k+1} \gamma_k d\sigma & k = 1 \end{cases}$$

or, in shorthand notation, this can be written:

$$\langle \gamma, \psi_k \rangle_Z \equiv \gamma_{k-1} Inm_{k,1} + \gamma_k Inm_{k,2} + \gamma_{k+1} Inm_{k,3} = \sum_{m=1}^{3} \gamma_{k+m-2} Inm_{k,m} \qquad (3.7)$$

where:

ψ_k is a vertical weighting function; ψ_k =1 at node, and ψ_k = 0 at all other nodes.

k is a node number over vertical elements with k = 1 at the bottom and k = NV at the surface

$$Inm_{k,1} = \begin{cases} \int_{\sigma_{k-1}}^{\sigma_k} \psi_{k-1} \psi_k d\sigma = \frac{1}{2} \int_{\sigma_{k-1}}^{\sigma_k} \psi_k \psi_k d\sigma = \frac{\sigma_k - \sigma_{k-1}}{6} & for \quad k \neq 1 \\ 0 & for \quad k = 1 \end{cases} \qquad (3.8a)$$

$$Inm_{k,3} = \begin{cases} \int_{\sigma_k}^{\sigma_{k+1}} \psi_{k+1} \psi_k d\sigma = \frac{1}{2} \int_{\sigma_k}^{\sigma_{k+1}} \psi_k \psi_k d\sigma = \frac{\sigma_{k+1} - \sigma_k}{6} & for \quad k \neq NV \\ 0 & for \quad k = NV \end{cases} \qquad (3.8b)$$

$$Inm_{k,2} = 2\left(Inm_{k,1} + Inm_{k,3}\right) \tag{3.8c}$$

Applying rules in Eq.3.7 and 3.8 to all terms of Eq.3.6a-e, and multiplying by $3/A_{NE_j}$, then vertical discretization of salinity equation for each term yields:

- Vertical integration of the *transient* term in Eq.3.6:

$$\left\langle \frac{\partial S_j}{\partial t}, \psi_k \right\rangle_Z = \sum_{m=1}^{3} \frac{\partial S_{j,k+m-2}}{\partial t} Inm_{k,m} \tag{3.9a}$$

- Vertical integration of the *horizontal advection* term in Eq.3.6:

$$\frac{1}{A_{NEj}} \left\langle \sum_{n=1}^{3} \frac{An}{3}\left(u_n \frac{\partial S_n}{\partial x} + v_n \frac{\partial S_n}{\partial y} \right), \psi_k \right\rangle_Z = \frac{1}{A_{NEj}} \sum_{m=1}^{3} \left[\sum_{n=1}^{NEj} A_n \left(u_n \frac{\partial S_n}{\partial x} + v_n \frac{\partial S_n}{\partial y} \right) \right]_{k+m-2} Inm_{k,m} \tag{3.9b}$$

- Vertical integration of the *vertical advection* term in Eq.3.6:

$$\frac{(a-b)}{H} \left\langle \omega_j \frac{\partial S_j}{\partial \sigma}, \psi_k \right\rangle_Z = \frac{(a-b)}{H} \left[\left(\frac{\partial S_j}{\partial \sigma} \right)_{k-1,k} \left[\omega_{j,k-1} + 2\omega_{j,k} \right] Inm_{k,1} + \left(\frac{\partial S_j}{\partial \sigma} \right)_{k,k+1} \left[2\omega_{j,k} + \omega_{j,k+1} \right] Inm_{k,3} \right] \tag{3.9c}$$

- Vertical integration of the *lateral diffusion* term in Eq.3.6:

$$-\frac{3}{A_{NEj}} \left\langle \left[D_h \sum_{n=1}^{NEj} A_n \left(\frac{\partial S}{\partial x}\frac{\partial \phi_j}{\partial x} + \frac{\partial S}{\partial y}\frac{\partial \phi_j}{\partial y} \right) \right], \psi_k \right\rangle_Z = -\frac{3}{A_{NEj}} \sum_{m=1}^{3} \left[D_h \sum_{n=1}^{NEj} A_n \left(\frac{\partial S}{\partial x}\frac{\partial \phi_j}{\partial x} + \frac{\partial S}{\partial y}\frac{\partial \phi_j}{\partial y} \right)_n \right]_{k+m-2} Inm_{k,m} \tag{3.9d}$$

- Vertical integration of the *vertical diffusion* term in Eq.3.6 is simplified to:

$$\left(\frac{a-b}{H} \right)^2 \left\langle \frac{\partial}{\partial \sigma}\left(D_v \frac{\partial S}{\partial \sigma} \right), \psi_k \right\rangle_Z = -\left(\frac{a-b}{H} \right)^2 \sum_{m=1}^{3} S_{j,k+m-2} KSnm_{k.m} \tag{3.9e}$$

since $\left. \left(D_v \frac{\partial S}{\partial \sigma} \right) \right|_{k=1} = 0$ and $\left. \left(D_v \frac{\partial S}{\partial \sigma} \right) \right|_{k=NV} = 0$

in which $KSnm_{k,m}$ given in *Luettich and Westerink* (2003) is:

$$KSnm_{k,1} = \begin{cases} \left(\dfrac{\partial \psi_{k-1}}{\partial \sigma}\right)_{k-1,k} \left(\dfrac{\partial \psi_{k}}{\partial \sigma}\right)_{k-1,k} \left(Dv_{j,k-1} \displaystyle\int_{\sigma_{k-1}}^{\sigma_k} \psi_{k-1} d\sigma + Dv_{j,k} \int_{\sigma_{k-1}}^{\sigma_k} \psi_{k} d\sigma \right) & \\ = -\left(\dfrac{\partial \psi_{k}}{\partial \sigma}\right)_{k-1,k} \left(\dfrac{\partial \psi_{k}}{\partial \sigma}\right)_{k-1,k} \left(Dv_{j,k-1} \displaystyle\int_{\sigma_{k-1}}^{\sigma_k} \psi_{k-1} d\sigma + Dv_{j,k} \int_{\sigma_{k-1}}^{\sigma_k} \psi_{k} d\sigma \right) & \\ = -\dfrac{Dv_{j,k} + Dv_{j,k-1}}{2\left(\sigma_k - \sigma_{k-1}\right)} & for \quad k \neq 1 \\ 0 & for \quad k = 1 \end{cases} \tag{3.10a}$$

$$KSnm_{k,3} = \begin{cases} \left(\dfrac{\partial \psi_{k+1}}{\partial \sigma}\right)_{k,k+1} \left(\dfrac{\partial \psi_{k}}{\partial \sigma}\right)_{k,k+1} \left(Dv_{j,k} \displaystyle\int_{\sigma_{k}}^{\sigma_{k+1}} \psi_{k} d\sigma + Dv_{j,k+1} \int_{\sigma_{k}}^{\sigma_{k+1}} \psi_{k+1} d\sigma \right) & \\ = -\left(\dfrac{\partial \psi_{k}}{\partial \sigma}\right)_{k,k+1} \left(\dfrac{\partial \psi_{k}}{\partial \sigma}\right)_{k,k+1} \left(Dv_{j,k} \displaystyle\int_{\sigma_{k}}^{\sigma_{k+1}} \psi_{k} d\sigma + Dv_{j,k+1} \int_{\sigma}^{\sigma_{k+1}} \psi_{k+1} d\sigma \right) & \\ = -\dfrac{Dv_{j,k+1} + Dv_{j,k}}{2\left(\sigma_{k+1} - \sigma_{k}\right)} & for \quad k \neq NV \\ = \quad 0 & for \quad k = NV \end{cases} \tag{3.10b}$$

$$KSnm_{k,2} = -\left(KSnm_{k,1} + KSnm_{k,3}\right) \tag{3.10c}$$

Thus following vertical integration, Eqs.3.9a-e become:

$$\begin{aligned} &\sum_{m=1}^{3} \frac{\partial S_{j,k+m-2}}{\partial t} Inm_{k,m} + \frac{1}{A_{NEj}} \sum_{m=1}^{3} \left[\sum_{n=1}^{NEj} A_n \left(u_n \frac{\partial S_n}{\partial x} + v_n \frac{\partial S_n}{\partial y} \right) \right]_{k+m-2} Inm_{k,m} \\ &+ \frac{(a-b)}{H} \left[\left(\frac{\partial S_j}{\partial \sigma} \right)_{k-1,k} \left[\omega_{j,k-1} + 2\omega_{j,k} \right] Inm_{k,1} + \left(\frac{\partial S_j}{\partial \sigma} \right)_{k,k+1} \left[2\omega_{j,k} + \omega_{j,k+1} \right] Inm_{k,3} \right] = \\ &- \frac{3}{A_{NEj}} \sum_{m=1}^{3} \left[D_h \sum_{n=1}^{NEj} A_n \left(\frac{\partial S}{\partial x} \frac{\partial \phi_j}{\partial x} + \frac{\partial S}{\partial y} \frac{\partial \phi_j}{\partial y} \right)_n \right]_{k+m-2} Inm_{k,m} \\ &- \left(\frac{a-b}{H} \right)^2 \sum_{m=1}^{3} S_{j,k+m-2} KSnm_{k.m} \end{aligned} \tag{3.11}$$

3.2.4 Time Discretization:

Eq.3.11 is discretized in time using a two time level explicit scheme at the present (t) and future (t+1) time levels as described below:

Transient term: $\sum_{m=1}^{3} \frac{S_{j,k+m-2}^{t+1} - S_{j,k+m-2}^{t}}{\Delta t} Inm_{k,m}$ (3.12a)

Horizontal advection: $\frac{1}{A_{NEj}} \sum_{m=1}^{3} \left[\sum_{n=1}^{NEj} A_n \left(u_n \frac{\partial S_n^t}{\partial x} + v_n \frac{\partial S_n^t}{\partial y} \right) \right]_{k+m-2} Inm_{k,m}$ (3.12b)

Vertical advection: $\frac{(a-b)}{H_j^t} \left[\left(\frac{\partial S_j^t}{\partial \sigma} \right)_{k-1,k} \left[\omega_{j,k-1}^t + 2\omega_{j,k}^t \right] Inm_{k,1} + \left(\frac{\partial S_j^t}{\partial \sigma} \right)_{k,k+1} \left[2\omega_{j,k}^t + \omega_{j,k+1}^t \right] Inm_{k,3} \right]$

(3.12c)

Lateral diffusion: $-\frac{3}{A_{NEj}} \sum_{m=1}^{3} \left[D_j \sum_{n=1}^{NEj} A_n \left(\frac{\partial S^t}{\partial x} \frac{\partial \phi_j}{\partial x} + \frac{\partial S^t}{\partial y} \frac{\partial \phi_j}{\partial y} \right)_n \right]_{k+m-2} Inm_{k,m}$ (3.12d)

Vertical diffusion: $-(a-b)^2 \sum_{m=1}^{3} \left[\beta_1 \frac{S_{j,k+m-2}^{t+1}}{\left(H_j^{t+1}\right)^2} + (1-\beta_1) \frac{S_{j,k+m-2}^{t}}{\left(H_j^{t}\right)^2} \right] KSnm_{k.m}$ (3.12e)

3.2.5. Fully Discretized Equation:

Substituting Eqs.3.12a-e into Eq.3.11, multiplying by Δt and grouping time levels *t+1* and *t* yields:

$$
\begin{aligned}
&\sum_{m=1}^{3} S_{j,k+m-2}^{t+1} Inm_{k,m} + \beta_1 \Delta t \left(\frac{a-b}{H_j^{t+1}} \right)^2 \sum_{m=1}^{3} S_{j,k+m-2}^{t+1} KSnm_{k.m} = \\
&\quad + \sum_{m=1}^{3} S_{j,k+m-2}^{t} Inm_{k,m} \\
&\quad - \frac{\Delta t}{A_{NEj}} \sum_{m=1}^{3} \left[\sum_{n=1}^{NEj} A_n \left(u_n \frac{\partial S_n^t}{\partial x} + v_n \frac{\partial S_n^t}{\partial y} \right) \right]_{k+m-2} Inm_{k,m} \\
&\quad - \Delta t \frac{(a-b)}{H_j^t} \left[\left(\frac{\partial S_j^t}{\partial \sigma} \right)_{k-1,k} \left[\omega_{j,k-1}^t + 2\omega_{j,k}^t \right] Inm_{k,1} + \left(\frac{\partial S_j^t}{\partial \sigma} \right)_{k,k+1} \left[2\omega_{j,k}^t + \omega_{j,k+1}^t \right] Inm_{k,3} \right] \qquad (3.13) \\
&\quad - \frac{3\Delta t}{A_{NEj}} \sum_{m=1}^{3} \left[D_j \sum_{n=1}^{NEj} A_n \left(\frac{\partial S^t}{\partial x} \frac{\partial \phi_j}{\partial x} + \frac{\partial S^t}{\partial y} \frac{\partial \phi_j}{\partial y} \right)_n \right]_{k+m-2} Inm_{k,m}
\end{aligned}
$$

$$-\left(1-\beta_1\right)\Delta t\left(\frac{a-b}{H_j^t}\right)^2\sum_{m=1}^{3}S^t_{j,k+m-2}\,KSnm_{k.m}$$

3.2.6. Solution

Eq. 3.13 can be represented in the matrix form. The matrix is uncoupled in the horizontal direction and has a tri-diagonal form in the vertical direction.

$$\mathbf{M}\,S = Frs \tag{3.14}$$

with **M** is a tri-diagonal matrix; *S* is a scalar solution for salinity and *Frs* is the RHS terms of Eq. (3.13). Matrix **M** consists of:

$$M(k,k-1)=\begin{cases} Inm_{k,1}+\beta_1\Delta t\left(\dfrac{a-b}{H_j^{t+1}}\right)^2 KSnm_{k,1} & for\quad k\neq 1\\ 0 & for\quad k=1\end{cases}$$

$$M(k,k)=Inm_{k,2}+\beta_1\Delta t\left(\frac{a-b}{H_j^{t+1}}\right)^2 KSnm_{k,2}\qquad for\quad all\quad k$$

$$M(k,k+1)=\begin{cases} Inm_{k,3}+\beta_1\Delta t\left(\dfrac{a-b}{H_j^{t+1}}\right)^2 KSnm_{k,3} & for\quad k\neq NV\\ 0 & for\quad k=NV\end{cases}$$

or, in matrix form becomes:

$$\begin{bmatrix} b_k & c_k & 0 & & & & \\ a_{k-1} & b_{k-1} & c_{k-1} & & & & \\ & & \ddots & & & & \\ & & & \ddots & a_2 & b_2 & c_2 \\ & & & & 0 & a_1 & b_1 \end{bmatrix}\cdot\begin{bmatrix} S_k \\ S_{k-1} \\ \vdots \\ S_2 \\ S_1\end{bmatrix}=\begin{bmatrix} Frs_k \\ Frs_{k-1} \\ \vdots \\ Frs_2 \\ Frs_1\end{bmatrix} \tag{3.15}$$

where: $a_k = M_{k,k-1}$; $b_k = M_{k,k}$; $c_k = M_{k,k+1}$

3.3 The Baroclinic Forcing Terms

3.3.1. Derivation of the Baroclinic Pressure Gradient

The vertical momentum on Eq.2.3c can be rewritten as:

$$p_{z'} = \int_{z'}^{\eta} \rho g dz \tag{3.16}$$

Taking derivative of this expression with respect to x, and then taken with *Leibnitz rule of integration*:

$$\frac{\partial}{\partial x}\int_{\alpha(x)}^{\beta(x)} f(x,y)\,dy = \int_{\alpha(x)}^{\beta(x)} \frac{\partial f(x,y)}{\partial x}dy + f(x,\beta(x))\frac{\partial \beta}{\partial x} - f(x,\alpha(x))\frac{\partial \alpha}{\partial x} \tag{3.17}$$

Then the pressure gradients will be:

$$\begin{aligned} \frac{\partial p_{z'}}{\partial x} &= \frac{\partial}{\partial x} g\int_{z'}^{\eta} \rho\, dz \\ &= g\int_{z'}^{\eta} \frac{\partial \rho}{\partial x}dz + g\rho_{\eta}\frac{\partial \eta}{\partial x} - g\rho_{z'}\frac{\partial z'}{\partial x} \end{aligned}$$

since $\frac{\partial z'}{\partial x} = 0$, then:

$$\frac{\partial p_{z'}}{\partial x} = g\int_{z}^{\eta} \frac{\partial \rho}{\partial x}dz + g\rho_{\eta}\frac{\partial \eta}{\partial x} \tag{3.18}$$

total pressure gradient	=	baroclinic pres. Gradient	+	barotropic pres. Gradient

where ρ is a water density; ρ_η is the water density at the surface; η is the free surface elevation; and z' is arbitrary reference plane.

Robertson et al. (2001) applied normalized density in order to reduce the truncation error in the computation of the baroclinic pressure gradient (BcPG) in the Princeton Ocean Model (POM). Thus, the normalized baroclinic forcing terms on ADCIRC can be represented as:

$$b_x = \frac{g}{\rho_0}\int_{z}^{\eta} \frac{\partial}{\partial x}(\rho - \rho_0)\,dz = \text{baroclinic x – forcing} \tag{3.19a}$$

$$b_y = \frac{g}{\rho_0}\int_z^{\eta}\frac{\partial}{\partial y}\left(\rho-\rho_0\right)dz = \text{baroclinic y – forcing} \qquad (3.19b)$$

where: η = free surface elevation, and ρ_o is a general mean density, which was set to 1000 (or 1025) kg/m^3. The baroclinic term $b_{x\sigma}$ and $b_{y\sigma}$ are a function of density distribution. The variable density is determined from temperature *T*, salinity *S* and pressure p using the *International Equation of State of Sea Water, IES80.* Applying chain rule given in Eq.2.2, the baroclinic forcing terms $b_{x\sigma}$ and $b_{y\sigma}$ in the σ coordinate system can be written as:

$$\begin{aligned}
b_x &= \frac{g}{\rho_0}\frac{H}{(a-b)}\int_\sigma^a\left[\frac{\partial}{\partial x}\left(\rho-\rho_0\right)-\left(\frac{(\sigma-b)}{(a-b)}\frac{\partial\eta}{\partial x}+\frac{(\sigma-a)}{(a-b)}\frac{\partial h}{\partial x}\right)\frac{\partial}{\partial z}\left(\rho-\rho_0\right)\right]d\sigma \\
&= \frac{g}{\rho_0}\frac{H}{(a-b)}\int_\sigma^a\left[\frac{\partial}{\partial x}\left(\rho-\rho_0\right)-\frac{(a-b)}{H}\left(\frac{(\sigma-b)}{(a-b)}\frac{\partial\eta}{\partial x}+\frac{(\sigma-a)}{(a-b)}\frac{\partial h}{\partial x}\right)\frac{\partial}{\partial\sigma}\left(\rho-\rho_0\right)\right]d\sigma \\
&= \frac{g\,H}{(a-b)}\int_\sigma^a\left[\frac{\partial}{\partial x}\frac{(\rho-\rho_0)}{\rho_o}-\left(\frac{(\sigma-b)}{H}\frac{\partial\eta}{\partial x}+\frac{(\sigma-a)}{H}\frac{\partial h}{\partial x}\right)\frac{\partial}{\partial\sigma}\frac{(\rho-\rho_0)}{\rho_o}\right]d\sigma
\end{aligned}$$

$$b_x = \frac{g\,H}{(a-b)}\int_\sigma^a\left[\frac{\partial\rho'}{\partial x}-\left(\frac{(\sigma-b)}{H}\frac{\partial\eta}{\partial x}+\frac{(\sigma-a)}{H}\frac{\partial h}{\partial x}\right)\frac{\partial\rho'}{\partial\sigma}\right]d\sigma \qquad (3.20a)$$

and in similar way, we have b_y as:

$$b_y = \frac{g\,H}{(a-b)}\int_\sigma^a\left[\frac{\partial\rho'}{\partial y}-\left(\frac{(\sigma-b)}{H}\frac{\partial\eta}{\partial y}+\frac{(\sigma-a)}{H}\frac{\partial h}{\partial y}\right)\frac{\partial\rho'}{\partial\sigma}\right]d\sigma \qquad (3.20b)$$

where ρ' is a normalized in situ density (*Robertson et al.*, 2001):

$$\rho' = \frac{\rho_{\theta,S}}{\rho_o}-1 \quad ;\text{ with }\quad \rho_o = \rho_{\theta,S}\left(\theta_{surface},S_{surface}\right) \qquad (3.21)$$

In a similar way to the POM Model modification performed by Robertson et al. (2001), the baroclinic terms in ADCIRC do not require ρ_{mean} as proposed earlier by Mellor (1998) since the removal of ρ_{mean} also removes the pressure contribution to *in situ* density ρ. The normalized density ρ' may be separated into two portions – one from the potential temperature and salinity, ρ_N, and one from the pressure, ρ_P:

$$\rho'(x,y,\sigma) = \rho'_N\left[\theta(x,y,\sigma),S(x,y,\sigma)\right]+\rho'_P\left[\sigma,H(x,,y)\right] \qquad (3.22)$$

The baroclinic terms in (3.10a) and (3.10b) then could be determined from those two portions:

$$b_x = \frac{g\,H}{(a-b)} \int_{\sigma}^{a} \left[\frac{\partial \rho'_N}{\partial x} + \frac{\partial \rho'_P}{\partial x} - \left(\frac{(\sigma-b)}{H}\frac{\partial \eta}{\partial x} + \frac{(\sigma-a)}{H}\frac{\partial h}{\partial x} \right) \left(\frac{\partial \rho'_N}{\partial \sigma} + \frac{\partial \rho'_P}{\partial \sigma} \right) \right] d\sigma \qquad (3.23a)$$

$$b_y = \frac{g\,H}{(a-b)} \int_{\sigma}^{a} \left[\frac{\partial \rho'_N}{\partial y} + \frac{\partial \rho'_P}{\partial y} - \left(\frac{(\sigma-b)}{H}\frac{\partial \eta}{\partial y} + \frac{(\sigma-a)}{H}\frac{\partial h}{\partial y} \right) \left(\frac{\partial \rho'_N}{\partial \sigma} + \frac{\partial \rho'_P}{\partial \sigma} \right) \right] d\sigma \qquad (3.23a)$$

As presented by Robertson et al. (2001), the pressure portion of density can be cancelled while treating the sound of speed c as a constant. Then, the baroclinic pressure gradient (BcPG) in Eqs. (3.13a,b) reduce to:

$$b_x = \frac{g\,H}{(a-b)} \int_{\sigma}^{a} \left[\frac{\partial \rho'_N}{\partial x} - \left(\frac{(\sigma-b)}{H}\frac{\partial \eta}{\partial x} + \frac{(\sigma-a)}{H}\frac{\partial h}{\partial x} \right) \frac{\partial \rho'_N}{\partial \sigma} \right] d\sigma \qquad (3.24a)$$

$$b_y = \frac{g\,H}{(a-b)} \int_{\sigma}^{a} \left[\frac{\partial \rho'_N}{\partial y} - \left(\frac{(\sigma-b)}{H}\frac{\partial \eta}{\partial y} + \frac{(\sigma-a)}{H}\frac{\partial h}{\partial y} \right) \frac{\partial \rho'_N}{\partial \sigma} \right] d\sigma \qquad (3.24b)$$

where:

$$\rho'_N = \frac{\rho_{T,S,0}}{\rho_o} - 1 \qquad (3.25)$$

with $\rho_{T,S,0}$ given in Fofonoff (1985) as:

$$\begin{aligned} \rho_{T,S,0} = {} & 999.842594 + (6.793952\text{E-}2 * T) - 9.095290\text{E-}3 * T^2 + 1.001685\text{E-}4 * T \\ & - 1.120083\text{E-}6 * T^4 + 6.536332\text{E-}9 * T^5 + (0.824493 - 4.0899\text{E-}3 * T \\ & + 7.6438\text{E-}5 * T^2 - 8.2467\text{E-}7 * T^3 + 5.3875\text{E-}9 * T^4) * S + (-5.72466\text{E-}3 \\ & + 1.0227\text{E-}4 * T - 1.6546\text{E-}6 * T^2) * S^{1.5} + 4.8314\text{E-}4 * S^2 \end{aligned}$$

3.3.2. Baroclinic Solution into Momentum Equations

As discussed in Chapter 2, the baroclinic terms were not included into the hydrodynamic solutions. Thus, the implementation of the baroclinic terms involve the finite element formulation for Eq.3.24a-b. Similar to the development of hydrodynamic solution given in Lueetich and Westerink (2003), the baroclinic terms are discretized as follows (here, only x-term is described):

(1) Multiplying b$_x$ term in Eq.3.24a by a horizontal weighting function ϕ_j and integrating over the horizontal computational domain Ω and then multiplying the results by a vertical weighting function ψ_k and integrating over the vertical domain Z.

$$\left\langle \left\langle b_x, \phi_j \right\rangle_\Omega, \psi_k \right\rangle_Z \tag{3.26}$$

(2) Horizontal integration of the term in Eq.3.26 gives:

$$\left\langle \left\langle b_x, \phi_j \right\rangle_\Omega, \psi_k \right\rangle_Z = \left\langle \sum_{n=1}^{NE_j} \frac{An}{3} b_{xn}, \psi_k \right\rangle_Z \tag{3.27}$$

and multiplication by $3/A_{NEj}$ gives:

$$= \frac{1}{A_{NEj}} \left\langle \sum_{n=1}^{NE_j} A_n b_{xn}, \psi_k \right\rangle_Z \tag{3.28}$$

(3) Vertical integration of the *<u>baroclinic</u>* term in Eq.3.28 gives:

$$\frac{1}{A_{NEj}} \left\langle \sum_{n=1}^{3} A_n b_{xn}, \psi_k \right\rangle_Z = \frac{1}{A_{NEj}} \sum_{m=1}^{3} \left[\sum_{n=1}^{NEj} A_n b_{xn} \right]_{k+m-2} Inm_{k,m} \tag{3.29}$$

where Inm$_{k,m}$ is given in Eqs.3.8a-c

(4) Time discretization:

$$= \frac{\Delta t}{A_{NEj}} \sum_{m=1}^{3} \left[\sum_{n=1}^{NEj} A_n b_{xn} \right]_{k+m-2} Inm_{k,m} \tag{3.30}$$

(5) Fully discretized equation

$$= \sum_{m=1}^{3} \left\{ \Delta t \; BcPGx_{j,k+m-2} \right\} Inm_{k,m} \tag{3.31a}$$

where: $$BcPG_x = \frac{1}{A_{NEj}} \sum_{m=1}^{3} \left[\sum_{n=1}^{NEj} A_n b_{xn} \right]_k$$

and b$_{xn}$ is the baroclinic pressure gradient in x-direction given in Eq.3. 14a. In similar way, the disctretized baroclinic pressure gradient in y-direction is:

$$= \sum_{m=1}^{3} \left\{ \Delta t \; BcPGy_{j,k+m-2} \right\} Inm_{k,m} \tag{3.31b}$$

where: $$BcPG_y = \frac{1}{A_{NEj}} \sum_{m=1}^{3} \left[\sum_{n=1}^{NEj} A_n b_{yn} \right]_k$$

Eqs. 3.21a,b are the final form of discretized baroclinic pressure gradient that are applied into the fully discretized momentum equations where the governing equations is provided in Eq. 2.3.

3.4. Test Cases and Model Validation

3.4.1. Dam Break Problem

One case is demonstrated to assess the ability of the model to simulate the stratification process under very high salinity gradient between fresh and saline water. The simulation is performed in a simple rectangular domain with 24 km long, 9 km wide, and flat bottom depth 30 m. See Fig. 3.3 for the domain configuration. The domain contains 931 nodes, 1728 triangular elements with uniform grid size 500 m, and 21 σ-layers distributed uniformly in vertical direction. This test case is so-called Dam Break Problem (DBP). Fresh water exists in the right half part (x > 12 km) with uniform initial salinity value S_f = 3 psu, while ocean saline water exists in the left-half part, with initial salinity S_s = 35 psu. Both sides have similar uniform initial temperature T = 19°C.

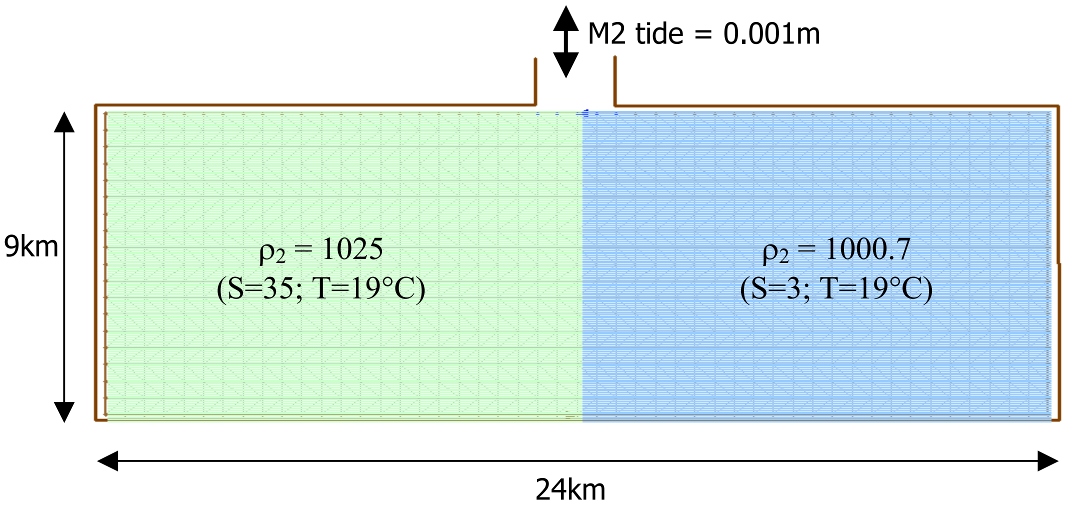

Fig. 3.3. Top view of domain and triangular grid of 30m depth of rectangular basin applicable for Dam Break Problem.

A small open boundary condition with 5-nodes is located in the middle of the northern side of the domain. To avoid effects of high oscillation in the domain, the open boundary is driven by very small semidiurnal M2 tide with amplitude of 0.001 m. The remaining boundary perimeter is assigned as land boundary indicated by a solid line in Fig. 3.3.

The DBP is simulated for 15 days, starting with very sharp salinity (i.e. density) gradient between fresh and saline water at x = 12 km. The Coriolis force is neglected. Then, the model lets the front expand horizontally due to diffusion while the baroclinic forcing works accordingly as the pressure density gradient requires. Fresh water that has lower density tends to ride over the saline water causing the fresh water in the top layers flowing to the left and saline water flows to the east at the bottom. In this simulation, a three-day ramp function is applied to the baroclinic force. This ramp function is intended to reduce the influence of the sharp density gradient in the beginning time steps that may cause instability in the model.

A couple of snapshots of salinity cross section is shown in Fig. 3.4a-f for t = 4, 60, 180, 300, 344, and 360 hours. The sections are taken along 24 km of the x-axis in the middle of the domain (y = 4.5 km), and vertical axes indicate the depths. After 4-h (Fig. 3.4a) the salinity front starts to break up to the west in the upper layers and to the east in the lower layers. The prevailing west-east density gradient generates flow; however, the horizontal currents are developed weakly due to the implementation of the baroclinic ramp function.

At t = 60-h (Fig. 3.4b) the stratification stars to develop, where the fresh water overlays saline water. The flow in the lower layer moves slower than the upper layers due to bottom friction, and the counter clockwise flow in the x-z axes exists. After 120 hours of simulation, the fully stratified waters were developed, and after the upper flow hits the boundary, the down welling occurs along the west land boundary and the pressure gradient orientation becomes eat-west direction. Similar mechanism occurs in the east land boundary. Thus, the upper and lower layers alter the flow direction becoming clockwise flow. Van Ledden (2003) mentioned that this flow pattern on the vertical plane is also

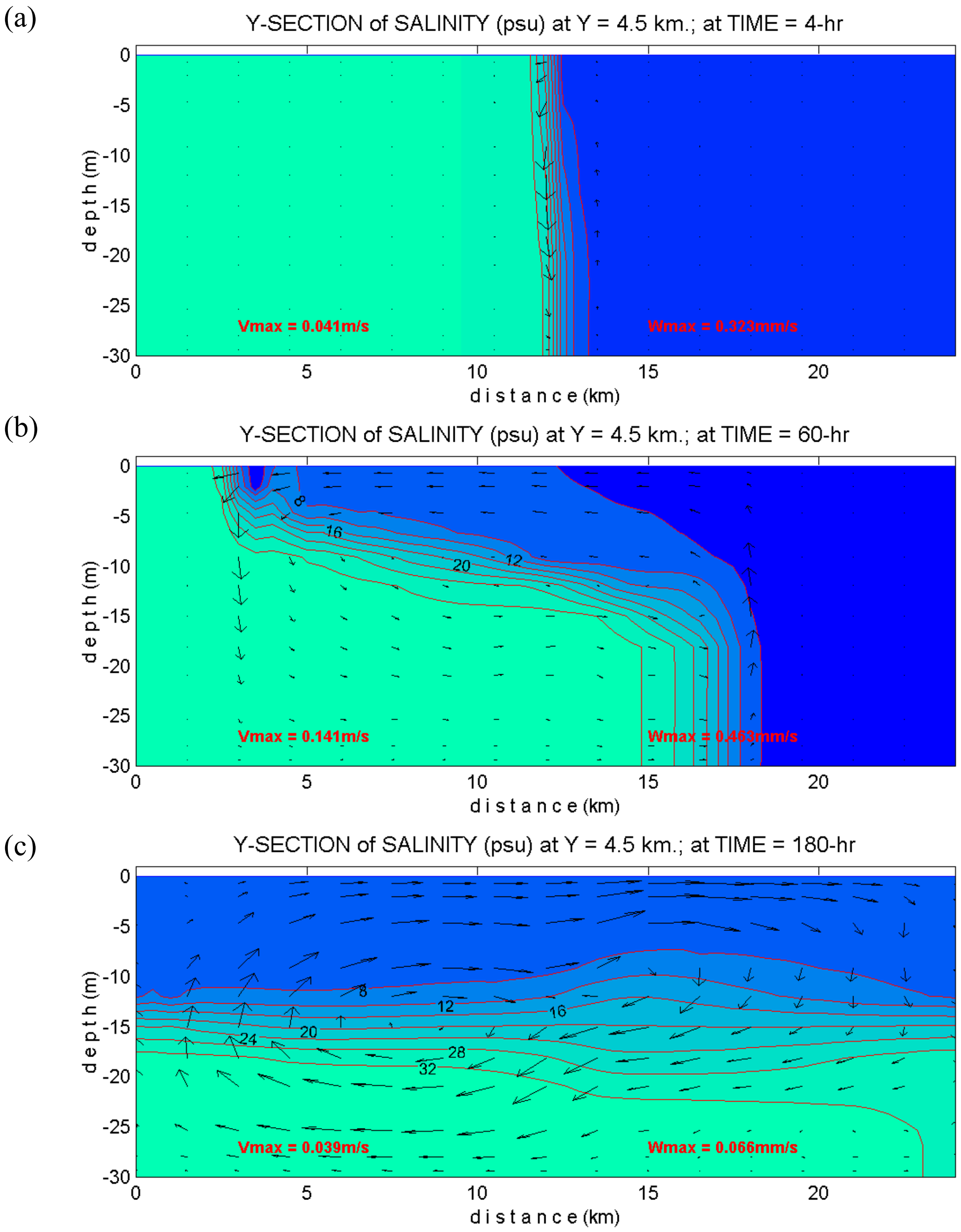

Fig. 3.4. Cross-sectional side views of salinity distribution taken along x-axis in the center of domain (y = 4.5km) for the Dam Break Problem. (a) 4 hours, (b) 60 hours, and (c) 180 hours. Contour lines represent the salinity values, and arrows for relative magnitude of current velocity.

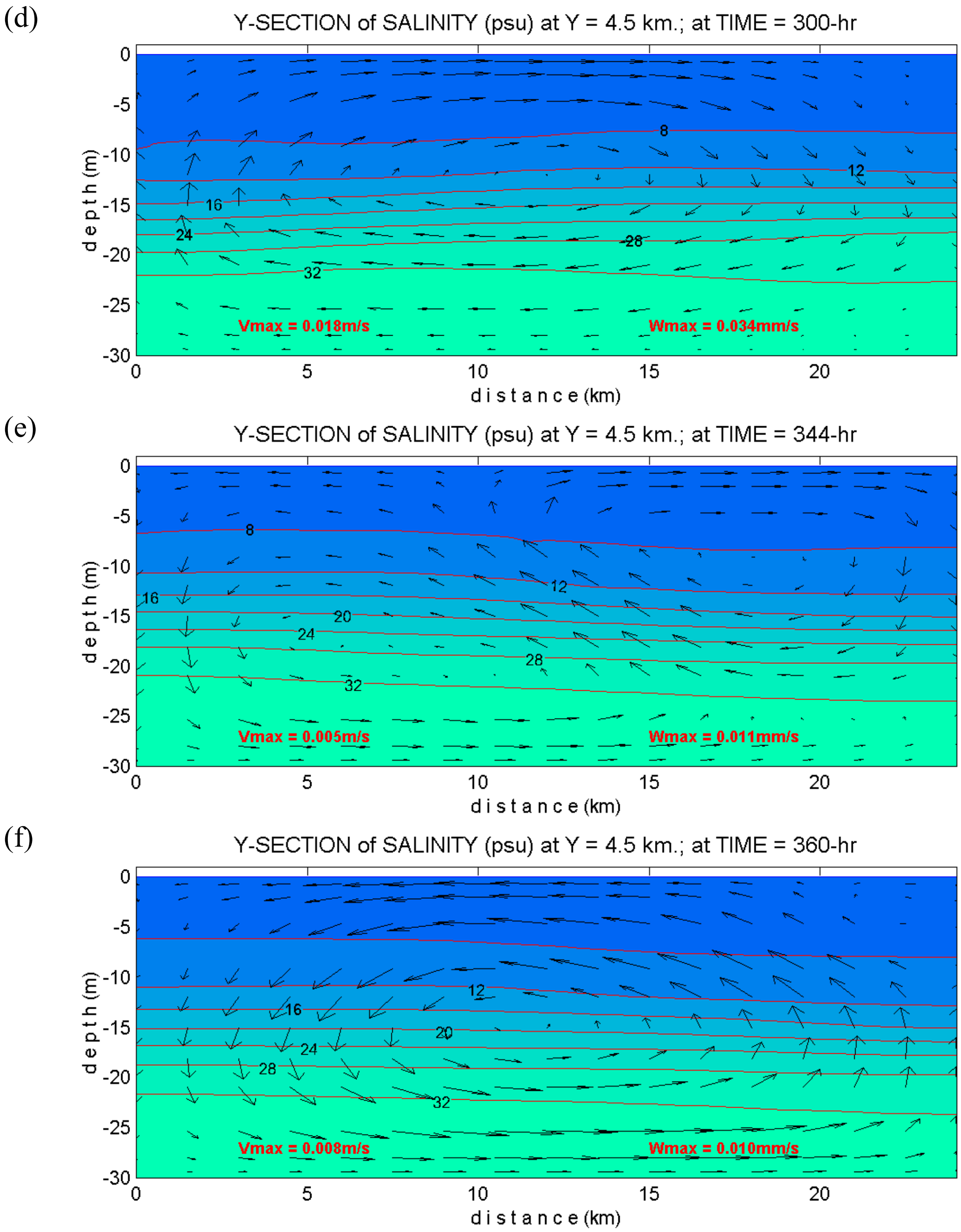

Fig. 3.4. (Cont'd). (d) 300 hours, (e) 344 hours, and (f) 360 hours. Contour lines represent the salinity values, and arrows for relative magnitude of current velocity.

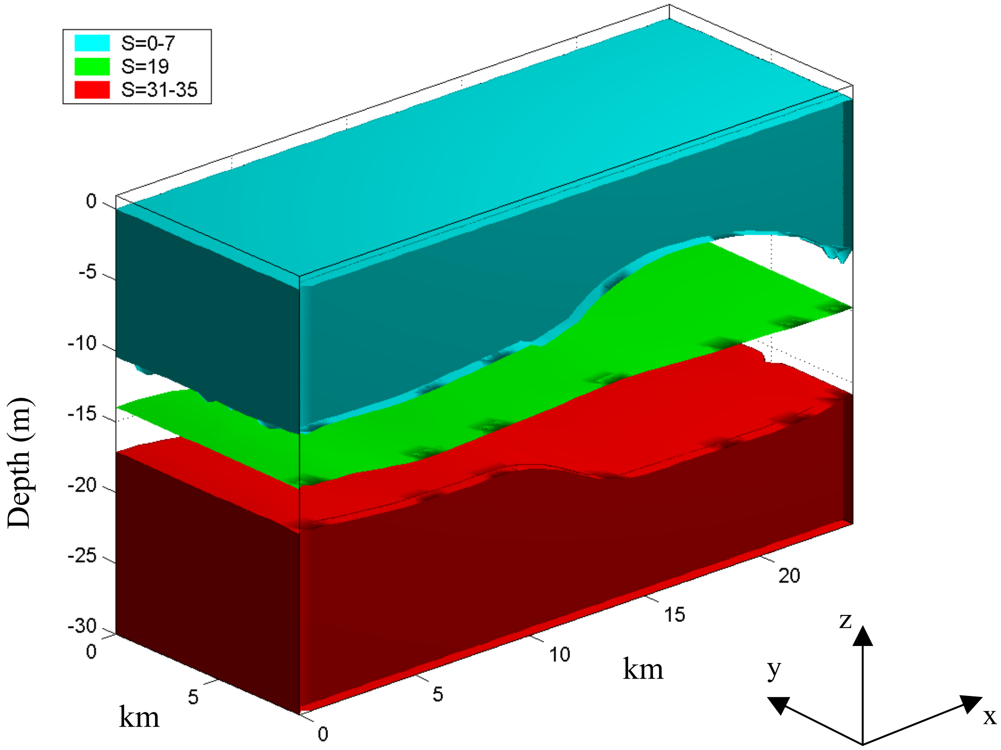

Fig. 3.5. One snapshot of 3D view of salinity at t = 180h. Lower layer (red) is saline water with salinity value S = 1 – 35 psu, mid-layer (green) is a mid salinity value S = 19 psu, and the upper layer (cyan) is the fresh water with salinity value S = 0-7 psu. The unit of x-y axes is km, and z-axis is m.

known as ‘gravitational circulation’. The circulation is actually generated by the presence of longitudinal salinity gradients.

At t = 180 h (Fig. 3.4c), when the flow direction is in the clockwise direction, the pressure gradient becomes weaker, and smaller current velocity generated. A three-dimensional view of this time snapshot, shown in Fig. 3.5, exhibits a nearly uniform flow across the domain with insignificant oscillation along the boundary due to numerical solution problems. A bulge in the eastern side is caused by the slower development of stratification in the lower layers than the upper layers in the earlier time. The rapid flow in the upper layers lead to upwelling near the eastern boundary, thus the salinity is relatively higher than that at the west. After the flow alters the direction, down welling occurs at the eastern boundary, at t = 180h, which will try to stabilize the salinity gradient. Thus, the existing bulge will become uniformly stratified after this time step, as shown in Fig. 3.4d, e and f. Those figures describe the mechanism of alternate flow from clockwise (t = 300h), transition (t = 344) and counter clockwise flow directions in x-z axes. During those periods, stratifications are well developed that produce weak flow due to less prominent density gradients. At t=344-h, Fig. 3.4e shows the transition of flow direction that generates vertically figure-eight pattern along the x-axis. Two down welling sites exists in both east and west boundaries, while upwelling is occured in the middle of the basin.

3.4.2. Idealized Riverine Case

The benchmarking of stratification due to the presence of the baroclinic terms is performed using the empirical 'saline wedge' formulation provided by Partheniades (1990a) and Ippen (1966). The comparison against theoretical length of saline wedge will be discussed by implementing the idealized riverine-ocean domain shown in Fig. 3.6. The ocean and river grid dimensions are 40 km alongshore, 24 km from the shoreline to the ocean boundary, and river length of 10 km and width of 1 km, respectively. The river has uniform depth of 4 m, and the ocean has a sloped bottom from 4 m depth at the shoreline down to 23 m depth along the open ocean boundary.

In this case, the model is driven by the 0.1 m amplitude of M2 tide in the open ocean boundary (left side), and by the influx of normal riverine flow with a constant velocity 0.2 m/s, and a constant Coriolis coefficient $f = 10^{-5}$ rad/s. The selection of small tidal amplitude is intended to avoid the oscillation of the saline wedge along the river. The initial condition of the domain has uniform salinity S_o = 35 psu and temperature T=19°C in the ocean part, while the river flow produces "fresh water" inflow with salinity S_r = 3 psu and temperature T_r = 19°C. The salinity gradient between ocean and river generate the pressure gradient due to salinity (i.e. density) difference.

The prevailing stratification and existence of density gradient will generate a baroclinic flow that drives an upstream flow in the lower layers of the river. This flow contributes to the development of a saline wedge. The balance between outward river

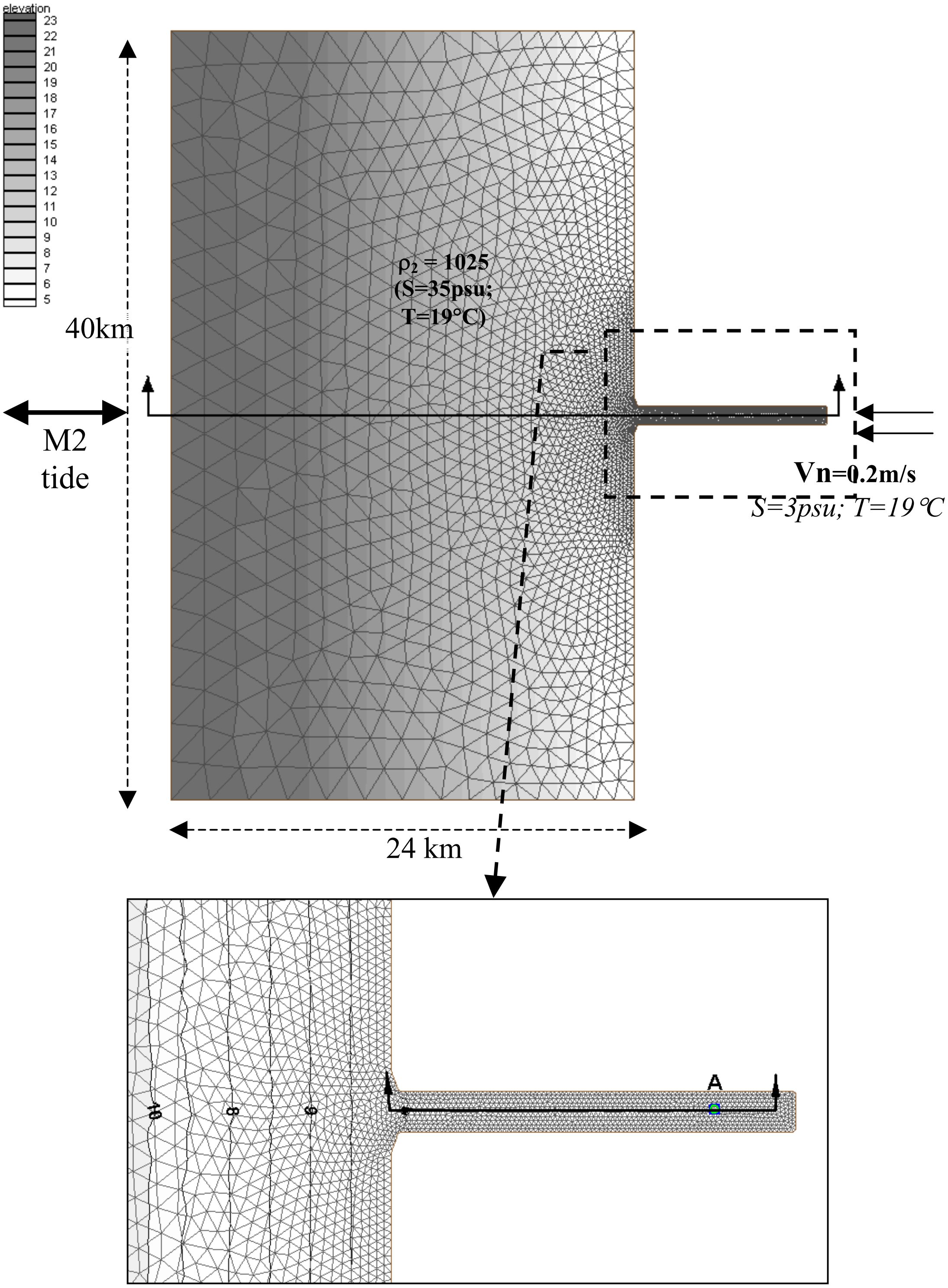

Fig. 3.6. Configuration of Idealized River-Ocean domain. Lower figure is the zooming part of the dashed-box indicated in the upper figure. Point A is the selected point to represent the river velocity.

flow to the ocean and inward flow into the river due to the baroclinic term provides a nearly steady point at the bottom of the penetrated saline wedge upstream. When the stability of hydrodynamic flow is achieved, the end tip of saline wedge consequently should shift up- and down-stream periodically in coherence with the period of the driving tidal current. Driven with only 0.1 m of M2 tidal amplitude, it is found that the distance range of that periodic shifting is within the range of less than 200 m.

Empirical computation of saline wedge travel was formulated by Partheniades (1990). He gave various lengths of penetrating saline wedge based on the outward river velocity and river depth (Fig. 3.7). The formula, which is also known as Schijf and Schoenfeld's equation, is written as:

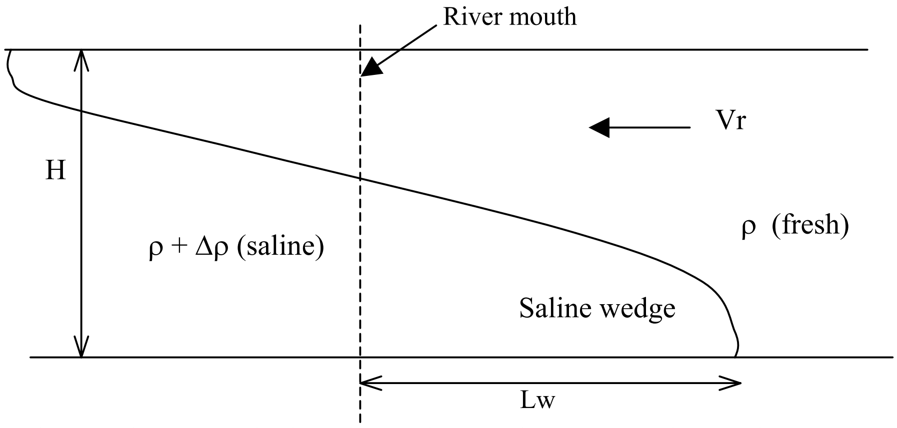

Fig. 3.7. Saline wedge; L_w is the length of saline wedge computed from the river mouth.

$$L_w = \frac{2h_o}{f}\left(\frac{1}{5Fr_o} - 2 + 3Fr_o^{(2/3)} - \frac{6}{5}Fr_o^{(4/3)}\right) \tag{3.32}$$

where: $Fr_o = \dfrac{V_r}{\sqrt{\dfrac{\Delta\rho\, g\, h_o}{\rho_f}}}$ is the densimetric Froude number; f is a friction coefficient; h_o is river depth at river mouth; and ρ_w is the density of fresh water.

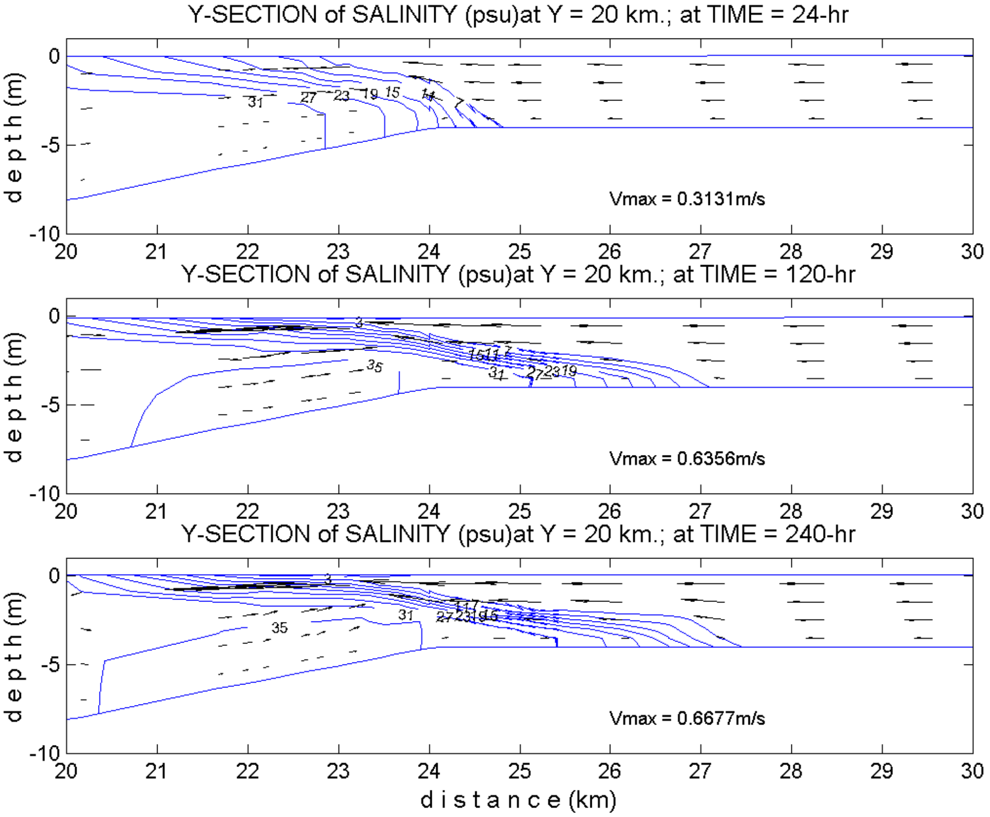

Fig. 3.8. Side-view profiles of salinity along the transect indicated in the lower figure of Fig. 3.6. The plots show the developed saline wedge at t = 1-day (top), 5-day (middle) and 10-day (bottom).

Fig. 3.8 (a, b and c) shows vertical profiles of developed arrested saline wedge due to freshwater influx from the river out to the ocean at the end of first (24h), fifth (120h) and tenth (240h) days, respectively. The profiles represent a transect along the middle of the river in the x-axis direction indicated in Fig. 3.6.

The upper layers exhibit strong outward flow immediately outside the river mouth and weakened conditions offshore. The maximum outward flow occurs at the river mouth with 0.67 m/s maximum velocity. Meanwhile the inward flow to the river develops the saline wedge with penetrating distance up to about 3.1 km upstream. In the first day, the stratification starts to occur, with less than 1 km of penetration upstream. After

5 and 10 days, the saline wedges are well developed without much change of the wedge length between the 5th and 10th day.

The penetration length of saline wedge is estimated graphically from the model results for comparison with the results of Eq.3.22. The effective outward velocity observed at point A (Fig. 3.6) is averaged over 10 days model observation to remove the effect of tidal oscillation (Fig. 3.9a). The time series consist of 4-hourly recorded current velocity. The oscillation of the maxima and minima velocities are caused by considerably long (four hours) recording time, thus the data could not provide the maxima and minima values of M2 tidal current precisely.

As previously discussed, the specified normal flow is 0.2 m/s; however due to a slightly widening effect of the river width as it flows from the normal flow boundary into the river domain, the effective averaged velocity decreases to 0.178 m/s. This value is then considered as the outward river velocity to compute the length of theoretical saline wedge. See Table 3.1. This gives the length of saline wedge as 3.11 km.

The corresponding length of saline wedge from the model is estimated from the last simulation day. Fig. 3.9b provides near bottom current velocities sampled every 4 hours, from 9d-00h to 10d-00h, along the center of the river starting 0.0m from the river mouth to the upstream direction. Positive and negative values indicate the upstream and downstream flows, respectively.

Table 3.1.
Length of saline wedge for various V_r and h_o.

V_r (m/s)	h_o (m)	L_w empirical (km)	L_w numerical (km)
0.10	4.0	10.41	8.14 [a]
0.18	4.0	3.11	3.13
0.18	5.0	5.93	5.84
0.20	2.0	0.44	0.47
0.20	4.0	2.46	n/a
0.20	5.0	4.18	n/a

[a] The wedge cannot penetrate further downstream due to the domain limit of 10km river length.

Figure 3.9c shows a top view of the direction of the flow along the river. The zero crossings indicate the location of the “null point”, or limit of penetration where the bottom velocity reverses direction, at each particular time. Averaging the location for 24 h provides the estimated length of arrested saline wedge as 3.13 km.

For a second case, the river depth is modified to 5 m depth (Table 3.1, Fig. 3.10). The model computes for this case that the length of saline wedge is 5.84 km, while the empirical model gives 5.93 km. All computations of arrested saline wedges provided in Table 3.1 are based on Eq. 3.22. This equation is actually very sensitive to the specified velocity value, thus careful attention must be taken in computing the theoretical arrested saline wedge. In general, however, the comparisons between numerical and Partheniades’s empirical models for the various lengths of saline wedge show good agreement. The newly extended ADCIRC-Transport numerical model does demonstrate the development of arrested saline wedge.

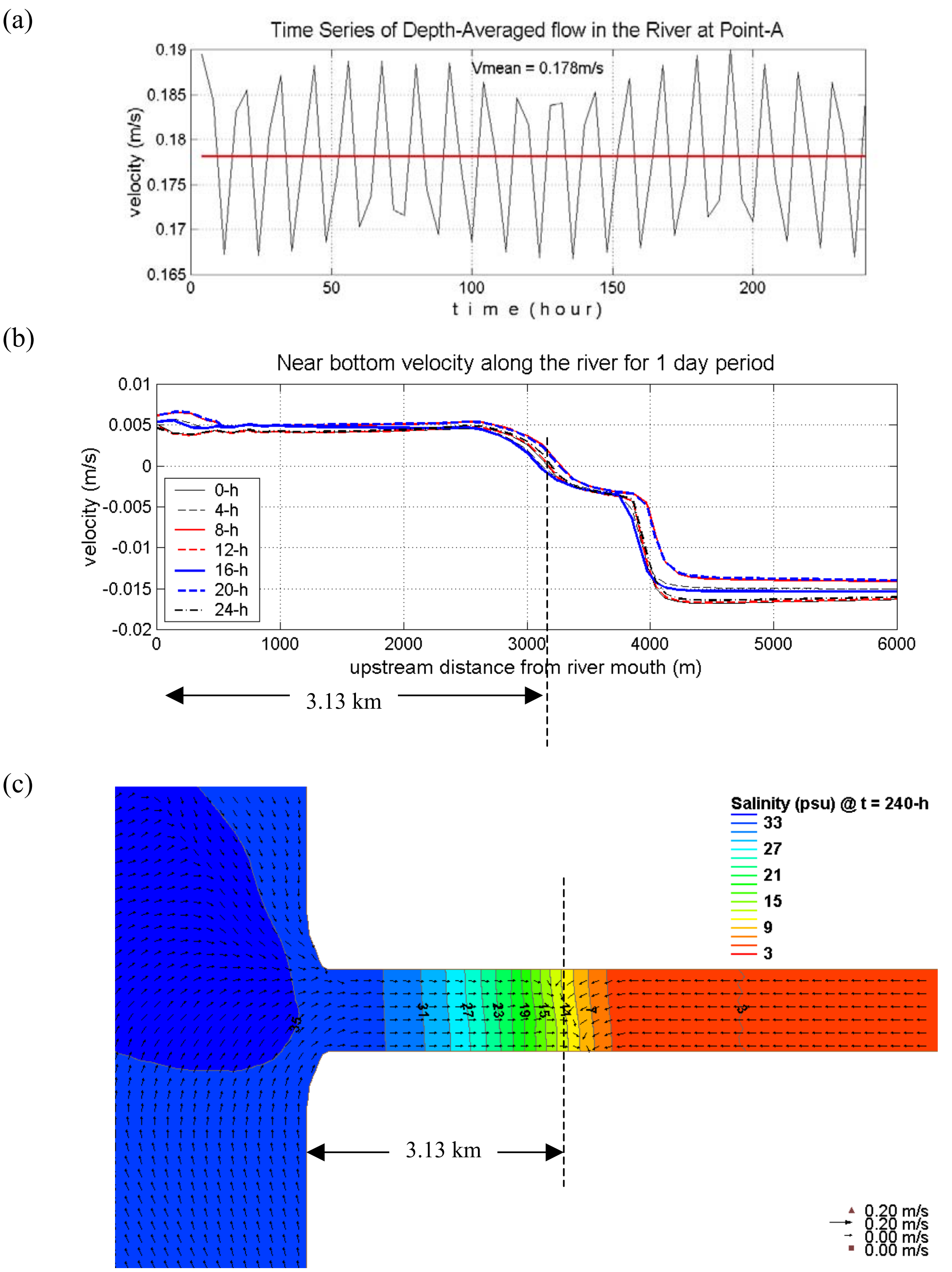

Fig. 3.9. (a) The assessment of finding the detided depth averaged river out flow from V_r at Point-A, (b) Near bottom velocity around the 'null point', where the mean location of zero crossing indicated by the dashed line is 3.13km from the river mouth, and (c) is the top view of the location of estimated null point. Arrows indicate the flow direction, and contour indicates salinity value. The estimated L_w is 3.13 km upstream from river mouth.

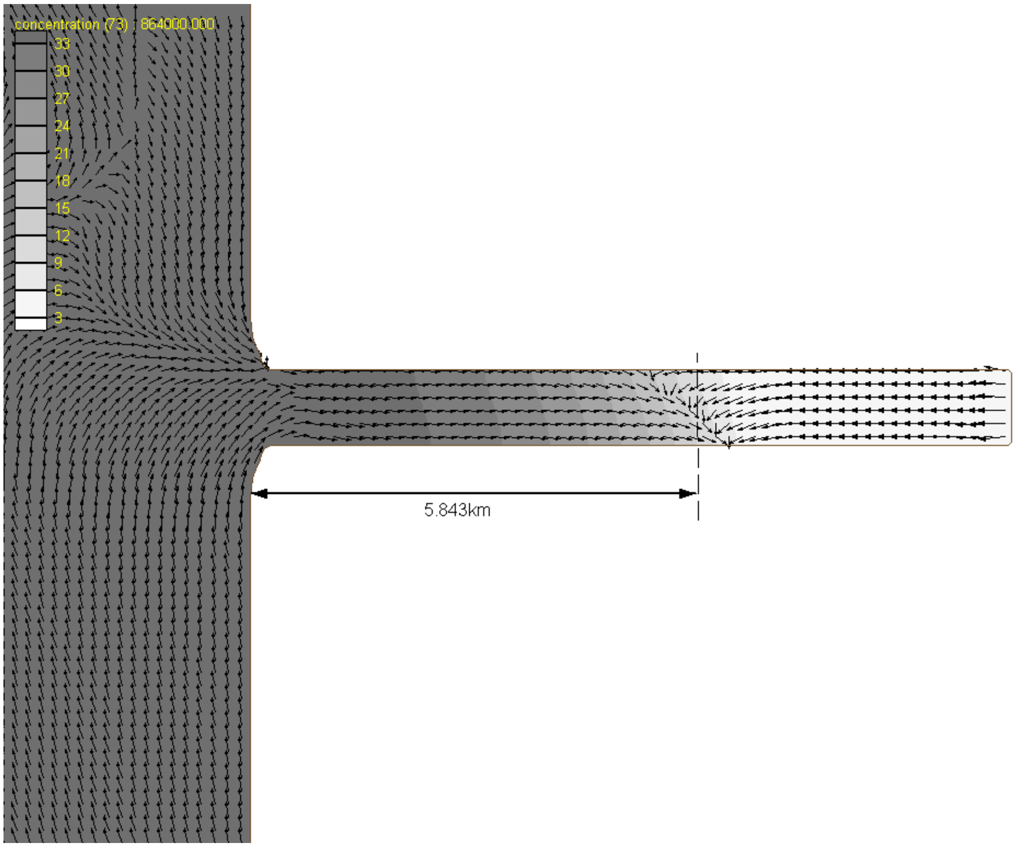

Fig. 3.10. Top view of the location of estimated null point for h_0 = 5m. Arrows indicate the flow direction, and contour indicates salinity value. The estimated L_w is 5.84 km upstream from river mouth.

CHAPTER IV

SEDIMENT TRANSPORT MODULE

Suspended materials in the water column are highly related to the hydrodynamic circulation. The interface of the salinity wedge or a convergence zone may be related to the presence of deposited sediments. Several mechanisms of both horizontal and vertical sediment transport based on sediment concentration can be distinguished, and are graphically presented in Fig. 4.1. Gravity force forces the sediment particles in the water column to settle down; meanwhile the vertical mixing occurs accordingly in upward and downward directions. Interaction between those two processes provides a vertical concentration profile (Whitehouse et al., 2000; Soulsby, 1997)

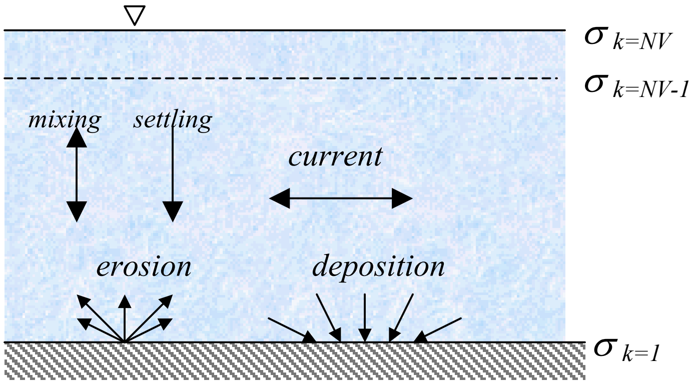

Fig. 4.1. Sediment transport processes. σ_k indicates the sigma layers starting k =1 at the bottom and k = NV at the surface.

The important mechanisms affecting suspended sediment transport are erosion, suspension, transport and deposition by horizontal variation of the bed shear stress. Non-cohesive sediments have a granular structure and the sediment particles do not stick together, thus the particle size and weight are the dominant parameters for erosion and deposition; whereas cohesive sediments are in coherent mass form due to electrochemical interactions among the particles that will dominate the transport behavior (van Ledden, 2003).

Currents over the bed and the bed roughness of the bed surface determine the bed shear stress, which is the key parameter for sediment transport processes. Current information is obtained from the hydrodynamic module. The bed roughness is considered constant in time and space.

4.1. Governing Equation of Sediment Transport

The governing equation for sediment concentration (HydroQual, 1998) is given as:

$$\begin{gathered}\frac{\partial C}{\partial t}+u\frac{\partial C}{\partial x}+v\frac{\partial C}{\partial y}+\frac{(a-b)}{H}(\omega-\omega_s)\frac{\partial C}{\partial \sigma}= \\ \frac{\partial}{\partial x}\left(D_h\frac{\partial C}{\partial x}\right)+\frac{\partial}{\partial y}\left(D_h\frac{\partial C}{\partial y}\right)+\left(\frac{a-b}{H}\right)^2\frac{\partial}{\partial \sigma}\left[D_v\frac{\partial C}{\partial \sigma}\right]\end{gathered} \tag{4.1}$$

and the boundary conditions:

$$\left(\frac{a-b}{H}\right)D_v\frac{\partial C}{\partial \sigma}=-\omega_s\,C_k \qquad \text{at} \qquad z \rightarrow \eta \tag{4.2a}$$

$$\left(\frac{a-b}{H}\right)D_v\frac{\partial C}{\partial \sigma}=E-D+\omega_s C_k \qquad \text{at} \qquad z \rightarrow -h \tag{4.2b}$$

where C is a sediment concentration [g/l or kg/m^3]; E is an erosion flux [kg/m^2/s]; D is a deposition flux [kg/m^2/s]; D_h, D_v are horizontal and vertical dispersion coefficients for sediment [m^2/s]; ω is a vertical velocity in σ-coordinate [m/s]; and ω_s is a settling velocity of sediment in σ-coordinate [m/s]. The sediment transport covers both cohesive and non-cohesive types of sediment.

Here the cohesive and non-cohesive sediment are treated independently, thus the settling velocities for each sediment type are computed differently. Similar to the tracer or salinity transport discussed in previous chapter, the horizontal diffusivity for sediment is constant and uniform in time and space.

Initial condition for the concentration has to be specified at t = 0h. In the presence of normal flow boundaries, the normal concentration fluxes have to be specified at all normal flow boundaries in the unit of kg/m^2. The model allows optional normal flux to be considered as natural or essential normal concentration flux.

4.2. Non-Cohesive Sediment (Sand)

4.2.1. Vertical Profile of Suspended Concentration

Above the threshold of motion, sand/sediment in the bed is lifted off into suspension, where it is carried by the current. The bottom friction governs the entrainment of sediment from the bed. When the sediment is suspended, the settling of sediments towards the bed is counterbalanced by diffusion of sand upward near the bed. In the environment of waves and currents, Soulsby (1997) provides a suggested vertical profile of the suspended sediment concentration (Fig. 4.2) presented in σ-level coordinate system in the following form:

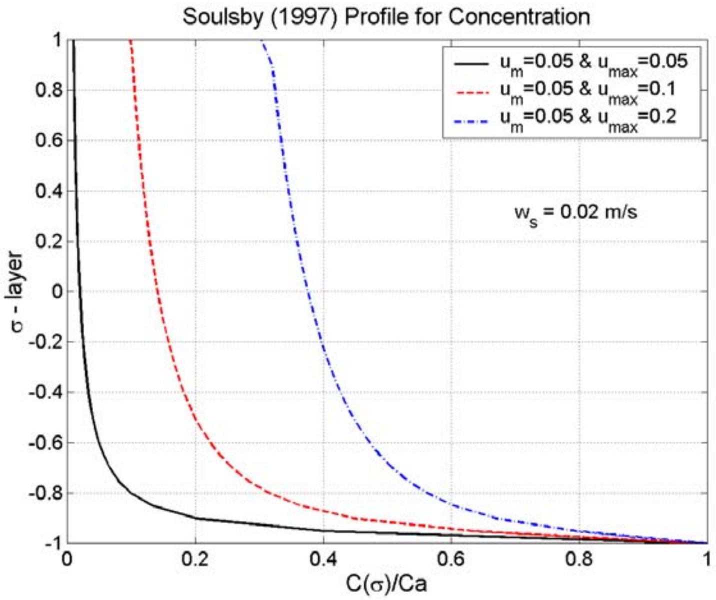

Fig. 4.2. Soulsby's vertical profile of suspended non-cohesive sediment concentration with variation mean (u_m) and maximum (u_{max}) friction velocities.

$$C_e(\sigma) = C_a \left(\frac{\sigma - b}{\sigma_a - b} \right)^{-b_{\max}} \qquad \text{for } \sigma_a < \sigma < \sigma_w \qquad (4.3)$$

$$C_e(\sigma) = C_e(\sigma_w)\left(\frac{\sigma - b}{\sigma_w - b}\right)^{-b_m} \qquad \text{for } \sigma_w < \sigma < a \tag{4.4}$$

with:

$b_{\max} = \dfrac{w_s}{\kappa u_{*\max}}$ = Maximum Rouse number or suspension parameter

$b_m = \dfrac{w_s}{\kappa u_{*m}}$ = Mean Rouse number or suspension parameter

$\sigma_w = a - \dfrac{z_w}{H}(a-b)$ = wave boundary thickness in σ-level

$z_w = \dfrac{u_{*\max} T}{2\pi}$ = wave boundary thickness in z-level

$u_{*\max} = \left(\dfrac{\tau_{\max}}{\rho}\right)^{1/2}$ = maximum friction velocity

$u_{*m} = \left(\dfrac{\tau_m}{\rho}\right)^{1/2}$ = mean friction velocity

$a = 1 = \sigma$ at the surface, and $b = -1 = \sigma$ at the bottom

where σ is a height above sea bed [m]; σ_a is a reference height near sea bed [m]; T is wave period [sec]; $C_e(\sigma)$ is a sediment concentration at height σ due to bed load [mass/volume]; κ is the von Karman's constant = 0.4; and C_a is a sediment reference concentration at height z_a [mass/volume] empirically formulated in Soulsby (1997) as:

$$C_a = \frac{0.015 d T_s^{3/2}}{z_a D_*^{0.3}} \qquad \text{with: } T_s = \frac{\tau_b - \tau_{cr}}{\tau_{cr}} = \text{threshold shear stress} \tag{4.5}$$

Settling velocity of natural sand particle, w_s, is evaluated using the formulation given by Cheng (1997) as follows:

$$w_s = \frac{\upsilon}{d_{50}}\left[\left(25 + 1.2 d_*^{\,2}\right)^{1/2} - 5\right]^{1.5} \tag{4.6}$$

where d_* is the dimensionless particle parameter, and ν is the kinematic viscosity.

4.2.2. Bed Shear Stress under Combined Wave and Current

The mean and maximum bed shear stresses under combined waves and currents are determined from an addition of the wave-alone and current-alone stresses, where Whitehouse et al. (2000) formulates as follow:

$$\tau_{mean} = \tau_c \left[1 - 1.2 \left(\frac{\tau_w}{\tau_c + \tau_w} \right)^{3.2} \right] \tag{4.7}$$

$$\tau_{\max} = \left[(\tau_{mean} + \tau_w \cos\phi)^2 + (\tau_w \sin\phi)^2 \right]^{1/2} \tag{4.8}$$

in which τ_{max} is given by a vector addition of τ_{mean} and τ_w; and φ is the angle of wave direction measured CCW from east. τ_c and τ_w are the bottom shear stresses which would occur due to the current-alone and to the wave-alone, respectively, with the formulation given below:

$$\tau_w = \frac{1}{2} \rho f_w U_{ob}^2 \tag{4.9}$$

$f_w = 1.39 \left(\frac{A}{z_o} \right)^{-0.52}$ = wave friction factor

$A = \frac{U_{ob} T}{2\pi}$ = semi orbital excursion [m]

$z_o = \frac{d_{50}}{12}$ = bed roughness (for hydrodynamically rough flow) [m]

$U_{ob} = \frac{HgkT}{4\pi} \frac{1}{\cosh(kd)}$ = amplitude of wave orbital velocity at the bottom [m]

Here, the model considers only linear wave with constant wave period and incoming wave angle.

4.2.3. Critical Bed Shear Stress

The critical bed shear stress in Eq. 4.5 can be determined from the threshold Shields parameter θ_{cr} as given in Van Rijn (1993) :

$$\tau_{cr} = \theta_{cr} g (\rho_s - \rho_w) d_{50}, \tag{4.10}$$

where:

$\theta_{cr} = \frac{0.30}{1 + 1.2 d_*} + 0.055 \left[1 - e^{(-0.02 d_*)} \right]$ = threshold Shields parameter

$d_* = \left(\frac{\Delta g}{\upsilon^2} \right)^{1/3} d_{50}$ = dimensionless particle parameter

$\Delta = \frac{\rho_s - \rho_w}{\rho_w}$

d_{50} = median grain diameter [m]

ν = kinematic viscosity [m^2/s]

The sediment concentration near the bed C_a adapts instantaneously to the distribution given in Eq. (4.3) and (4.4). To assure that the suspended sediment concentration in the water column *C(z)* follows the distribution of C_e, the erosion and diffusion terms, *E* and *D*, for very fine sand with $d_{50} \leq 0.1$mm are taken as:

$$E = \frac{1}{\Delta t} \int \left(C_e(z) - C(z) \right) dz \qquad \text{for} \qquad C_e(z) > C(z) \tag{4.11}$$

$$D = -\frac{w_s}{H} \int \left(C_e(z) - C(z) \right) dz \qquad \text{for} \qquad C_e(z) \leq C(z) \tag{4.12}$$

The deposition of non-cohesive sediment is described in terms of non-equilibrium conditions for the suspended load transport. It is assumed that the deposition removes an excess of suspended material in the water column with settling velocity w_s. In case $\tau_b < \tau_{cr}$ (ie. $C_e = 0$), the deposition flux term reduces to a general settling formulation:

$$D = w_s \, C_b \tag{4.13}$$

where *D* is a depositional flux of non-cohesive sediment [kg/m^{2}s]; *C* is a concentration of suspended non-cohesive sediment [kg/m^3]; C_b is the near bottom sediment concentration [kg/m^3]; and w_s is sediment settling velocity [m/s].

Applying Eq. 4.6 will produce a considerable large settling velocity, particularly for fine sand and larger. In ordinary tidal current and wave condition, the high concentration of suspended sediment will dominate the lower parts near the bottom. This is unfavorable to solve in the finite element formulation since the presence of high gradient of concentration may cause model instability. The solution for this problem is either apply the depth-integrated transport rate formulation or increase the vertical layers and time step. The latter may cause significant increase of computational time, so the first option is more reliable to be applied in the non-cohesive sediment transport for size larger than fine sand.

Based on that reason, having first established the vertical profiles of velocity u(z) and suspended concentration $C_e(z)$ from Eqs. 4.3 and 4.4, the suspended sediment transport for fine sand and larger can be obtained from depth-integrated sediment flow rate given as (Van Rijn, 2003; Camenen and Larroude, 2003):

$$q_t = \int_{-h}^{\eta} u(z)\, C_e(z)\, dz \tag{4.14}$$

where q_t is a total (volumetric) sediment transport rate in the positive x-direction [m/s].

Considering the existing concentration in the water column, the bed change rate can be represented from the depth-integrated transport rate as:

$$\frac{\partial h}{\partial t} = E - D = -\frac{1}{\rho(1-\varepsilon)}\left(\left(\frac{\partial q_{tx}}{\partial x} + \frac{\partial q_{ty}}{\partial x} - D_h\left(\frac{\partial^2 \overline{C}_e}{\partial x^2} + \frac{\partial^2 \overline{C}_e}{\partial y^2}\right)\right) - \frac{\partial \overline{C}_e}{\partial t}\right) \tag{4.15}$$

with: $\overline{C}_e = \int_{-h}^{\eta} C_e(z) dz$ = depth-integrated flux rate [kg/m^2]

where q_{tx} and q_{ty} are components of total (volumetric) sediment transport rate in the positive x and y directions [kg/m.s.], and D_h [m^2/s] is the horizontal dispersion coefficient.

4.3. Cohesive Sediment (Clay [1μm] – Silts [50μm])

For cohesive type of sediment, Whitehouse et al. (2000) assumed that the flocs of cohesive sediment could be treated as low-density grains, when aggregation of flocs, break-up of flocs and water-flow within flocs are neglected. The corresponding formula of settling velocity w_s is given as:

$$w_s = \frac{\upsilon}{d_e}\left\{\left[10.36^2 + 1.049\left(1 - C_f\right)^{4.7} d_*^3\right]^{1/2} - 10.36\right\} \tag{4.16}$$

where: $d_* = d_e\left[\frac{g(\rho_e - \rho)}{\rho\upsilon^2}\right]^{1/3}$ is a dimensionless floc diameter; d_e is the effective diameter of a floc that increases with the volume concentration C of the suspension; ρ is water density; ρ_e is effective density of the floc; C_f is the volume concentration of flocs in water [non-dimension]; and C_k is the mass concentration of the suspension [mass/volume]. Fig. 4.3 shows the settling velocity as a function of cohesive sediment concentration.

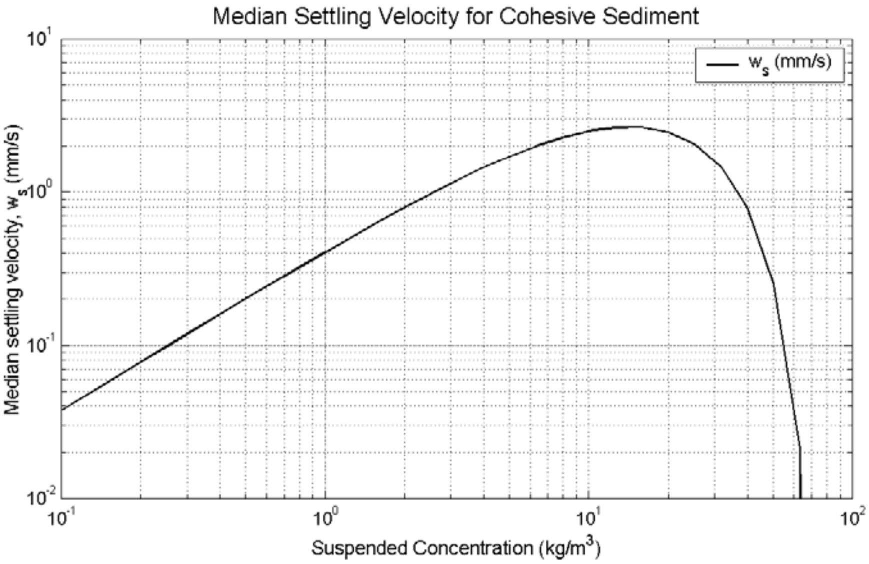

Fig. 4.3. Median settling velocity for cohesive sediment as a function of suspended concentration (After Whitehouse et al., 2000).

Deposition will occur when the bed shear stress is below the critical shear stress for deposition near the bed, whereas a floc of sediment will be resuspended if the bed shear stress too large. The depositional flux rate is computed using the following settling formulation for cohesive sediment (Partheniades, 1990):

$$D = P\, w_s\, C_b \tag{4.17a}$$

where:

$$\text{P = probability of deposition} = \begin{cases} -\left(1-\dfrac{\tau_b}{\tau_{cd}}\right) & for \quad \tau_b < \tau_{cd} \\ 0 & for \quad \tau_b \geq \tau_{cd} \end{cases} \tag{4.17b}$$

w_s = sediment settling velocity (m/s); and τ_{cd} is a critical bed shear stress and is estimated from laboratory tests to be between 0.05 and 0.15 N/m^2 (van Ledden, 2003).

The analysis to estimate the erosion flux rate (*E*) expressed as dry mass of material eroded per unit area per unit time (kg m^{-2} s^{-1}) as a function of shear stress is given by Partheniades (1990b) and Whitehouse et al. (2000):

$$E = m_e\left(\tau_b - \tau_{ce}\right) \quad , \quad \tau_b > \tau_{ce} \tag{4.18}$$

$$E = 0 \qquad\qquad , \quad \tau_b \le \tau_{ce}$$

where m_e is an experimental/site specific erosion constant with m_e is between 0.0002 and 0.002 $kN^{-1}s^{-1}$, and τ_{ce} is the critical bed shear stress for erosion given in Whitehouse et al. (2000) as:

$$\tau_{ce} = 0.015(\rho_b - 1000)^{0.73} \tag{4.19}$$

Typical τ_{ce} is around 0.1-0.2 N/m^2 but it should not exceed 1.0 N/m^2, where ρ_b is the bulk density of the bed over the density range 1000 to 2000 kg/m^3.

4.4. Discretization

The sediment transport formulation slightly differs from the tracer transport. In the concentration formulation, it includes the source and sink terms.

4.4.1. Weighted Residual

The weighted residual method is applied to Eq.4.1 by multiplying each term by a horizontal weighting function ϕ_j and integrating over the horizontal computational domain *Ω* and then multiplying the results by a vertical weighting function ψ_k and integrating over the vertical domain *Z*.

$$\begin{aligned} &\left\langle\left\langle \frac{\partial C}{\partial t},\phi_j\right\rangle_\Omega,\psi_k\right\rangle_Z + \left\langle\left\langle\left(u\frac{\partial C}{\partial x}+v\frac{\partial C}{\partial y}+(\omega-\omega_S)\frac{(a-b)}{H}\frac{\partial C}{\partial\sigma}\right),\phi_j\right\rangle_\Omega,\psi_k\right\rangle_Z = \\ &\quad\left\langle\left\langle\left[\frac{\partial}{\partial x}\left(D_h\frac{\partial C}{\partial x}\right)+\frac{\partial}{\partial y}\left(D_h\frac{\partial C}{\partial y}\right)\right],\phi_j\right\rangle_\Omega,\psi_k\right\rangle_Z + \left\langle\left\langle\left(\left(\frac{a-b}{H}\right)^2\frac{\partial}{\partial\sigma}\left[D_v\frac{\partial C}{\partial\sigma}\right]\right),\phi_j\right\rangle_\Omega,\psi_k\right\rangle_Z \end{aligned} \tag{4.20}$$

4.4.2. Horizontal Integration

Following rules provided by *Luettich and Westerink* (2003) for solving *u* and *v*, the horizontal discretization of salinity equation for each term yields:

- Horizontal integration of the *transient* term in Eq.4.20:

$$\left\langle \left\langle \frac{\partial C}{\partial t}, \phi_j \right\rangle_{\Omega}, \psi_k \right\rangle_{Z} = \frac{A_{NEj}}{3} \left\langle \frac{\partial C}{\partial t}, \psi_k \right\rangle_{Z} \tag{4.21a}$$

- Horizontal integration of the *horizontal advection* term in Eq.4.20:

$$\left\langle \left\langle \left(u \frac{\partial C}{\partial x} + v \frac{\partial C}{\partial y} \right), \phi_j \right\rangle_{\Omega}, \psi_k \right\rangle_{Z} = \left\langle \sum_{n=1}^{3} \frac{An}{3} \left(u_n \frac{\partial C_n}{\partial x} + v_n \frac{\partial C_n}{\partial y} \right), \psi_k \right\rangle_{Z} \tag{4.21b}$$

- Horizontal integration of the *vertical advection* term in Eq.4.20:

$$\left\langle \left\langle \left((\omega - \omega_S) \left(\frac{a-b}{H} \right) \frac{\partial C}{\partial \sigma} \right), \phi_j \right\rangle_{\Omega}, \psi_k \right\rangle_{Z} = \frac{A_{NEj}}{3} \frac{(a-b)}{H} \left\langle (\omega_j - \omega_{S,J}) \frac{\partial C_j}{\partial \sigma}, \psi_k \right\rangle_{Z} \tag{4.21c}$$

- Horizontal integration of the *lateral diffusion* term in Eq.4.20:

$$\begin{aligned} &\left\langle \left\langle \left[\frac{\partial}{\partial x} \left(D_h \frac{\partial C}{\partial x} \right) + \frac{\partial}{\partial y} \left(D_h \frac{\partial C}{\partial y} \right) \right], \phi_j \right\rangle_{\Omega}, \psi_k \right\rangle_{Z} = \\ &\qquad -\left\langle \left[D_h \sum_{n=1}^{NEj} A_n \left(\frac{\partial C}{\partial x} \frac{\partial \phi_j}{\partial x} + \frac{\partial C}{\partial y} \frac{\partial \phi_j}{\partial y} \right) \right], \psi_k \right\rangle_{Z} \end{aligned} \tag{4.21d}$$

this term is obtained by assuming that the lateral diffusions are zero along external boundary segments.

- Horizontal integration of the *vertical diffusion* term in Eq.4.20:

$$\left\langle \left\langle \left[\left(\frac{a-b}{H} \right)^2 \frac{\partial}{\partial \sigma} \left(D_v \frac{\partial C}{\partial \sigma} \right) \right], \phi_j \right\rangle_{\Omega}, \psi_k \right\rangle_{Z} = -\frac{A_{NEj}}{3} \left(\frac{a-b}{H} \right)^2 \left\langle \frac{\partial}{\partial \sigma} \left(D_v \frac{\partial C}{\partial \sigma} \right), \psi_k \right\rangle_{Z} \tag{4.21e}$$

4.4.3. Vertical Integration

Again, applying a standard one-dimensional vertical integration rule (Luettich, 2002) given in Eqs.3.7 and Eq. 3.8a,b,c to all terms of Eqs.4.21a-e, and multiplication by $3/A_{NEj}$, then vertical discretization of concentration equation for each term yields:

- Vertical integration of the *transient* term in (4.21)

$$\left\langle \frac{\partial C_j}{\partial t}, \psi_k \right\rangle_Z = \sum_{m=1}^{3} \frac{\partial C_{j,k+m-2}}{\partial t} Inm_{k,m} \tag{4.22a}$$

- Vertical integration of the *horizontal advection* term in (4.21)

$$\begin{aligned} &\frac{1}{A_{NEj}} \left\langle \sum_{n=1}^{3} A_n \left(u_n \frac{\partial C_n}{\partial x} + v_n \frac{\partial C_n}{\partial y} \right), \psi_k \right\rangle_Z = \\ &\qquad \frac{1}{A_{NEj}} \sum_{m=1}^{3} \left[\sum_{n=1}^{NEj} A_n \left(u_n \frac{\partial C_n}{\partial x} + v_n \frac{\partial C_n}{\partial y} \right) \right]_{k+m-2} Inm_{k,m} \end{aligned} \tag{4.22b}$$

- Vertical integration of the *vertical advection* term in (4.21)

$$\frac{(a-b)}{H} \left\langle \left(\omega_j - \omega_{S,j}\right) \frac{\partial C_j}{\partial \sigma}, \psi_k \right\rangle_Z = \frac{(a-b)}{H} \left[\begin{array}{l} \left(\dfrac{\partial C_j}{\partial \sigma} \right)_{k-1,k} \left[\left(\omega_{j,k-1} - \omega_{S,j,k-1}\right) + 2\left(\omega_{j,k} - \omega_{Sj,k}\right) \right] Inm_{k,1} \\ + \left(\dfrac{\partial C_j}{\partial \sigma} \right)_{k,k+1} \left[2\omega_{j,k} + \omega_{j,k+1} - 2\omega_{s,j,k} - \omega_{s,j,k+1} \right] Inm_{k,3} \end{array} \right]$$

(4.22c)

- Vertical integration of the *lateral diffusion* term in (4.21)

$$\begin{aligned} &-\frac{3}{A_{NEj}} \left\langle \left[D_h \sum_{n=1}^{NEj} A_n \left(\frac{\partial C}{\partial x} \frac{\partial \phi_j}{\partial x} + \frac{\partial C}{\partial y} \frac{\partial \phi_j}{\partial y} \right) \right], \psi_k \right\rangle_Z = \\ &\qquad -\frac{3}{A_{NEj}} \sum_{m=1}^{3} \left[D_h \sum_{n=1}^{NEj} A_n \left(\frac{\partial C}{\partial x} \frac{\partial \phi_j}{\partial x} + \frac{\partial C}{\partial y} \frac{\partial \phi_j}{\partial y} \right)_n \right]_{k+m-2} Inm_{k,m} \end{aligned} \tag{4.22d}$$

- Vertical integration of the *vertical diffusion* term in (4.21)

$$\begin{aligned} &\left(\frac{a-b}{H} \right)^2 \left\langle \frac{\partial}{\partial \sigma} \left(D_v \frac{\partial C}{\partial \sigma} \right), \psi_k \right\rangle_Z = \\ &\qquad + \left(\frac{a-b}{H} \right)^2 \left(D_v \frac{\partial C}{\partial \sigma} \right) \bigg|_{k=NV} - \left(\frac{a-b}{H} \right)^2 \left(D_v \frac{\partial C}{\partial \sigma} \right) \bigg|_{k=1} - \left(\frac{a-b}{H} \right)^2 \sum_{m=1}^{3} C_{j,k+m-2} KSnm_{k.m} \end{aligned} \tag{4.22e}$$

The free surface boundary condition *(FSBC* at *k = NV)* is given as:

$$\left(\frac{a-b}{H}\right)D_v\frac{\partial C}{\partial\sigma}=-\omega_s\ C_k \tag{4.23a}$$

and bottom boundary condition (*BBC* at *k* = *1*) is given as:

$$\left(\frac{a-b}{H}\right)\left(D_v\frac{\partial C}{\partial\sigma}\right)=E-D+\omega_s C_k \tag{4.23b}$$

where: *E* is the erosion rate, and *D* is the deposition rate.

Thus following vertical integration, Eq. 4.22 becomes:

$$\begin{aligned}
&\sum_{m=1}^{3}\frac{\partial C_{j,k+m-2}}{\partial t}Inm_{k,m}+\frac{1}{A_{NEj}}\sum_{m=1}^{3}\left[\sum_{n=1}^{NEj}A_n\left(u_n\frac{\partial C_n}{\partial x}+v_n\frac{\partial C_n}{\partial y}\right)\right]_{k+m-2}Inm_{k,m}\\
&+\frac{(a-b)}{H}\left[\begin{array}{l}\left(\frac{\partial C_j}{\partial\sigma}\right)_{k-1,k}\left[\omega_{j,k-1}+2\omega_{j,k}-\omega_{s,j,k-1}-2\omega_{s,j,k}\right]Inm_{k,1}+\\ \left(\frac{\partial C_j}{\partial\sigma}\right)_{k,k+1}\left[2\omega_{j,k}+\omega_{j,k+1}-2\omega_{s,j,k}-\omega_{s,j,k+1}\right]Inm_{k,3}\end{array}\right]=\\
&-\frac{3}{A_{NEj}}\sum_{m=1}^{3}\left[D_h\sum_{n=1}^{NEj}A_n\left(\frac{\partial C}{\partial x}\frac{\partial\phi_j}{\partial x}+\frac{\partial C}{\partial y}\frac{\partial\phi_j}{\partial y}\right)_n\right]_{k+m-2}Inm_{k,m}\\
&-\left(\frac{a-b}{H_j}\right)^2\sum_{m=1}^{3}C_{j,k+m-2}KSnm_{k.m}+\left(\frac{a-b}{H}\right)\omega_s C_k\Big|_{k=NV}-\left(\frac{a-b}{H}\right)\left(E-D-\omega_s C_k\right)\Big|_{k=1}
\end{aligned} \tag{4.24}$$

with:

$$\left(\frac{\partial C_j}{\partial\sigma}\right)_{k-1,k}\equiv\frac{C_{j,k}-C_{j,k-1}}{\sigma_k-\sigma_{k-1}}$$

and

$$\left(\frac{\partial C_j}{\partial\sigma}\right)_{k,k+1}\equiv\frac{C_{j,k+1}-C_{j,k}}{\sigma_{k+1}-\sigma_k}$$

4.4.4. Time Discretization:

Eq.4.24 is discretized in time using a two time level explicit scheme at the present (t) and future (t+1) time levels as described below:

Transient term: $\sum_{m=1}^{3} \frac{C_{j,k+m-2}^{t+1} - C_{j,k+m-2}^{t}}{\Delta t} Inm_{k,m}$ (4.25a)

Horizontal advection: $\frac{1}{A_{NEj}} \sum_{m=1}^{3} \left[\sum_{n=1}^{NEj} A_n \left(u_n \frac{\partial C_n^t}{\partial x} + v_n \frac{\partial C_n^t}{\partial y} \right) \right]_{k+m-2} Inm_{k,m}$ (4.25b)

Vertical advection: $\frac{(a-b)}{H_j^t} \begin{bmatrix} \left(\frac{\partial C_j^t}{\partial \sigma} \right)_{k-1,k} \left[\omega_{j,k-1}^t + 2\omega_{j,k}^t - \omega_{s_{j,k-1}}^t - 2\omega_{s_{j,k}}^t \right] Inm_{k,1} \\ + \left(\frac{\partial C_j^t}{\partial \sigma} \right)_{k,k+1} \left[2\omega_{j,k}^t + \omega_{j,k+1}^t - 2\omega_{s_{j,k}}^t - \omega_{s_{j,k+1}}^t \right] Inm_{k,3} \end{bmatrix}$ (4.25c)

Surface downward flux: $-\left(\frac{a-b}{H} \right) \omega_s C_k \Big|_{k=NV}$ (4.25d)

Bottom source/sink flux: $\left(\frac{a-b}{H} \right) \left(E - D + \omega_s C_k \right) \Big|_{k=1}$ (4.25e)

Lateral diffusion: $-\frac{3}{A_{NEj}} \sum_{m=1}^{3} \left[D_j \sum_{n=1}^{NEj} A_n \left(\frac{\partial C^t}{\partial x} \frac{\partial \phi_j}{\partial x} + \frac{\partial C^t}{\partial y} \frac{\partial \phi_j}{\partial y} \right)_n \right]_{k+m-2} Inm_{k,m}$ (4.25f)

Vertical diffusion: $-(a-b)^2 \sum_{m=1}^{3} \left[\beta_1 \frac{C_{j,k+m-2}^{t+1}}{\left(H_j^{t+1} \right)^2} + (1-\beta_1) \frac{C_{j,k+m-2}^{t}}{\left(H_j^{t} \right)^2} \right] KSnm_{k.m}$ (4.25g)

4.4.5. Fully Discretized Equation:

Substituting those equations into Eq.4.24, multiplying by Δt and grouping time levels *t+1* and *t* yields:

$$\sum_{m=1}^{3} C_{j,k+m-2}^{t+1} Inm_{k,m} + \beta_1 \Delta t \left(\frac{a-b}{H_j^{t+1}} \right)^2 \sum_{m=1}^{3} C_{j,k+m-2}^{t+1} KSnm_{k.m} =$$

$$+ \sum_{m=1}^{3} C_{j,k+m-2}^{t} Inm_{k,m}$$

$$- \frac{\Delta t}{A_{NEj}} \sum_{m=1}^{3} \left[\sum_{n=1}^{NEj} A_n \left(u_n \frac{\partial C_n^t}{\partial x} + v_n \frac{\partial C_n^t}{\partial y} \right) \right]_{k+m-2} Inm_{k,m}$$

$$
\begin{aligned}
&-\Delta t\frac{(a-b)}{H_j^t}\left[\begin{array}{l}\left(\dfrac{\partial C_j^t}{\partial\sigma}\right)_{k-1,k}\left[\omega^t_{j,k-1}+2\omega^t_{j,k}-\omega^t_{s_{j,k-1}}-2\omega^t_{s_{j,k}}\right]Inm_{k,1}\\ +\left(\dfrac{\partial C_j^t}{\partial\sigma}\right)_{k,k+1}\left[2\omega^t_{j,k}+\omega^t_{j,k+1}-2\omega^t_{s_{j,k}}-\omega^t_{s_{j,k+1}}\right]Inm_{k,3}\end{array}\right] \qquad (4.26)\\
&-\frac{3\Delta t}{A_{NEj}}\sum_{m=1}^{3}\left[D_j\sum_{n=1}^{NEj}A_n\left(\frac{\partial C^t}{\partial x}\frac{\partial\phi_j}{\partial x}+\frac{\partial C^t}{\partial y}\frac{\partial\phi_j}{\partial y}\right)_n\right]_{k+m-2} Inm_{k,m}\\
&-(1-\beta_1)\Delta t\left(\frac{a-b}{H_j^t}\right)^2\sum_{m=1}^{3}C^t_{j,k+m-2}KSnm_{k.m}\\
&+\Delta t\left(\frac{a-b}{H}\right)\omega_s C_k\Big|_{k=NV}-\Delta t\left(\frac{a-b}{H}\right)(E-D)\Big|_{k=1}-\Delta t\left(\frac{a-b}{H}\right)(\omega_s C_k)\Big|_{k=1}
\end{aligned}
$$

Then, the C_j^{t+1} in LHS of Eq.4.26 can be solved in matrix form using tridiagonalize matrix method formulated in Eq. 3.15.

4.5. Model Validation

For model validation of non-cohesive type sediment transport, the model is compared with an analytical model provided by Van de Kreeke et al. (2002). The initial cross section of the trench in the Van de Kreeke formulation is approximated by a Gaussian distribution:

$$
d=\frac{A}{\sqrt{2\pi}\sigma_o}e^{-x^2/2\sigma_o^2} \qquad (4.27)
$$

where d is a depth of the trench relative to the surrounding sea bottom, A is the cross sectional area of the trench, and σ_o is the half-width of the initial cross section.

The model domain is a long-flat rectangular channel with uniform depth 3m, and 5 m deep of a ‘Gaussian shape’ trench located across the channel width in the mid point of the channel. The model is driven by the 0.5 m amplitude of M2 tide on the left side and an influx normal flow 0.5m/s from the right downstream to the left. The M2 tidal range is required to generate the M2 tidal current. Investigating the model results, the maximum amplitude of M2 tidal current on the shelf around the trench is 0.12m/s. The comparison of the deposition and erosion at the bottom across the trench for median grain size 0.3mm is shown in Fig.4.4. The top figure shows the amount of erosion (-) and deposition at 5 days.

There is good agreement in the magnitude of both erosion and deposition; however there are also shifts of deposition and erosion, where the erosion occurs shifted to the left and the deposition shifted to the right. The bottom figure represents the change of the bathymetric depth relative to its initial depth profile (gray-thin line). Van de Kreeke (2002) assumes that the water level is assumed uniform across the channel, so the solution will be symmetric between erosion and deposition.

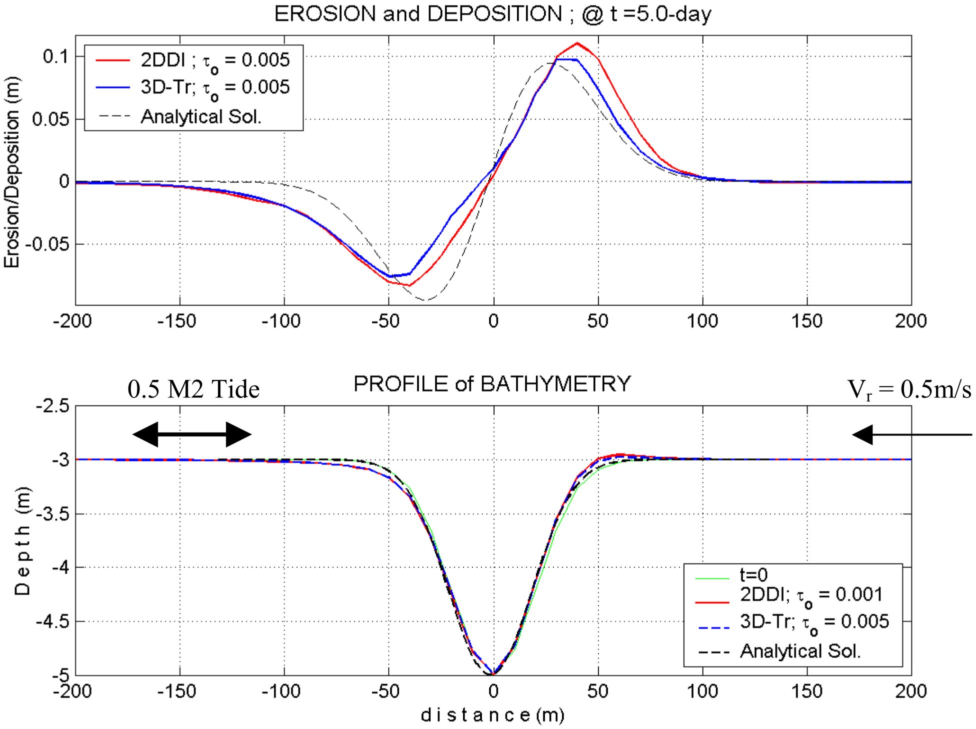

Fig. 4.4. Comparison of erosion and deposition of non-cohesive sediment for d_{50}=0.3mm between ADCIRC 3D, ADTRANS-2DDI and Van de Kreeke's analytical models.

The assessment on the model indicates that the water level and velocity in both edges of the channel are not uniform (figure is not shown). The water level in the edge of the upstream direction is slightly higher than the downstream site, thus, the velocity in the downstream site is slightly higher than the upstream site to the order of 0.07m/s. The erosion and deposition magnitudes are calculated by Eq. (4.15). This velocity difference may drive different amounts of suspended sediment C_e between both sides. Thus, considering the transport balance, the erosion is more likely to occur more in the downstream site than in the upstream. Consequently, the velocity difference across the channel may explain the discrepancies between the model and the analytical models.

The comparison was also made against the ADCIRC-Transport (ADTRANS) 2DDI version (Scheffner, 1999). The 3D result slightly improves the magnitude of erosion and deposition closer to the analytical model. Both models, however, over-estimate the magnitude of deposition in the channel upstream direction and erosion in the downstream direction.

4.6. Conservation of Mass for Sediment

To test the reliability of the model to simulate transport, a simple sloped-bottom rectangular domain with a shallow bar located in the middle of the basin was developed as given in Fig.4.5. The open ocean boundary is located in the left (west) side of the domain; the normal flow boundary is located in the right (east) side, while the other two sides are defined as mainland (solid) boundaries. The dimensions are 12 km long and 4 km wide, with a 1 m sand bar located between 8 and 9 km from the ocean boundary. The bay dimension behind the bar (x = 9 - 12 km) has uniform depth of 2.5m, while from the bar to the open ocean boundary slopes from 1m to 20m over 8 km. The triangular grid size was specified to be 125m along the x-axis and 250m along the y-axis, giving the number of nodes and elements of 1699 and 3079, respectively. Nine vertical layers are implemented in this simulation which are distributed uniformly in the vertical σ-layers from $\sigma = b = -1$ at the bottom to $\sigma = a = 1$ at the surface.

The grid was selected for the analysis of the conservation of mass for the sediment transport. To assess the conservation of mass for non-cohesive sediment, the simulation is driven with constant velocity of 0.6 m/s of normal inflow, and zero tide at the open

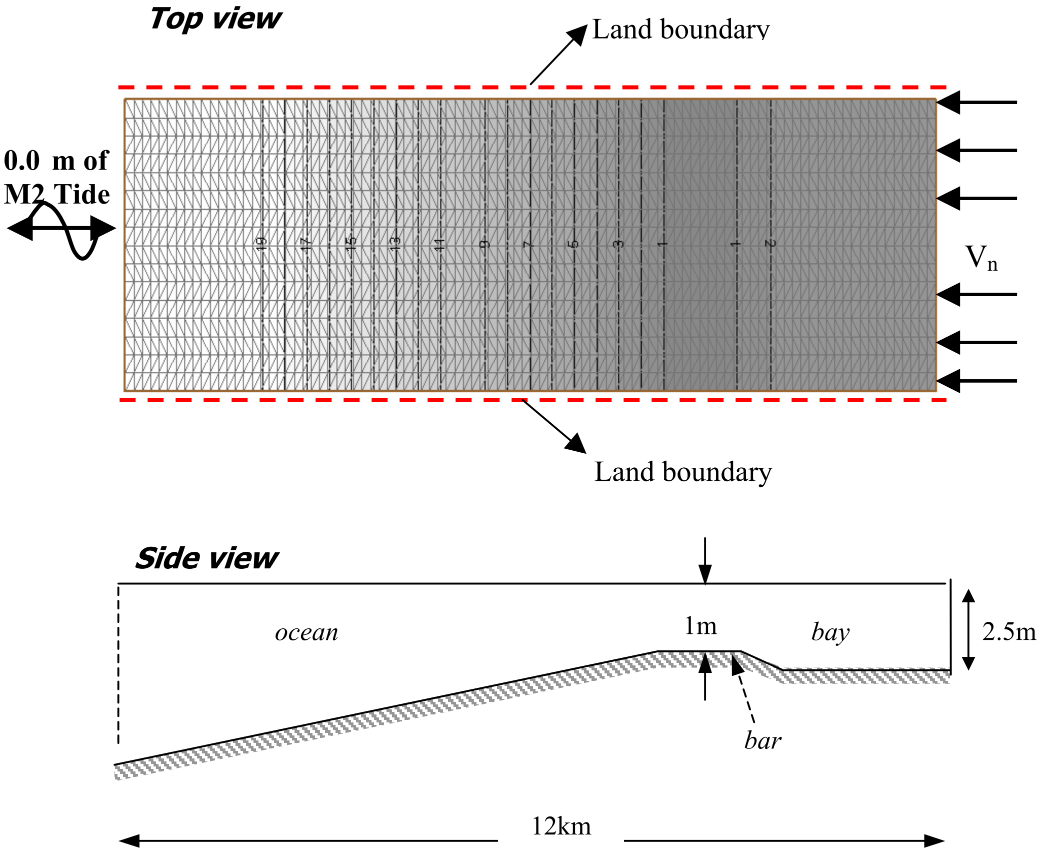

Fig.4.5. The configuration of barred rectangular basin. (Upper) The grid consists of 1699 nodes and 3079 elements and the bathymetric depth varies from 1.0 m to 19.0 m. Open ocean and normal flow boundaries are specified on the left and right side, respectively. (Lower) The side view of the basin, 12km long and 4km wide.

boundary. Starting at the bottom slope of the bar, velocity will increase causing the increase of the bottom stress. Erosion occurs when the bottom shear stress τ_b has exceeded the critical shear stress for erosion τ_{ce}. For this case, erosion occurs starting near the top of bayside slope of the bar, continuously along the bar to the other tip of the bar. Fig.4.6 shows the results of the along-basin vertical profile of the sediment transport for a 3-day simulation for a non-cohesive sediment type with a uniform grain size (d_{50}) of 0.1 mm. The profiles represent the mid-line of the basin (i.e. y=2000m).

As shown in Fig.4.6a, the distribution of suspended sediment taken arbitrarily at time t = 78-hour simulation. The suspended sediment due to erosion is mostly contained near the bar. Arrows indicate the direction and magnitude of three dimensional flow components. Using Eq.4.10, the settling velocity of 0.1mm grain size is ~0.6 mm/s or ~2.2m/hr. The existing very shallow bar of one meter produces a maximum horizontal velocity of about 1.1m/s near the left tip of the bar where the maximum erosion occurs. With these conditions, it is expected that the suspended sediment will not be advected far after it has been suspended into the water column. The deposition process occurs immediately after τ_b is less than τ_{cr}. The corresponding profile of erosion and deposition is given in the bottom Fig.4.6.

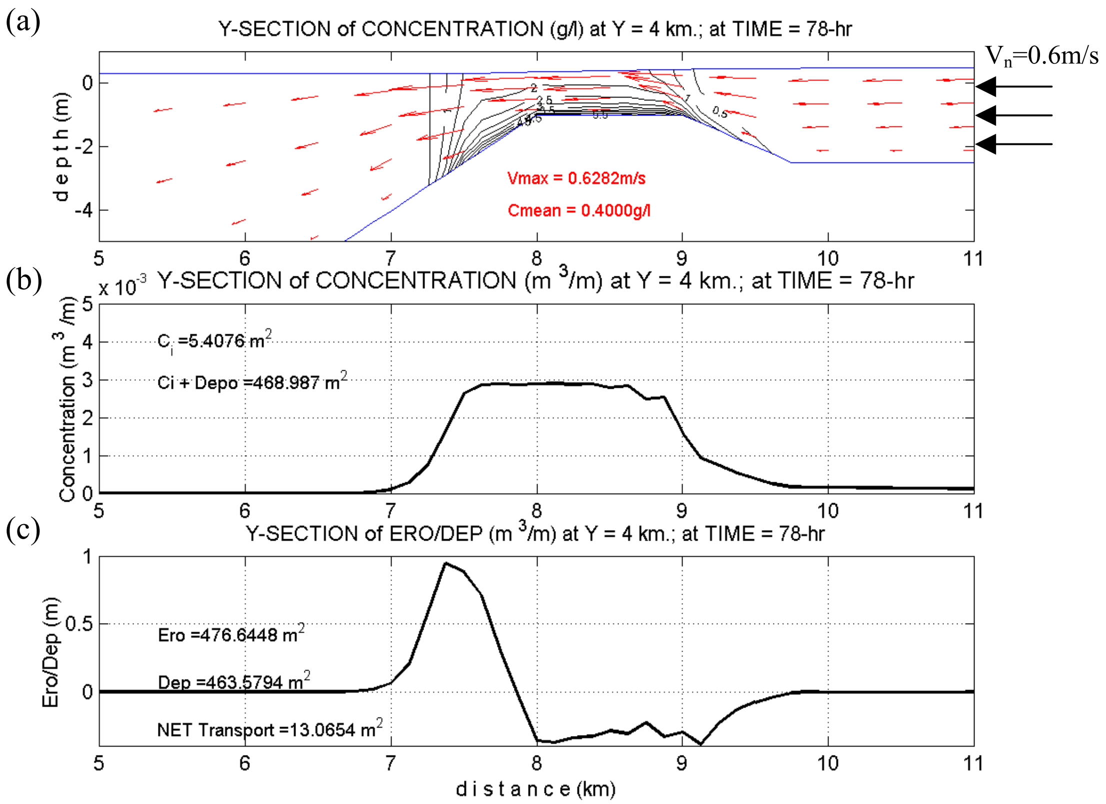

Fig. 4.6. Profile of non cohesive sediment transport, with d_{50} = 0.1mm and t = 78h. (a) Contour plot of suspended sediment concentration with arrows representing the relative magnitude and direction of current velocity. (b) Depth integrated concentration along the profile in term of m^2/m, and (c) the corresponding erosion (-) and deposition (+) along the profile line.

Fig.4.6b describes the depth-integrated concentration (C_i) of suspended sediment in the water column at each node. The concentration units in g/l in Fig. 4.6a is integrated in vertical and lateral directions, and then converted to volume given in units of m^2 (Fig. 4.6b), which represents the mass volume per width (m^3/m). Assuming the distribution of transport is uniform across the basin, the simple way to estimate the conservation of mass is to compute the area along the profile with the expected relationship:

$$Erosion\ (m^2) = Depth\ integrated\ suspended\ sediment\ (m^2) + Deposition\ (m^2) \tag{4.23}$$

Thus, from Fig.4.6c the sum of C_i + *Depo* should equal to *Ero*, but the results are not perfectly met. The finite element method for solving the governing equations is usually conserved locally, but not globally. Small numerical rounding errors might propagate from element to element and develop accountable errors. Conversion of a vertical reference from z- to σ-level can introduce another source of conservation errors as it was discussed in Mellor et al. (1998).

In this case, the error was 9.6m^2 of 476.6 m^2 eroded material or about 2.0% of the total transported mass. The error of conservation of mass is mostly less than 6%, especially in the sloping bottom. The sources of the error are commonly due to accumulated numerical “round off” either from hydrodynamic or transport modules.

For the cohesive sediment type, a similar way of assessment for conservation of mass is applied in the same grid and bathymetric configuration, but larger V_n = 1.0m/s. The results are given in Fig.4.7 at time t = 28-hour. The erosion is arbitrarily stopped after 24-hour, then it is expected that the amount of depth-integrated suspended sediment plus deposited sediment must be constant. It is known that the property of cohesive sediment in a bed is very easily eroded when τ_b exceeds τ_{cre}. It is then suspended, transported a relatively long distance, and deposited back to a bed at particular location whenever the τ_b is less thanτ_{crd}. The amount of suspended sediment is high and settles more slowly due to slow settling velocity as given in Eq.4.16.

At time t=28-hour, it is seen that the conservation of mass coincidently is better than the non-cohesive sediment. In Fig.4.7a, initial erosion occurs around the bar, and after the erosion is arbitrarily forced to stop at t=24h, the cloud of cohesive suspended sediment travels offshore while the particles tend to settle down. Thus, the prevailing sediment concentration should be high at near bottom decreasing upward to the surface. The error in this simulation is less than 1% of the transported mass volume. The error of conservation of mass for cohesive sediment is usually less than 2%, especially in the sloping bottom.

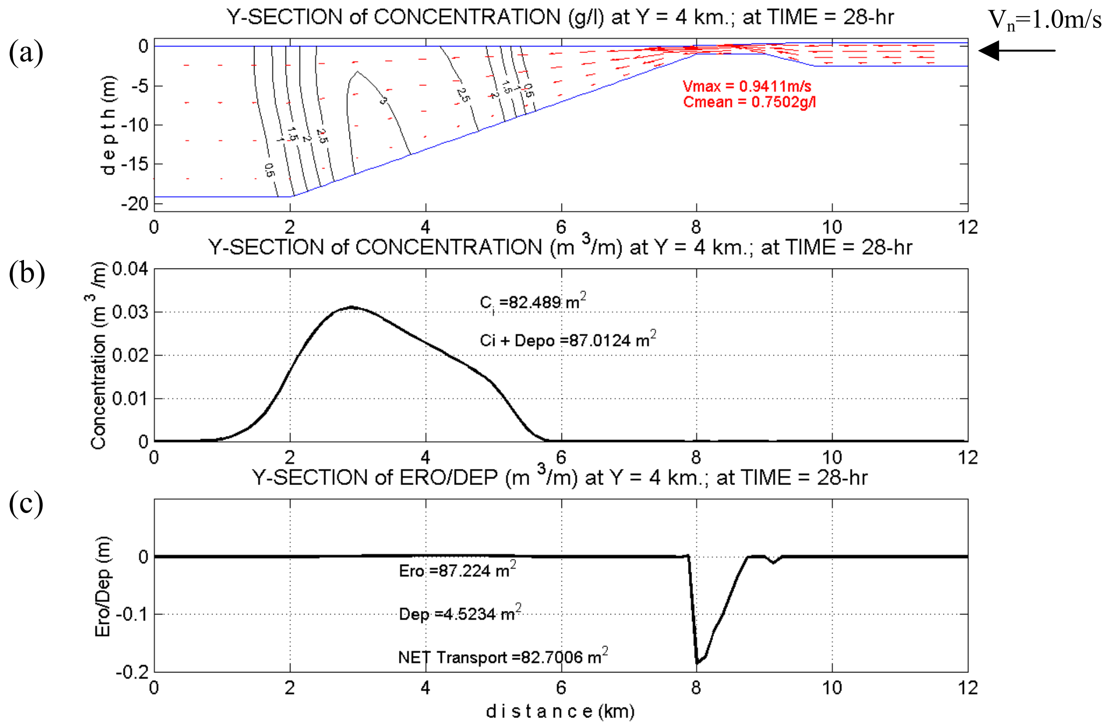

Fig.4.7. Profile of cohesive sediment transport taken at time t = 28-h. (a) Contour plot of suspended sediment concentration with arrows representing the relative magnitude and direction of current velocity. (b) Depth integrated concentration along the profile in term of m^2/m, and (c) the corresponding erosion (-) and deposition (+) along the profile line.

4.7. Barotropic Versus Baroclinic Modes

Coupling the baroclinic hydrodynamic circulation and sediment transport in the stratified water is the main goal of this study. A comparison between barotropic and baroclinic sediment transport is performed to assess the importance of the baroclinic term.

4.7.1 *Barotropic Mode*

Fig.4.8a describes a snapshot taken at t=48-h of the salinity contour of barotropic only transport for cohesive type sediment. The setup configuration of the model is similar to the previous cases with the barred rectangular basin; however, the open boundary is driven with 0.5 m M2 tidal amplitude, normal flow V_n = 0.4 m/s, and the erosion occurs continuously. The freshwater discharge from the normal flow boundary on the right,

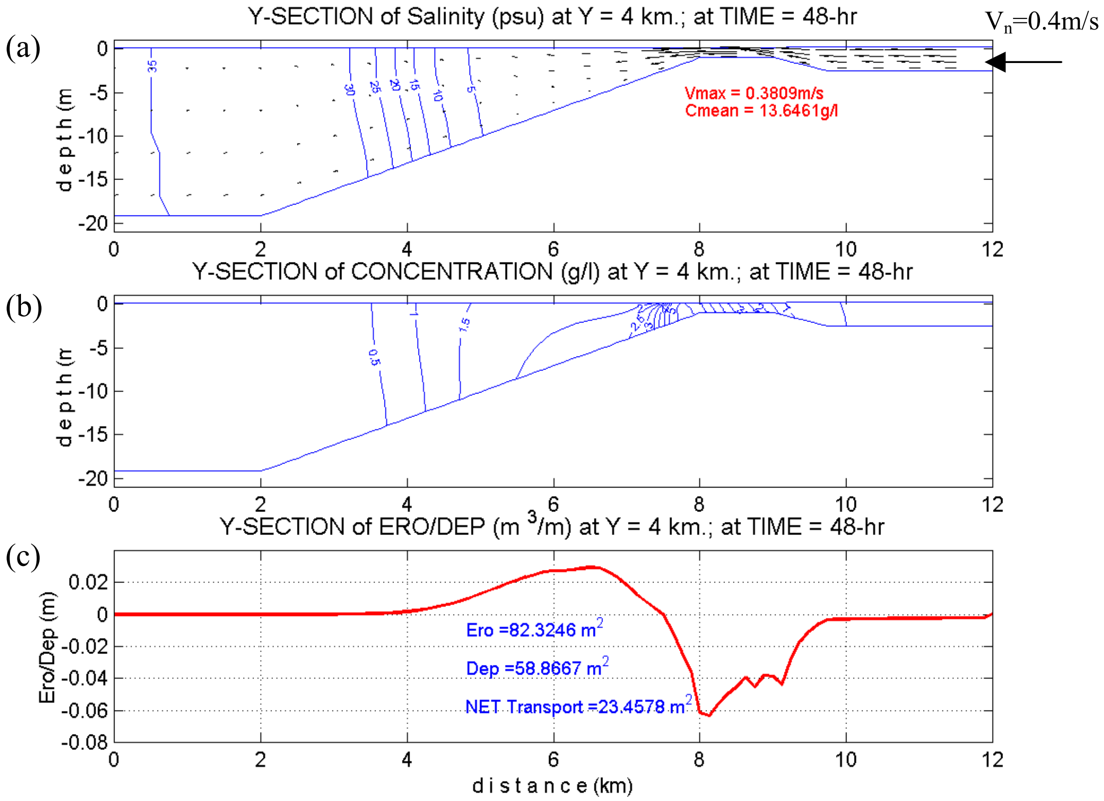

Y-SECTION of Salinity (psu) at Y = 4 km.; at TIME = 48-hr

Y-SECTION of CONCENTRATION (g/l) at Y = 4 km.; at TIME = 48-hr

Y-SECTION of ERO/DEP (m ^{3}/m) at Y = 4 km.; at TIME = 48-hr

Fig.4.8. Profile of cohesive sediment transport, barotropic mode, taken along the midline of the domain rectangular basin at time t = 48-h. (a) Contour plot of salinity in psu unit with arrows represent the relative magnitude and direction of current velocity. (b) Contour plot of suspended sediment concentration, and (c) the corresponding erosion (-) and deposition (+) along the profile line.

propagates towards the onshore direction in nearly vertically uniform transport, indicated by the uniform salinity (i.e. density) distribution.

Consequently, the eroded cohesive sediment along the top of the bar is also suspended with a nearly uniform transport. However, persistent settling velocity which takes place during the transport causes higher concentration near the bottom immediately after it is suspended (Fig.4.8b). Combined with the diffusion and vertical advection occurring during the horizontal transport, the sediment distribution is likely to become uniform at a location far away from its origin. Here, the critical stresses for erosion (τ_{ce}) and deposition (τ_{cd}) are 0.2 N/m^2 and 0.1 N/m^2, respectively.

The three-dimensional hydrodynamic model applies a one-day ramp function to reach its designed hydrodynamic flows. The initial erosion had occurred before the full ramp function is achieved, and the site of deposition is at some distance offshore from the erosion site due to the difference in the τ_{ce} and τ_{ce}. After the hydrodynamic ramp function, the erosion site is shifted further offshore than previously. Since the erosion and deposition processes occur almost continuously, as shown in Fig.4.8c, continuous erosion followed by immediate deposition offshore is a probable result.

4.7.2 Baroclinic Mode

Another simulation was performed similarly to the formerly discussed case with similar setup and configuration; however, both the baroclinic and barotropic terms were activated, hence so-called *baroclinic mode*. It generates a significant difference in the mechanism of sediment transport, especially for the cohesive type sediment. Due to fresh water (S=3psu) discharge from the normal flow boundary on the right side of domain into the saline ocean water (S=35 psu), the presence of stratification is clearly seen when the baroclinic term is activated (Fig.4.9a).

The tip end of the saline wedge is located in the x-axis between 6 and 6.5 km. At the tip of saline wedge, the near bottom horizontal velocity is small, but upward vertical velocity increases causing the near bottom sediment to either settle down or be lifted up. In this case of cohesive sediments, the concentration of the suspended sediment is small, thus the settling velocity is relatively smaller than its vertical lift velocity. Once the sediment is suspended and lifted up, the path of transport will be mainly driven by baroclinically hydrodynamic flow, which causes a cloud of suspended sediment concentrated in the top layers (Fig.4.9b). The suspended sediment cloud will be either carried away outside of the domain or deposited at some point further away offshore.

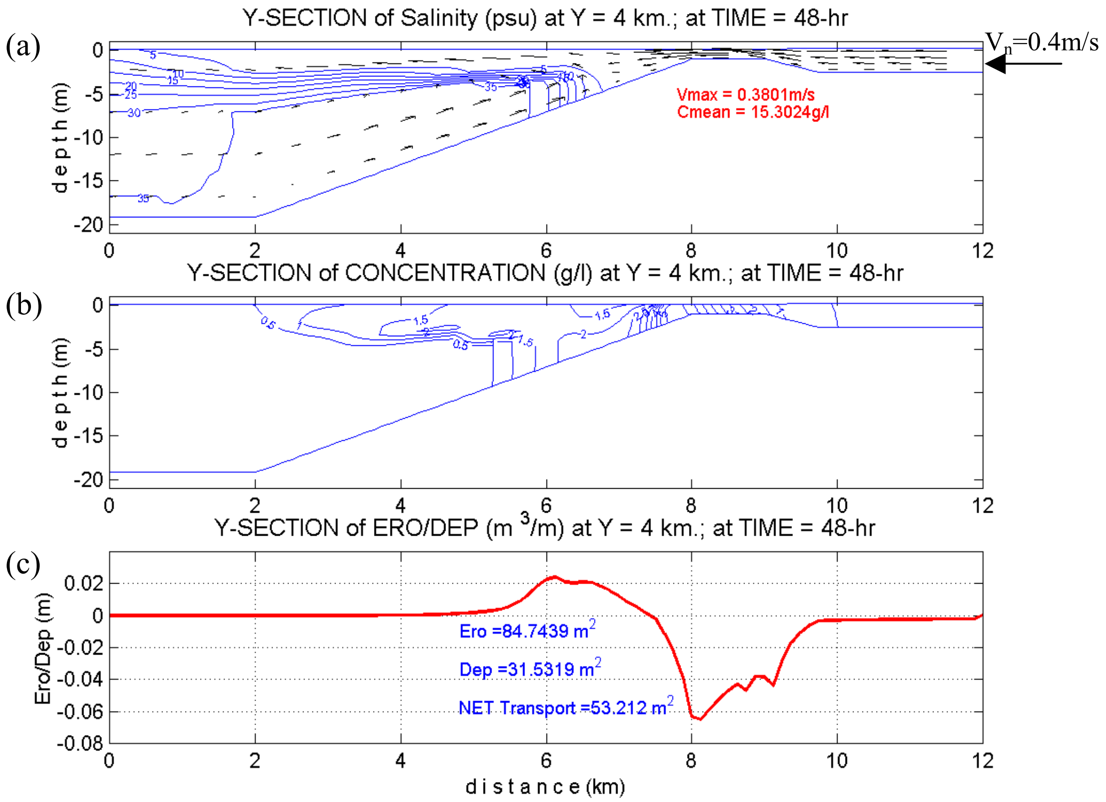

Fig.4.9. Profile of cohesive sediment transport in baroclinic mode taken at time t = 48-h. (a) Contour plot of salinity in psu unit with arrows represent the relative magnitude and direction of current velocity. (b) Contour plot of suspended sediment concentration, and (c) the corresponding erosion (-) and deposition (+) along the profile line.

The processes of erosion and deposition around the top of the bar are almost similar to the barotropic case; however at point x = 5.8 – 6.2 km in Figs.4.9c and 4.10c, it is shown that less deposition occurs in the baroclinic case around the tip of saline wedge. Some amount of suspended sediment is raised up, becoming a cloud of upper layer suspended sediment. The amount of erosion, deposition, and net sediment transport between them is summarized in Table 4.1. Therefore, in this case, the inclusion of the baroclinic term may transport the cohesive suspended sediment more than 60% of eroded materials, meanwhile the barotropic only model transports only about 28% of eroded materials.

Table 4.1.
Comparison of sediment transport between barotropic and baroclinic transport at t= 48-h.

Mode	Erosion (m^3/m)	Deposition (m^3/m) (% of erosion)	Net Transport (m^3/m) (% of erosion)
Baroclinic	84.744	31.532 (37%)	53.212 (63%)
Barotropic only	82.325	58.867 (72%)	23.456 (28%)

CHAPTER V

CASE STUDIES

Based on the development of the extended ADCIRC 3D with the Baroclinic Transport, three ideal case studies are performed to assess the capability of the numerical model. These three cases are: (1) River discharge, (2) Tidal Inlet, and (3) Capping erosion due to combined wave and current. Discussion hereafter will explore the model simulations and results for each case.

5.1. River Discharge

The simulation of idealized river discharge demonstrates the model ability to trace the suspended cohesive sediment as the fresh water river outflow mixes with the saline ocean water. The domain and grid for this numerical case is similar to the one given in Chapter III Fig. 3.6. The river discharges fresh water and suspended sediment with concentration C_n = 0.5 g/l, flow velocity V_n = 0.2 m/s, and salinity S_n = 3 psu. The initial conditions in the domain are 0.0 g/l for suspended sediment concentration and 35 psu for salinity. The model is driven by 0.1m amplitude of M2 tide. The vertical domain consists of 9 equally spaced σ-layers from $\sigma = -1$ at the bottom to $\sigma = 1$ at the surface.

The water salinity difference between the river outflow and the ocean, and the small M2 tide amplitude generates density stratification, which is mostly seen around the river-ocean system. The penetrating saline wedge discussed in Chapter III provides the existing strong stratification. Fresh water is mostly contained in the upper surface, with the saline water underneath.

As the downstream flow of the river goes to the ocean, the generated baroclinic force will counter act the flow to the upstream direction. Assuming the case located in the northern hemisphere, the balance between the baroclinic pressure gradient and the Coriolis force drives the deflected flow northward, so called geosttrophic flow (Pond and Pickard, 1995). This flow becomes a northward longshore salinity transport. Fig. 5.1a

(a) Salinity @ σ = 9 (Surface) **;** t = 10-d

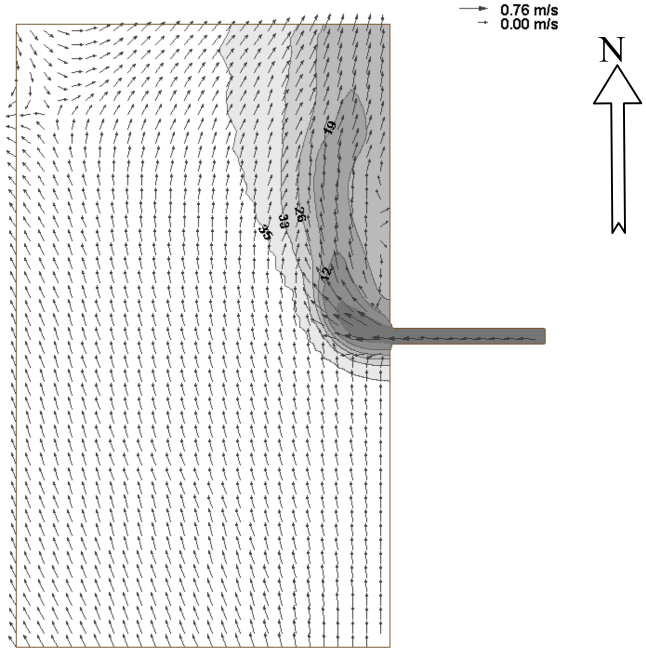

(b) Salinity @ σ = 1 (Bottom)

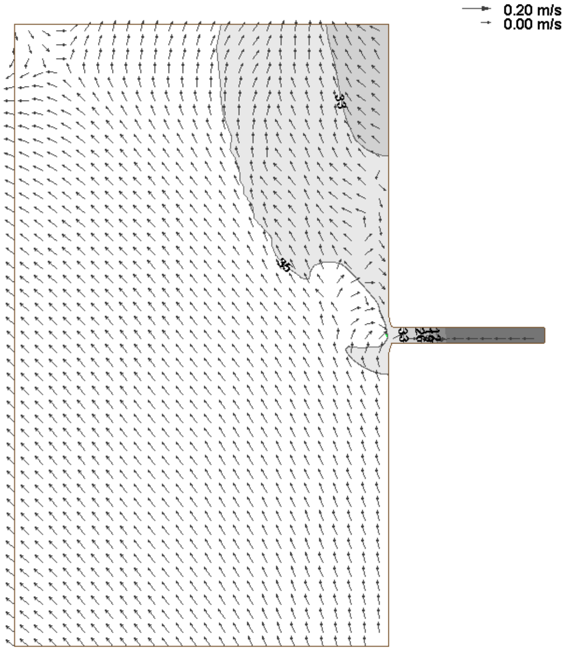

Fig. 5.1. Snapshots for contour of salinity (psu) at t = 10-day simulation for (a) at surface layer (σ = 9), and (b) at bottom layer (σ = 1). Arrows represent the relative magnitude and direction of flow for each corresponding layer.

shows a northward brackish tongue at the surface layer taken at t = 10-day simulation. The fresh water is mostly contained only around the river mouth. Water mixing occurs and the salinity increases as the transport propagates towards the north.

On the other hand, the ocean saline water persists in the lower layers penetrating the river upstream. Fig. 5.1b exhibits a salinity distribution at the bottom layer in the domain where the saline ocean water, S > 31 psu, exists in whole domain, while the relatively fresher water is contained along the river.

A three-dimensional view for salinity distribution at t = 10-day is provided in Fig. 5.2. It clearly shows the northward transport of tongue brackish water with salinity less than 26 psu in the upper half vertical layers. The fresh water with salinity less than 5 psu (yellow color) covers the top layers along the rivers and flows offshore near the river mouth before it mixes with the saline water. The saline wedge penetrates deep into the near shore in the lower layers. Unfortunately the upstream penetration of the saline wedge along the river is difficult to show in the figure.

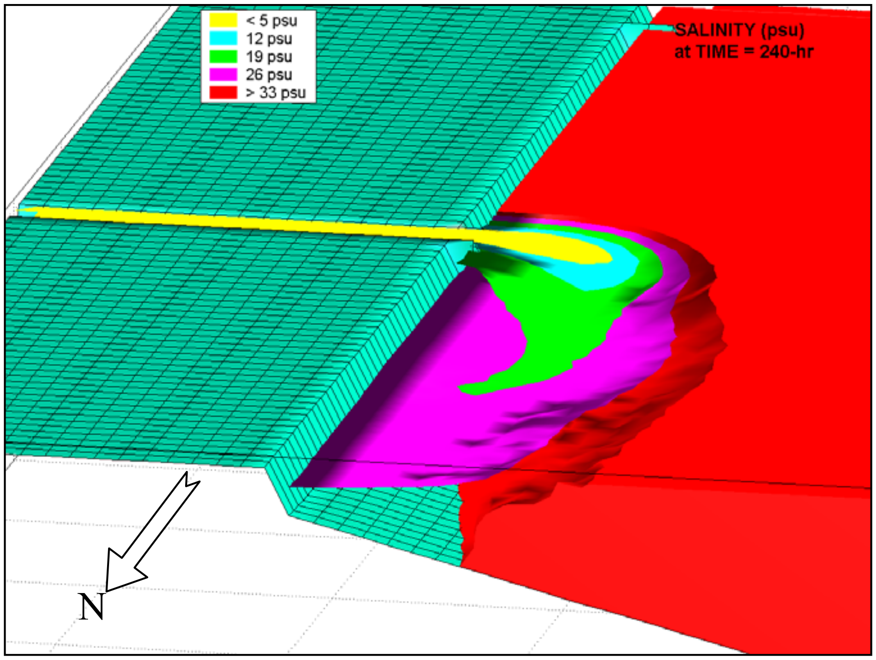

Fig. 5.2. Three-dimensional view from north side looking south of salinity distribution taken at t= 10-day simulation.

The corresponding suspended cohesive sediment concentrations after a 10-day simulation at the surface (σ=9) and at the bottom (σ=1) are given in Fig. 5.3a and Fig. 5.3b, respectively. The figures clearly provide a northward longshore sediment transport with higher suspended concentration near the bottom and decreasing upward.

At time t = 10-day, the combination of longshore flow and prevailing settling velocity for sediment are not strong enough to force the tongue of suspended sediment at the surface into further transport, but instead settles it down to the lower layers. The relatively high surface concentration of 100 mg/l discharged from the river decreases immediately down to 10mg/l as the sediment is transported northward. On the other hand, the suspended sediment concentration near the bottom consistently propagates much further along the shore. The highest concentrations are mostly located near the shore due to the force of the existing baroclinic term in the lower layers. The concentration near the shore, up to 30mg/l, is uniformly distributed along the shore, and less concentration prevails offshore.

In the river, the available concentration of 500 mg/l is limited from the null point upstream. The strong gravitational circulation around the null point due to the presence of the longitudinal salinity gradient causes the sediment to be lifted up and transported in the upper layers.

Interpolation from an unstructured to a structured rectangular grid was performed to generate a structured matrix for a three-dimensional view (See Appendix B). The three-dimensional views from two different view azimuths are shown in Fig. 5.4a,b for azimuths -45°N and 125°N, respectively. A high concentration of suspended sediment greater than 400 mg/l (red color) is mostly contained in the river upstream with a down sloping end around the saline wedge point. A relatively high concentration down to 200 mg/l (magenta color) exists from that point down stream to the river mouth. Upon discharging from the river, the concentration of sediment mixed with the ocean water decreases immediately, whereas the path of sediment transport is deflected to the north due to the Coriolis force.

(a) Concentration of Suspended Sediment @ σ = 9 (Surface)

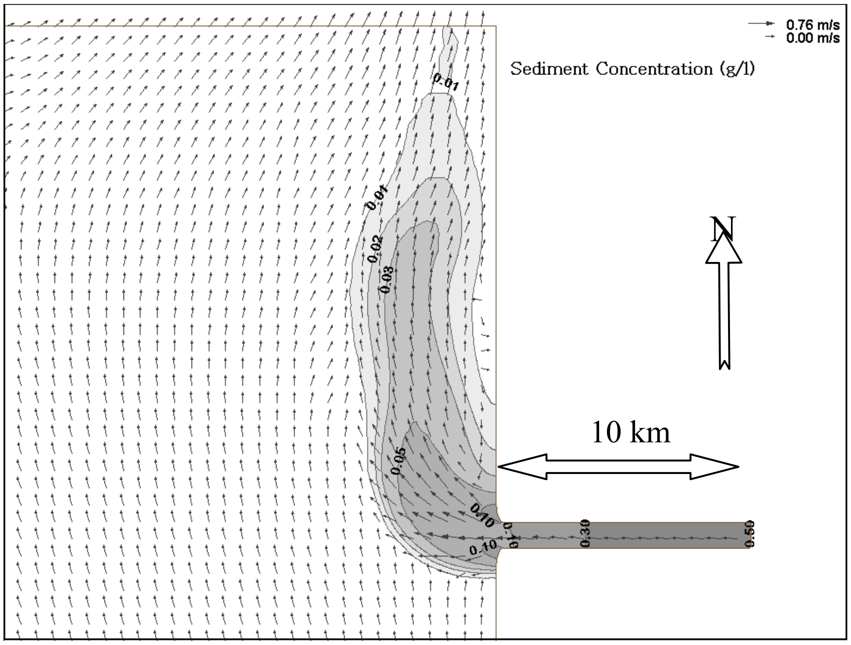

(b) Concentration of Suspended Sediment @ σ = 1 (Bottom)

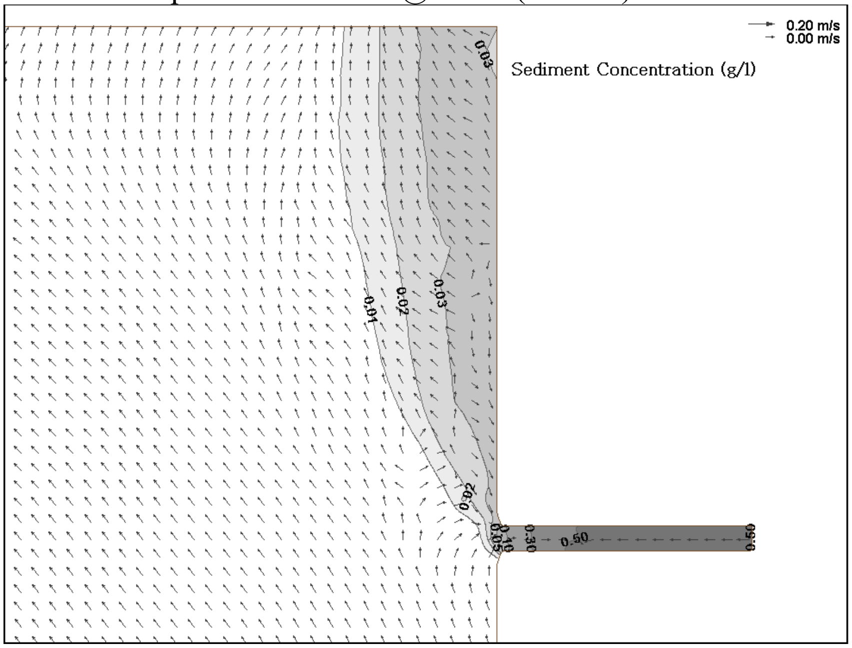

Fig. 5.3. Snapshots for contour of salinity (psu) at t = 10-day simulation for (a) at surface layer (σ = 9), and (b) at bottom layer (σ = 1). Arrows represent the relative magnitude and direction of flow for each corresponding layer.

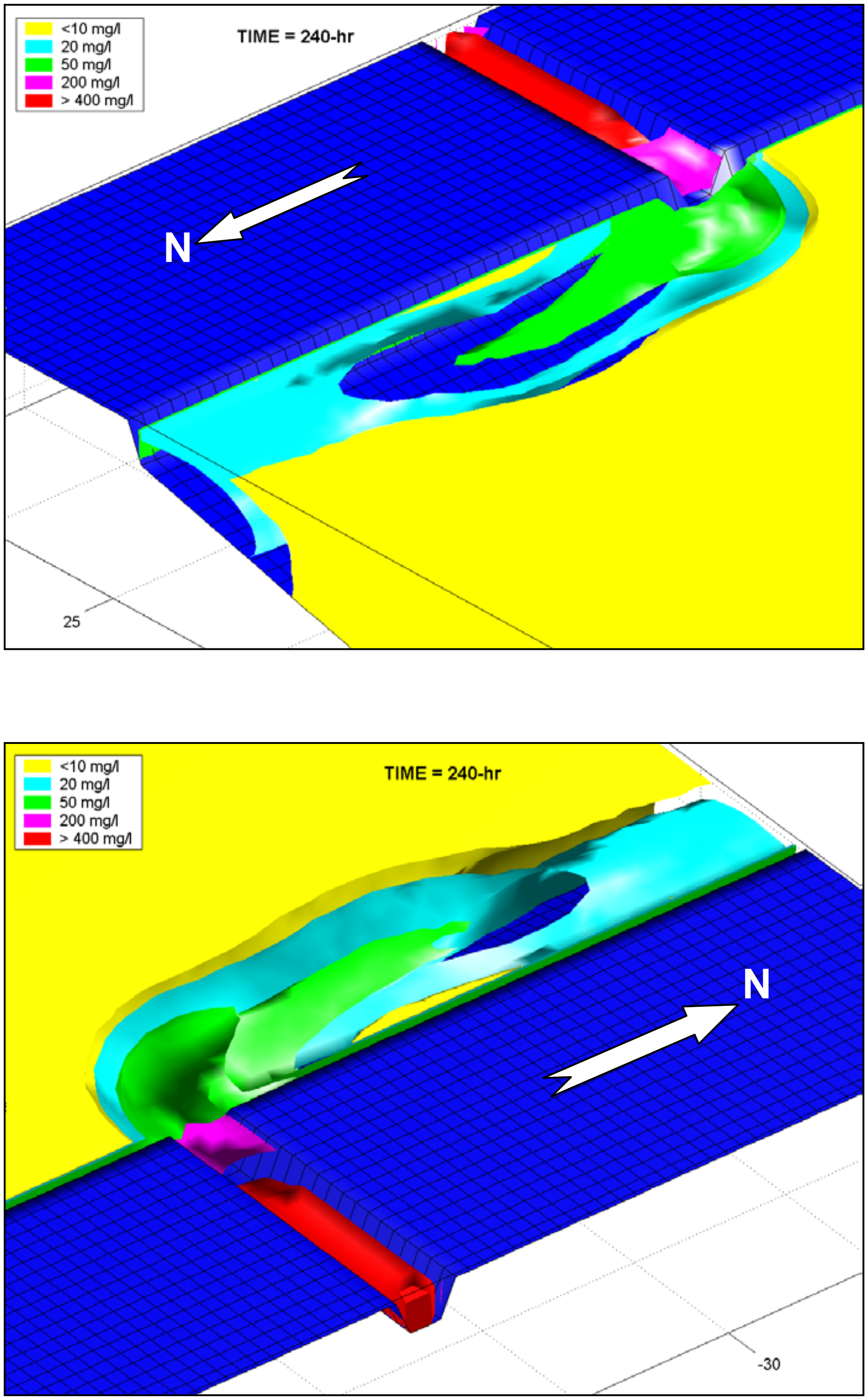

Fig. 5.4. Three-dimensional view of suspended sediment concentration (mg/l) taken at t=10-day simulation. (a) Viewed from northeast (Az = -45°N) looking southeast, and (b) viewed from southeast northeast (Az = 125°N) looking northwest.

After a 10-day simulation, the concentration of 50 mg/l (green) reaches up to 8 km northward nearly along the coastline, and the lower concentration down to 20 mg/l (cyan) propagate further northward out of the domain. The width of the concentration tongue is about 6km offshore. The three- dimensional plots shown here may demonstrate another way to analyze the three-dimensional sediment transport.

Correlating to Fig. 3.10, the limit of considerably higher concentration of suspended sediment greater than 400 mg/l marks the location of the limit of the arrested saline wedge or null point. The zero or relatively small velocity around the null point causes the sediment to settle and deposit around this point. It is shown in Fig. 5.5 that the higher deposition content at the seabed is located around the head of the salt intrusion. The

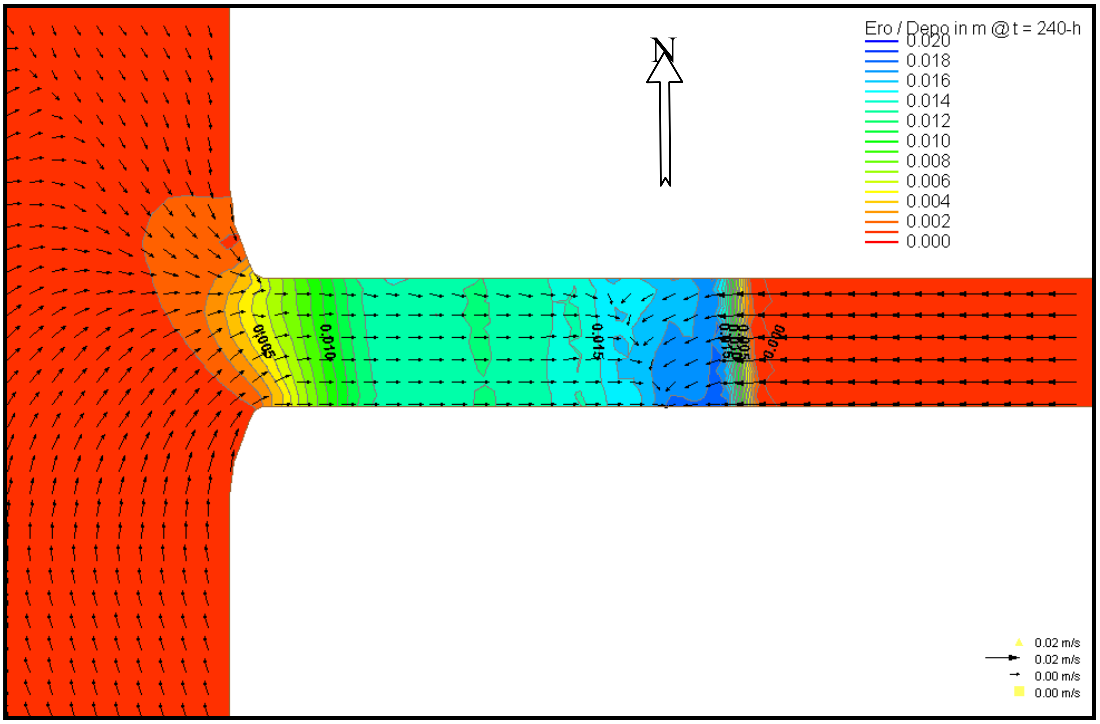

Fig. 5.5. Occurring deposition at bottom along the river after 10-day simulation. Arrows indicate the near bottom flow direction.

suspended sediment settles due to gravity, and it may reach a lower layer and be transported to the convergence null point. The location of the high deposition is relatively wide since the location of the maximum of the near bottom concentration is not fixed, but varies during the tide.

Another interesting point in Fig. 5.5 is the presence of the highest deposition occurring in the south, rather than being distributed symmetrically across the river. If one assumes in the Northern hemisphere, the Coriolis force deflects the water to the right, which may increase the net flow in the north part of the river, causing considerably higher velocity in the north part than in the south part. Less velocity in the southern part of the river causes the suspended sediment to settle and to be deposited more than in the northern part.

5.2. Tidal Inlet

The case of idealized tidal inlet was performed to simulate the behavior of sediment transport with baroclinic mode in an idealized tidal inlet with the domain shown in Fig. 5.6. The ocean grid dimension is 24 km alongshore and 24 km from the shoreline to the ocean boundary. The inlet length and width are 1.5 km and 1.125 km, respectively. The bay dimensions are 5 km x 8 km, with uniform depth of 2 m. The ocean depth was specified 2 m along the shoreline down to 20 m along the open boundary. The triangular grid sizes were specified to be 75 m around the inlet, gradually increasing toward the open boundary to 1500 m. The final grid contains 2397 nodes with 4575 triangular elements.

The model is driven with semidiurnal M2 tide with 0.4 m tidal amplitude at the open ocean boundary. The north and south border of the domain are defined as the normal radial wave boundaries with no constraints applied along those two boundaries. The coastlines to the north and to the south of the inlet, around the inlet, and to the north and south of the bay are defined as the mainland boundaries. Essential normal flow boundary conditions are applied along the east side of the bay, with constant normal velocity $V_n = 0.1$ m/s. The vertical is divided into 9 σ-layers that are uniformly distributed from bottom to the surface as $\sigma = [-1, -0.75, -0.5, -0.25, 0.0, 0.25, 0.5, 0.75, 1.0]$.

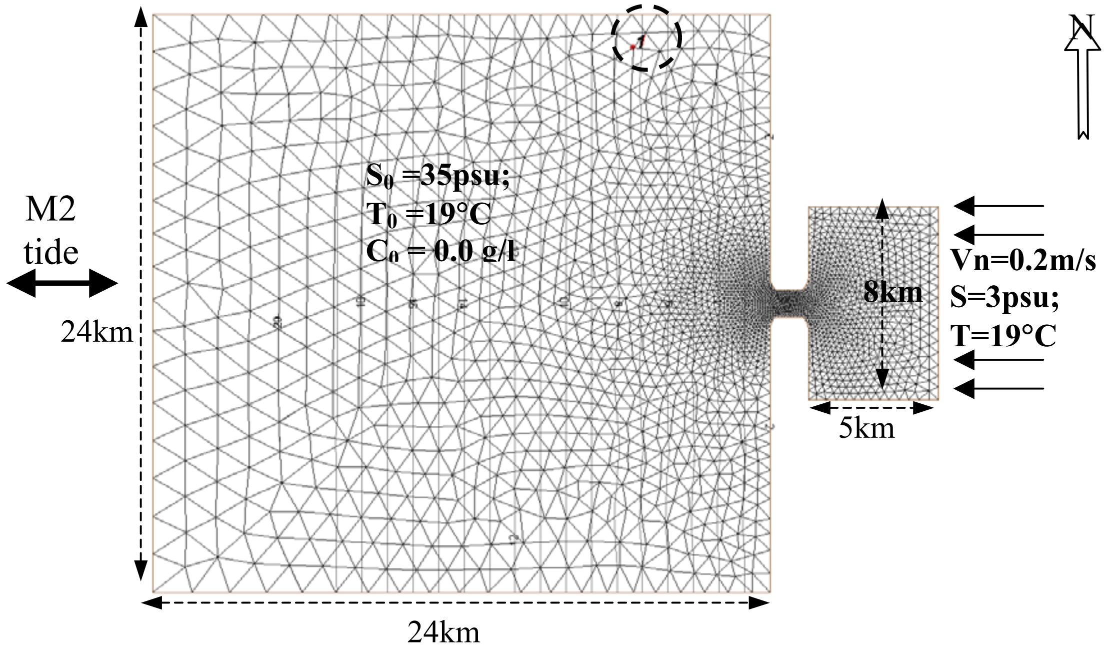

Fig. 5.6. Bathymetry and triangular grid of an Idealized Tidal Inlet. Point-1 (dash-circled) is the selected point to assess the longshore sediment flux.

The initial conditions of salinity, temperature and sediment concentration in the ocean side are set to $S_o = 35$ psu, $T_o = 19°$ C and $C_o = 0.0$ g/l , respectively; while in the bay the initial condition for those parameters are $S_o = 3$ psu, $T_o = 19°$ C and $C_o = 0.0$ g/l. Along the normal flow boundary, the normal flux of salinity, temperature and concentration are set as the essential scalar flux with $S_n = 3$psu, $T_n = 19°$ C and $C_n = 0.0$ g/l. The model performed a 10-day simulation with hydrodynamic time step $\Delta T = 4$sec and transport time step $\Delta T_{tr} = 12$ sec. One day hydrodynamic and three-day baroclinic ramp functions are applied to initiate the simulation. The implementation of the baroclinic ramp function is intended to smooth the initially sharp salinity gradient between fresh and saline waters. Thus, in this case the fully baroclinic term is achieved after a 3-day simulation. The salinity gradient between the surface and the bottom layers will generate a density pressure gradient, and balanced by the Coriolis force, will develop a geostrophic current northward assuming the northern hemisphere.

After a 10-day simulation, the salinity front is well developed. Figs. 5.7 a,b show a comparison of salinity distribution between the near surface ($\sigma = 0.75$) and the near bottom ($\sigma = -0.75$) layers. Near surface salinity spreads much further offshore, developing a tongue of low salinity propagating northward, with its center of low salinity about 8km offshore. The distribution of salinity further offshore is accelerated by two factors: (1) momentum flux from the normal flow on the right boundary, and (2) offshore acceleration of the baroclinic term in the upper layers due to the presence of the salinity (i.e. density) gradient.

The near bottom layer salinity clearly exhibits a different pattern of salinity distribution. Due to the balance between upstream baroclinic forcing and outward flow in the lower layers, the salinity front in the near bottom layer does not propagate far offshore, but just in the outer tip of the inlet. The front oscillates back and forth along the inlet in accordance with the tidal period. However, there is a northward propagation of brackish water with salinity value from 19 psu to 33 psu, caused by the presence of the northward-developed geostrophic transport along the shore. It is imminent that the distribution of near bottom salinity becomes asymmetic from the inlet to the offshore.

In the near surface layer, about 2 km offshore of the inlet, there is a small circular area with salinity higher than its surrounding area. This area represents the convergence/divergence zone between fresh water fluxes and oscillating saline water where vertical mixing is intensively occurring in this area in coherence with tidal oscillation. The high salinity in the indicated area is caused by the supply of the saline water from the lower layer by an upwelling process. However, further assessment is necessary as to whether this area is observable in any real bodies of water.

Interpolation from an unstructured (Fig.5.6) to a structured rectangular grid was also performed to generate a new matrix for the three-dimensional view. The result for the three-dimensional view of salinity distribution is shown in Fig.5.7c, taken at t = 10-day. The figure shows the salinity stratification with intrusion of saline water, S > 33psu (red), in the onshore direction. The upstream intrusion of saline water along the river is not shown here, due to the overlay of other salinity layers above it. Considerably fresh water

(a) Near Surface Salinity

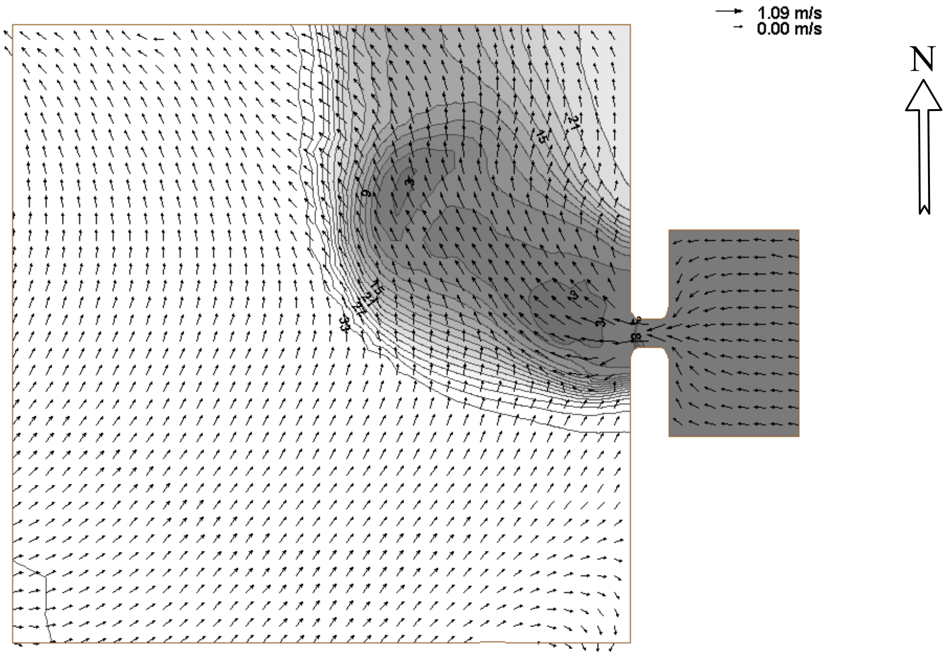

(b) Near Bottom Salinity

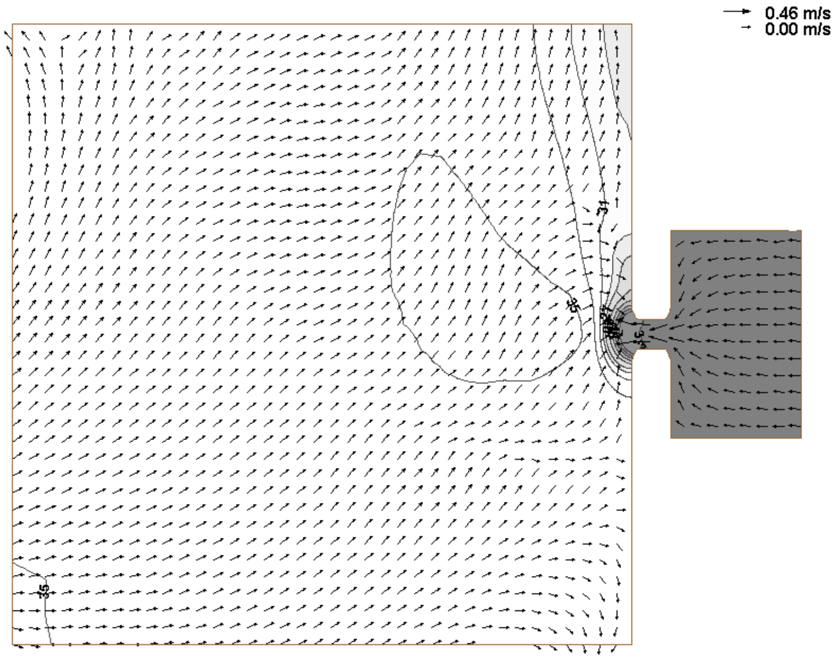

Fig. 5.7. Salinity distribution for Tidal Inlet case taken at t = 10-day. (a) Near Surface salinity, and (b) Near bottom salinity. Contour lines indicate salinity values, and the scaled arrows represent the direction and magnitude of the flow.

(c) Three dimensional view of Salinity

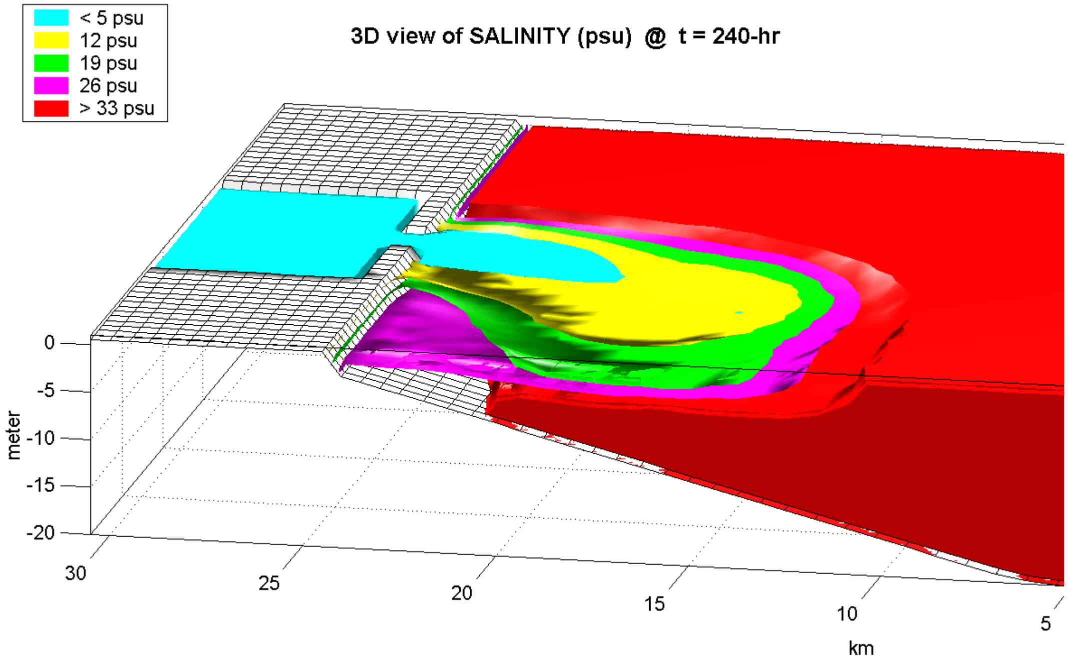

Fig. 5.7. (Cont'd) (c) Three-dimensional view of salinity at t = 10-day.

with S < 5psu (cyan) is discharged from the river flows to the ocean. At t = 10-day, fresh water may be observed up to about 5 km offshore, and then deflected to the north (right) by the geostrophic force.

The corresponding sediment transport nearly follows the pattern of the salinity transport, except that the sediment settles as it is transported, and it is deposited when the bottom shear stress is less than its critical shear for deposition, τ_{crd} (Fig. 5.8a,b). The channeling effect of the normal inflow from the east-end boundary into the bay and then through the inlet will significantly increase the current velocity along the inlet. Consequently, the bottom shear stress increases and the erosion occurring in the inlet causes suspended sediment. The suspended sediment is then transported offshore and deflected northward due to the effect of developed the geostrophic transport discussed previously.

(a) Near Surface of suspended sediment concentration

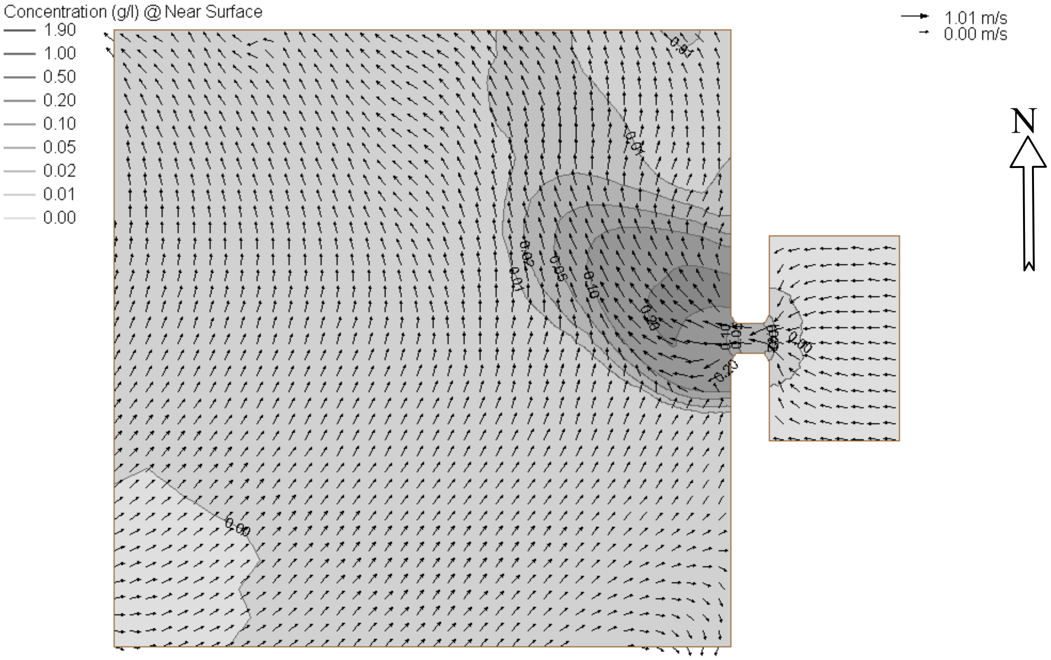

(b) Near Bottom of suspended sediment concentration

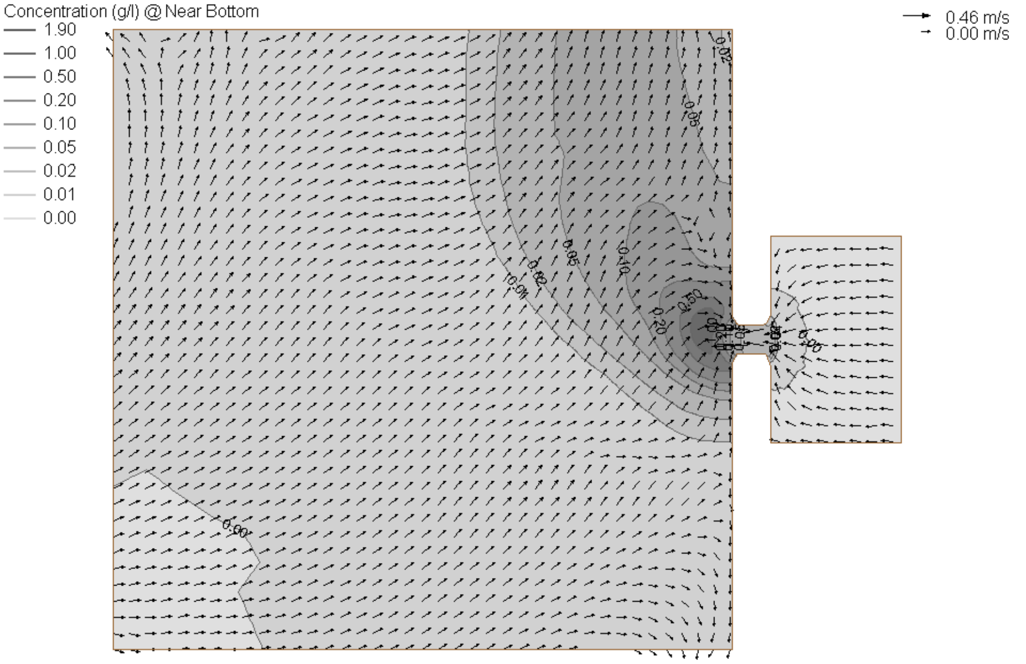

Fig. 5.8. Distribution of suspended sediment concentration taken at t = 10-day simulation. (a) Near surface concentration of suspended sediment, and (b) Near bottom concentration of suspended cohesive sediment. Contour lines indicate concentration in g/l, and the scaled arrows represent the direction and magnitude of the flow.

(c) Three-dimensional view taken from Az = -20° N

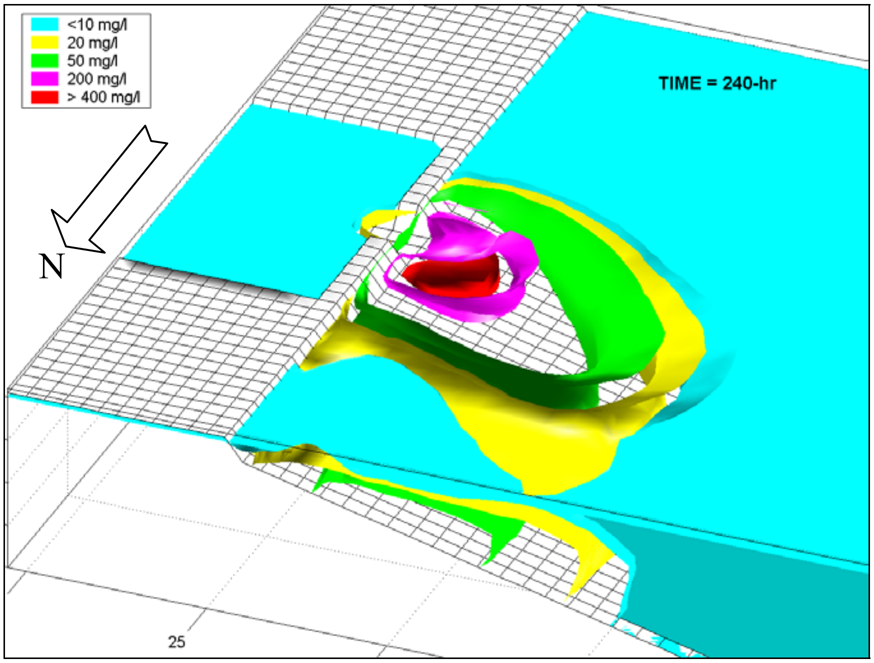

(d) Three-dimensional view taken from Az = 117° N

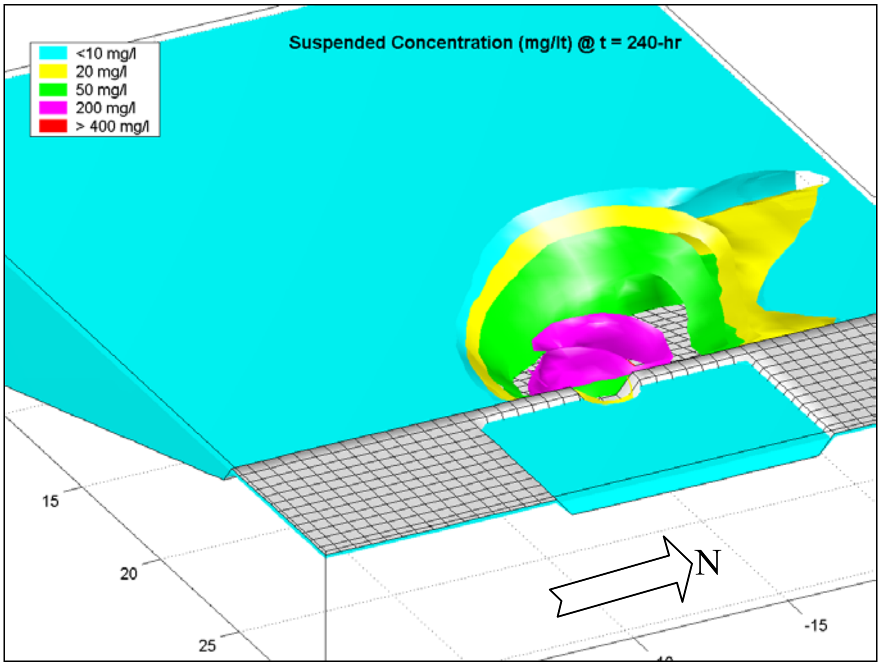

Fig. 5.8 (Cont'd) (c) Three-dimensional view from azimuth -20°N, and (d) Three-dimensional view from azimuth 117°N. Color legends indicate the concentration of suspended sediment in mg/l, and the rectangular grids represent the surface of bathymetry.

The maximum suspended concentration in the near surface layer is 0.5 g/l in the inlet and decreases to 0.025 g/l at about 8 km offshore. Similar to the salinity, the distribution of the near surface sediments also experience right-deflected propagation due to the prevailing Coriolis force acting on the water mass in northern hemisphere.

The maximum concentration near the bottom layer is higher than the layers above, since settlement of suspended sediment drives the concentration to accumulate in the bottom layers. Sediments from the inlet are transported downstream, and because of settlement, they reach the lower layer and are transported back upstream by the residual flow in the lower layer to the convergence ‘null point’. The highest near bottom sediment concentration is 1.94 g/l found near the mouth of the inlet in the offshore direction. This site is close to the place where the null point occurs. However, the prevailing northward longshore current transports some residual sediment to the north.

Similar to the process applicable to salinity, the three-dimensional concentration in a structured grid is interpolated from an original unstructured grid output file. The results of interpolated-suspended sediment concentration are given in Fig.5.8c,d both taken at t = 10-day. The plots were taken from two different azimuths: -20°N (Fig. 5.8c) and 117°N (Fig. 5.8d). It is clearly shown that the high concentrations are mostly suspended around the mouth inlet, seaward, not far from the origin of erosion. As the sediment cloud deflected and propagated northward, the concentration became less and less. Higher concentration is contained in the lower layer.

It is expected that for longer simulation times, the longshore transport would move this cloud of sediments much further northward; but this is beyond the scope of discussion in this research. For cohesive sediment, a decreasing suspended sediment concentration will reduce the settling velocity (Eq. 4.16), thus the sediment will likely remain suspended in the water column much longer.

To investigate the prevailing northward flow, one point, marked as ‘Point 1’ (dash-circled in Fig. 5.6) is selected near the north radial boundary. The depth averaged of east-west (U) and north-south (V) flow directions are shown in Fig. 5.9a and 5.9b, respectively. Detided time series provides nearly zero eastward flow and 0.07 m/s north-

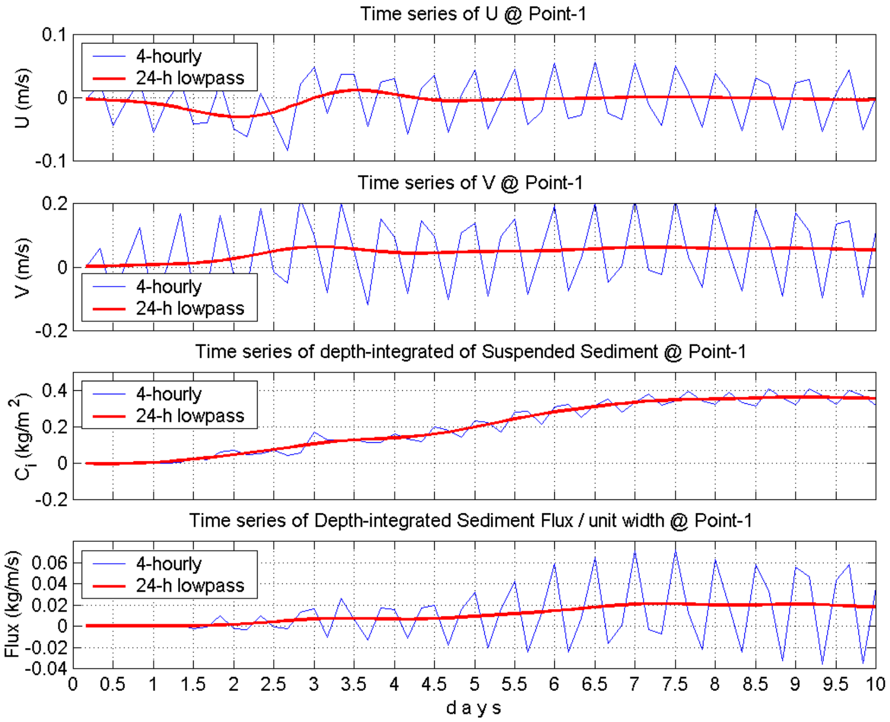

Fig. 5.9**.** Time series of depth-averaged velocity U and V, depth-integrated suspended concentration, C_i , and depth-integrated Sediment Flux at point #1 indicated in Fig. 5.6. The thin lines represent the observational values obtained from the model, and bold lines are detided values (24-h low passed) of each constituent.

ward flow after a 10-day simulation. The nearly zero flow in the east-west direction may indicate that there is only a small cross-shore transport as the material travels northward. On the other hand, the presence of a net northward flow may lead to a significant longshore transport of suspended sediment. The depth-averaged northward flow increases as the salinity difference between a near shore and an offshore location becomes more prominent. Such a difference causes the baroclinic acceleration to be enhanced.

The corresponding time series of the depth-integrated concentration in units of kg/m^2 is given in Fig. 5.9c, where the concentration at point 1 tends to increase as the supply of suspended sediments from the inlet are transported alongshore from the south. The concentration here is the residual sediment transport that has not yet deposited and remains as a suspended sediment. The net of depth-integrated sediment flux shown in Fig. 5.9d is computed by multiplying the depth-integrated concentration by its prevailing northward flow. The unit of the sediment flux is kg/s/m$_{\text{width}}$. In this case study, it is demonstrated that due to existing erosion around the inlet, a net longshore sediment transport of 0.018 kg/m$_{\text{width}}$/s may occur.

The maximum seaward velocity passing through the inlet occurs near the ocean side of both the left and the right edges of the inlet (Fig. 5.10). The maximum erosion at those sites is more than 0.08 m for the period of 10 days. The erosion is fairly uniform in the middle of the inlet of about 0.06 m, decreasing towards the east and west sides of the inlet.

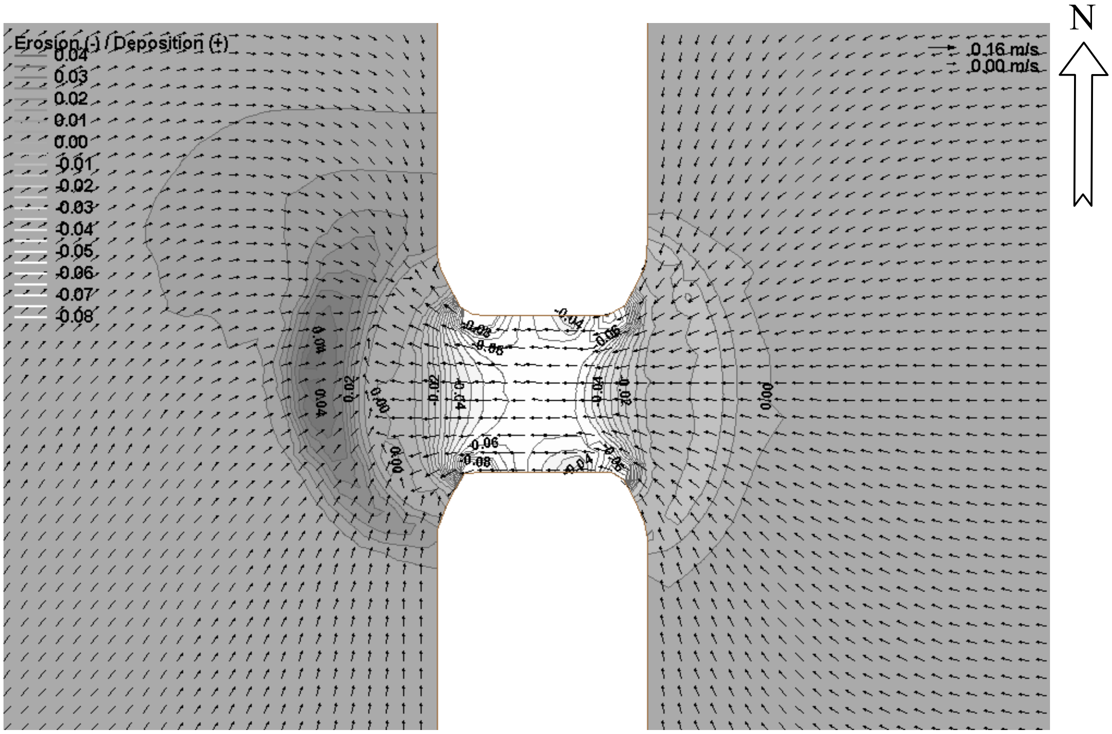

Fig. 5.10. The occurring erosion (-) and deposition (+) around the inlet after 10-day simulation.

The deposition pattern is asymmetrical between the ocean and the bay sides, with more significant deposition occurring at the ocean side. The main deposition of suspended sediment is concentrated just offshore of the inlet mouth. It is indicated by a dark shade in Fig. 5.10, with its maximum deposition of about 0.04 m accumulated for a 10-day simulation, or about 1.4 m/year. This area represents the null-point zone between the out flow jets from the inlet and inward saline wedge due to the presence of the baroclinic flow. The saline wedge does not penetrate the inlet due to a strong inlet outflow. Thus, the existing null point may cause the near bottom sediment to settle and be deposited at the bottom. Meanwhile, the upper layer concentration is transported further, deflected to the right, and carried away by the prevailing northward longshore flow discussed previously.

5.3. Capping Erosion

The case of idealized dredging-cap might be useful in determining the design cap thickness and also in consideration of the appropriate grain size of cap sediments to help minimize the erosion due to wave and current. The basic requirement for capping is to isolate the contaminated sediment of dredging disposal. Dredging material caps are typically constructed with a considerably thick layer of sand or clean dredged materials. However, in such an episodic event of a storm and an extreme current condition, cap erosion may occur. The idealized capping model considered here demonstrates the occurrence of capping erosion under the extreme current condition, where the combined wave and current effect may drive the suspended sediment in a certain way and where the exposed fine-grained material may be transported.

Assuming that each grain size in a non-cohesive sediment type behaves and is transported independently, with no interaction between them, the model allows a multi grain size setup (maximum 3) in one simulation. The distribution of grain size can be specified by percentage grain size of the sediment content. The suspended distribution, erosion and deposition of each grain size are sequentially processed; however, the depth change integrates all erosion and deposition terms occurring for each grain size.

An example of the transport of an idealized dredged mound, neglecting density pressure gradients (i.e. the barotropic mode) is given in the Fig. 5.11a. A three-dimensional view of the domain is shown in Fig. 5.11b. The cap domain dimension is 14km by 8km,

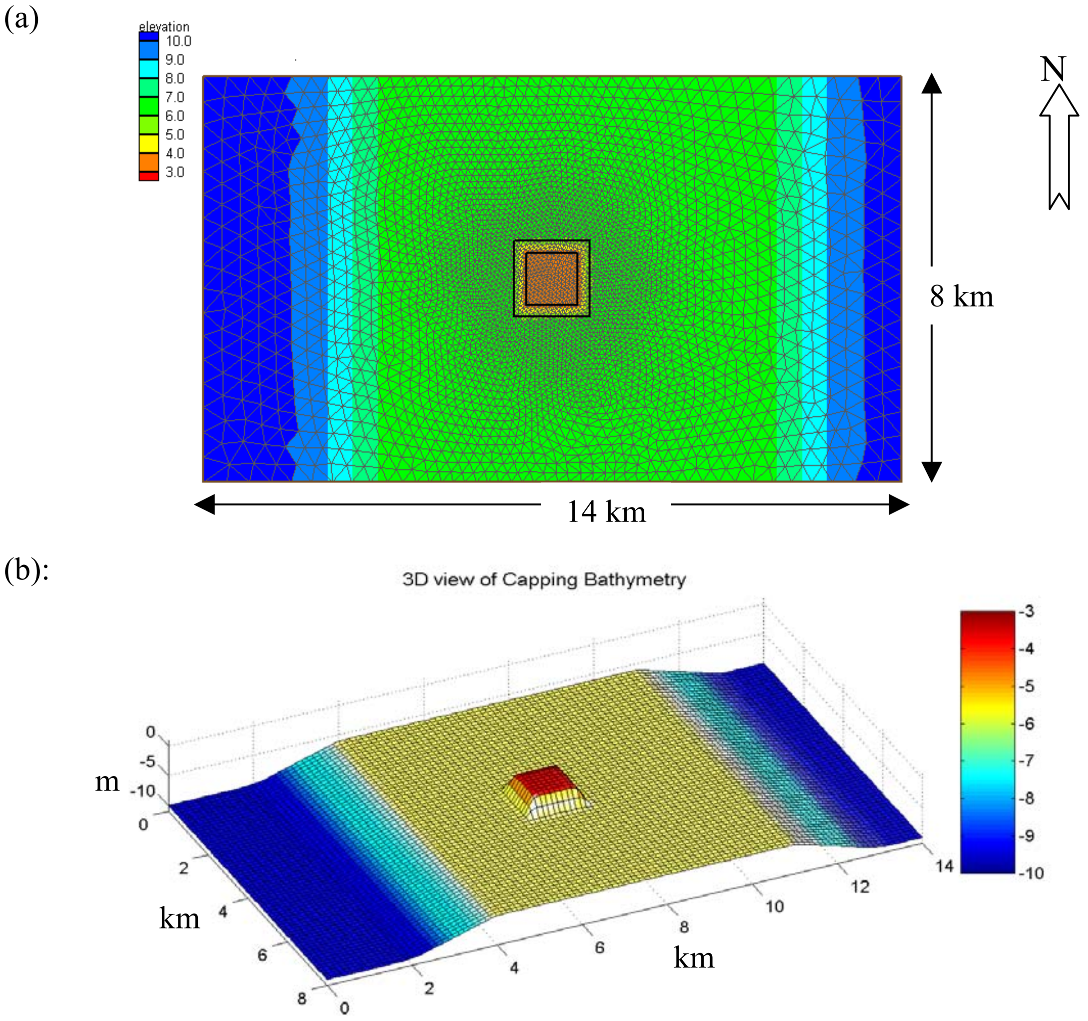

Fig. 5.11. The idealized capping mound domain. (a) Bathymetry and grid. Outer and inner box marks represents the bottom and upper edges of the capping, respectively, and (b) 3D view of bathymetry from azimuth 210°N. Horizontal scales indicate the distance in km. Vertical scale and color bar indicate the depth in m.

with uniform depth of 6 m in the mid domain between 4km and 10km, sloping down to 10m in both east and west boundaries. The domain is assumed to have a uniform grain size of d_{50} = 0.1mm. A rectangular area in the middle of the domain represents a rectangular one square kilometer mound with 3m mound-height of mixed sand material consisting of mean sand grain sizes (d_{50}) 0.1mm (10%), 0.2mm (50%) and 0.3mm (40%).

See Fig. 5.12. The placement of the idealized mound cap in the 6m water depths is intended to demonstrate the probability of occurring erosion and deposition.

The triangular grid sizes were specified to be 50m around the mound cap, gradually increasing toward the boundaries reaching size of 500 m. The final grid contains 3589 nodes with 7052 triangular elements. The boundaries along the south and north boundaries are no-flow boundaries with allowing tangential slip. The east boundary is a normal flow boundary and an open boundary with 0.5 m amplitude of M2 tidal forcing along the west end boundary. The Coriolis force is neglected.

The current of 0.5 m/s at the maximum intensity of an event flows from the east boundary as the normal flow boundary condition. A wave with period T = 6 sec travels at an angle of ϕ=45° to the direction of the current, and the distribution of wave height in the domain given in Fig. 5.13 varies from 0.1m at both east and west boundaries to 1.0m around the cap. The wave agitates the bed material suspended in the water column and the current moves the material considerably. The effect of density will create a different flow pattern. With a density change, the concentration will drive the flow faster near the

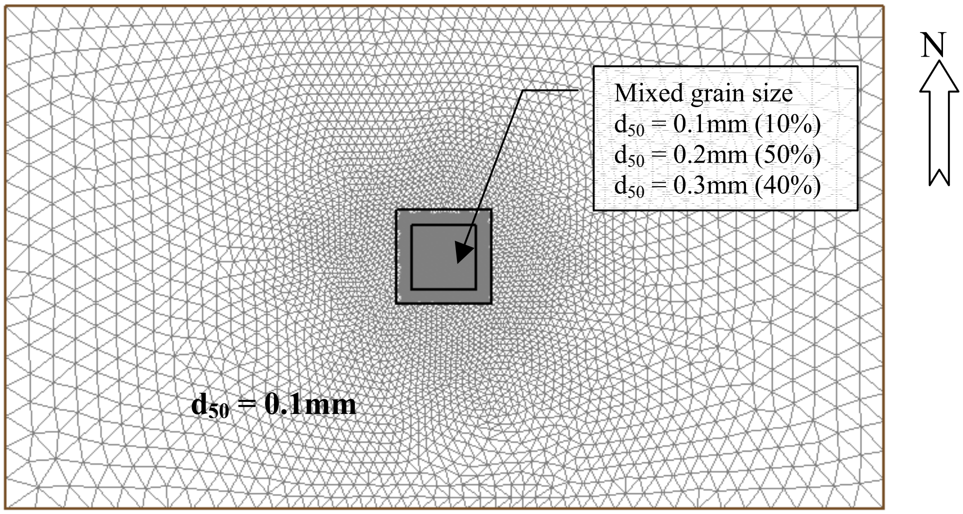

Fig. 5.12. Grain size distribution for the idealized capping case. The sediment grain size #1 (d_{50} = 0.1mm, 10%), grain size #2 (d_{50}= 0.2mm, 50%), and grain size #3 (d_{50} = 0.3mm, 40%) are located specifically in the capping site.

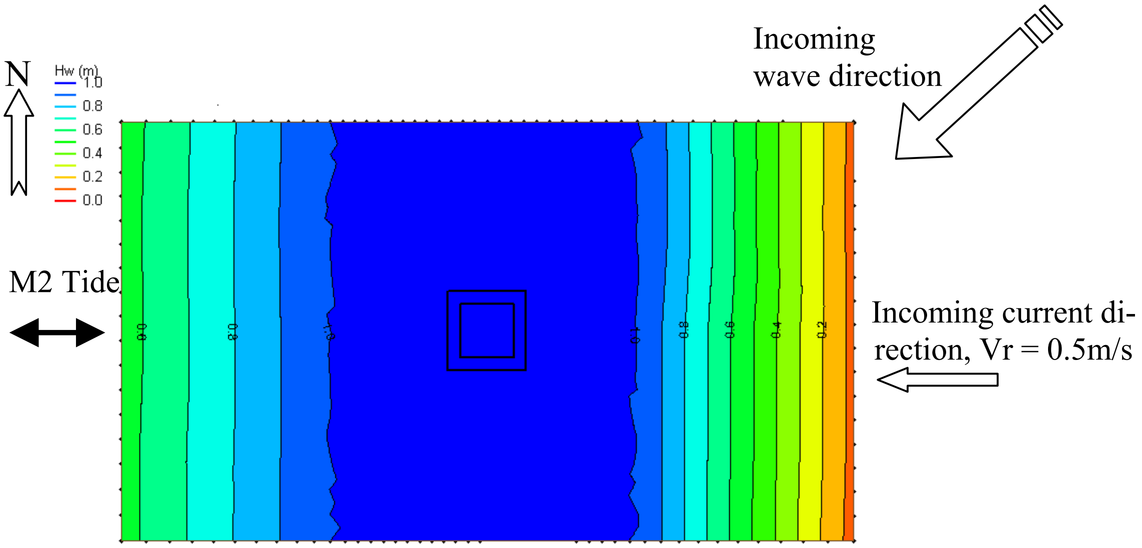

Figure 5.13. Simulated current and wave field applied to the idealized capping simulation.

bottom. However, this case considers barotropic mode only, and the Coriolis force is neglected to assess the symmetry of the results.

Since a wave field is immediately applied when the model runs, the processes of erosion, suspension and deposition occur accordingly. The applied wave height of 1.0 m around the cap where its depth is only 3 m causes a significant amplitude of wave orbital velocity at the bottom up to 0.8m/s, and consequently increases the wave-induced bottom shear stress τ_w. Combined with the existing current-induced bed shear stress formulated in Chapter IV, this may lead to the suspension of the sediment immediately after $\tau_{b\text{-}max}$ exceeds the critical shear stress for erosion τ_{cre}.

A maximum near bottom velocity at the eastern edge of the top cap initiates the erosion around capping, which is carried away by the current and deposited gradually as the current velocity decreases westward. After a 4-day simulation, significant amount of erosion and deposition occurs around the cap (Fig. 5.14a,b,c). The eastern edge and around its slope is severely eroded, while the deposition takes place on the west slope of the cap. This process behaves like a mound of the mound cap that shifts westward, similar to the profile given in Palermo et al. (1998).

(a) $d_{50} = 0.1$mm

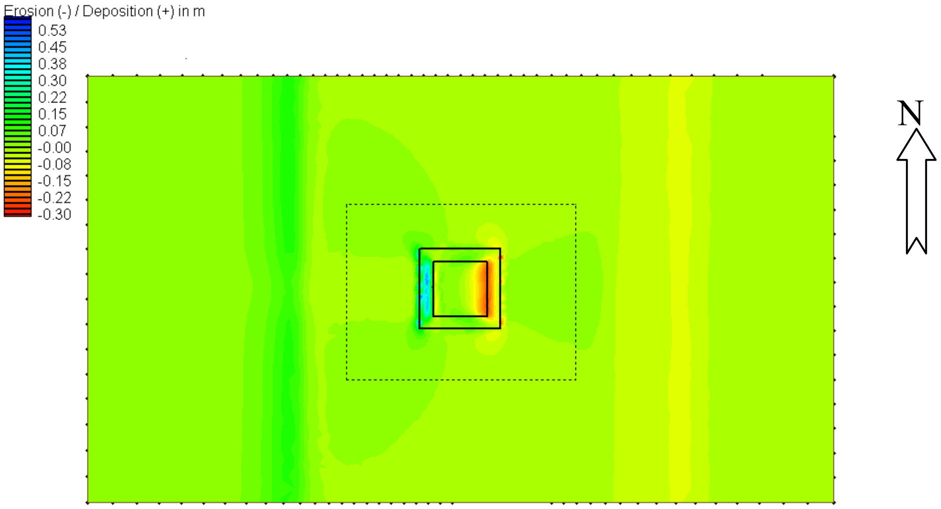

(b) $d_{50} = 0.2$mm

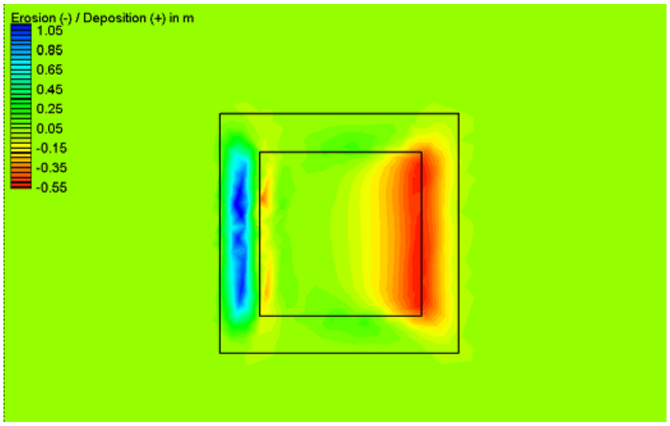

(c) $d_{50} = 0.3$mm

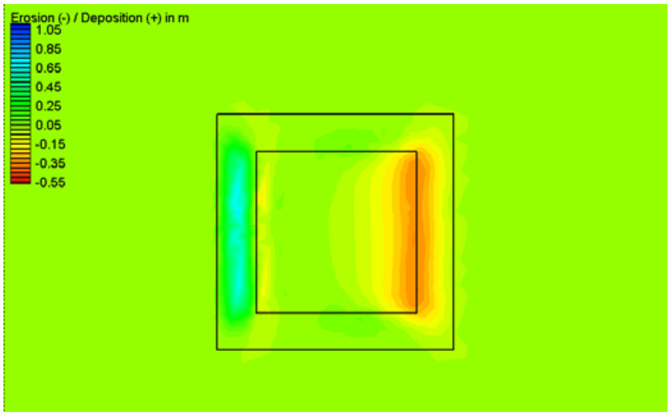

Fig. 5.14. Occuring erosion (-) and deposition (+) for the three-grain sizes. (a) 0.1mm for the whole domain, (b) 0.2mm around the capping, and (c) 0.3mm around the capping; snap shot after t = 100-hour simulation. Dashed box in part (a) represent the zooming area of part (b) and (c).

The smallest grain size with d_{50} = 0.1mm reveals the largest and widest erosion due to lightest weight among the three grain sizes (Fig. 5.14a). The relatively small settling velocity of this grain size, which is about 0.005 m/s, allows the suspended sediment to travel much further. At t = 100-h, the maximum erosion up to 0.3m for the grain size 0.1mm occurs in the east slope of the cap facing the incoming current, and the 0.5m material deposition starts from its west slope and decreases westward. Three nearly round sites indicated in the figure, which are located at east, northwest and southwest of the cap represent the depositional area. The east site is the deposition area due to relatively smaller current than its surrounding area (See Fig. 5.15) that allows the suspended sediment to settle. The north- and south-west sites are the area where the suspended sediment gradually deposits as the maximum current velocity gradually decreases away from the cap site. The magnitude of deposition in these sites at t = 100-h are 0.03m near the cap decreasing to 0.001m outward from the cap.

Due to the availability limit of 0.2mm and 0.3mm grain sizes around the cap only, after t = 100-h, the occurring erosion for those grain sizes mostly exist on the east slope with maximum erosion 0.55m and 0.35m for grains size 0.2mm and 0.3 mm, respectively. A heavier weight of grain size cause limited distance travel. The deposition for both grain sizes takes place just around the west slope (Fig. 5.14b,c) with maximum deposition 1.05m and 0.70m for grains size 0.2mm and 0.3 mm, respectively.

The occurring erosion and deposition cause the shifting point where the maximum velocity occurs. Initially at t=32-h, the maximum current velocity, represented as depth-averaged velocity during the maximum ebb tide current, occurs just right at the east end tip of the top cap (Fig. 5.15a). After t = 94-h, the location of maximum current is shifted westward. Erosion in the east tip of capping may reduce the maximum current, and at the deposition site, the current velocity tends to increase (Fig. 5.15b).

Fig. 5.16 shows the depth change of bathymetry between initial time t=1-h and t=100-h simulation. The change of depth is computed from accumulated erosion and deposition occurring for each specified grain size. The figure clearly shows the westward shifting of the mound cap within 3 days, while the previously capped material in the eastern cap slope is considerably exposed, and the material is suspended, transported westward, and then deposit.

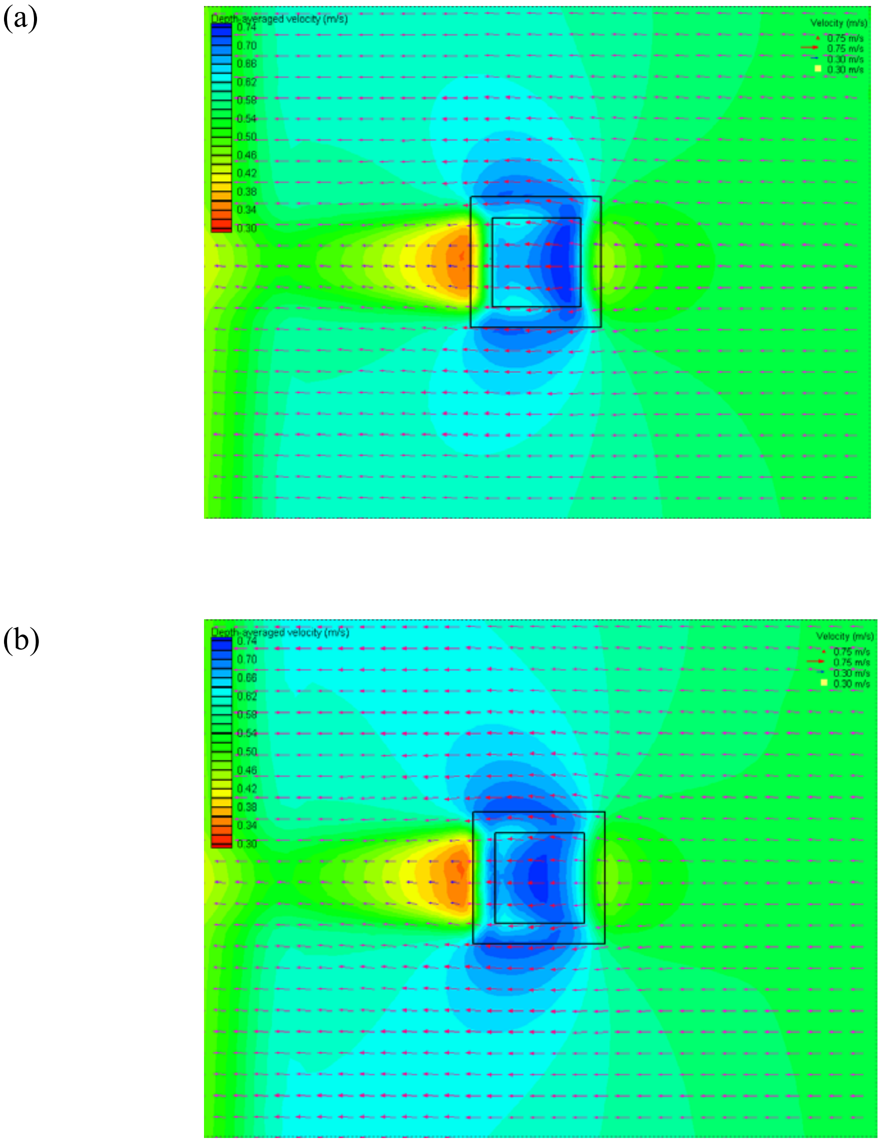

Fig. 5.15. Contour map of magnitude of depth-averaged velocity during the maximum ebb tide for (a) t = 32-hour to (b) t = 94-hour. Arrows represent the relative magnitude and direction of the current.

(a) Bathymetry @ t = 2-hour

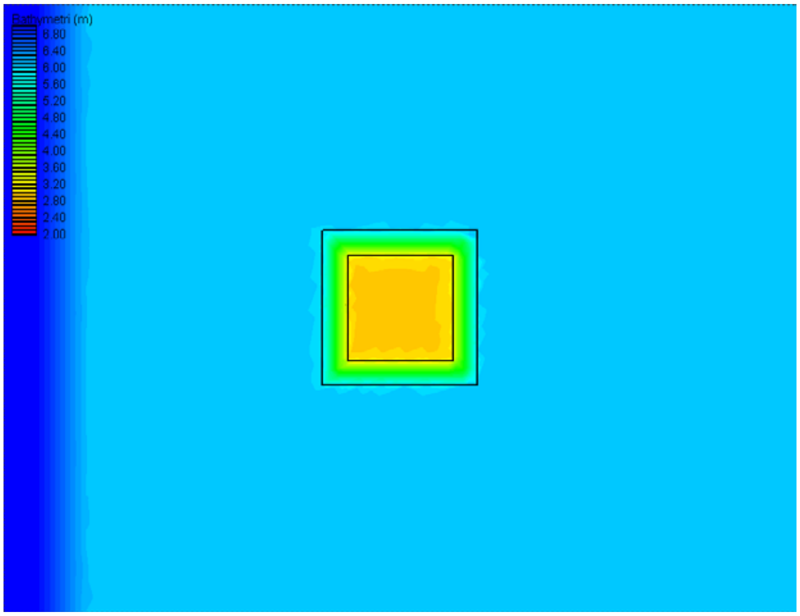

(b) Bathymetry @ t = 100-hour

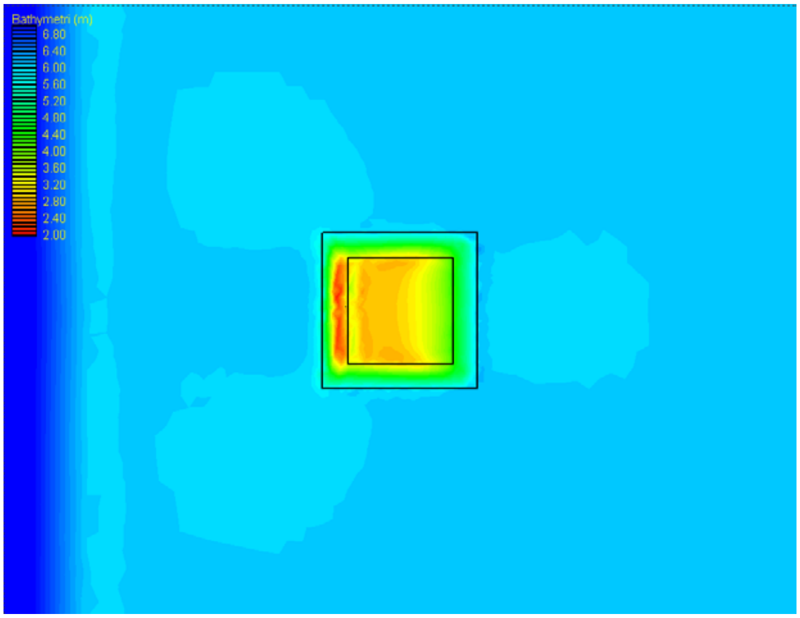

Fig 5.16. Change of bathymetry around cap. (a) Initial condition at t = 2-hour, and (b) at t= 100-hour.

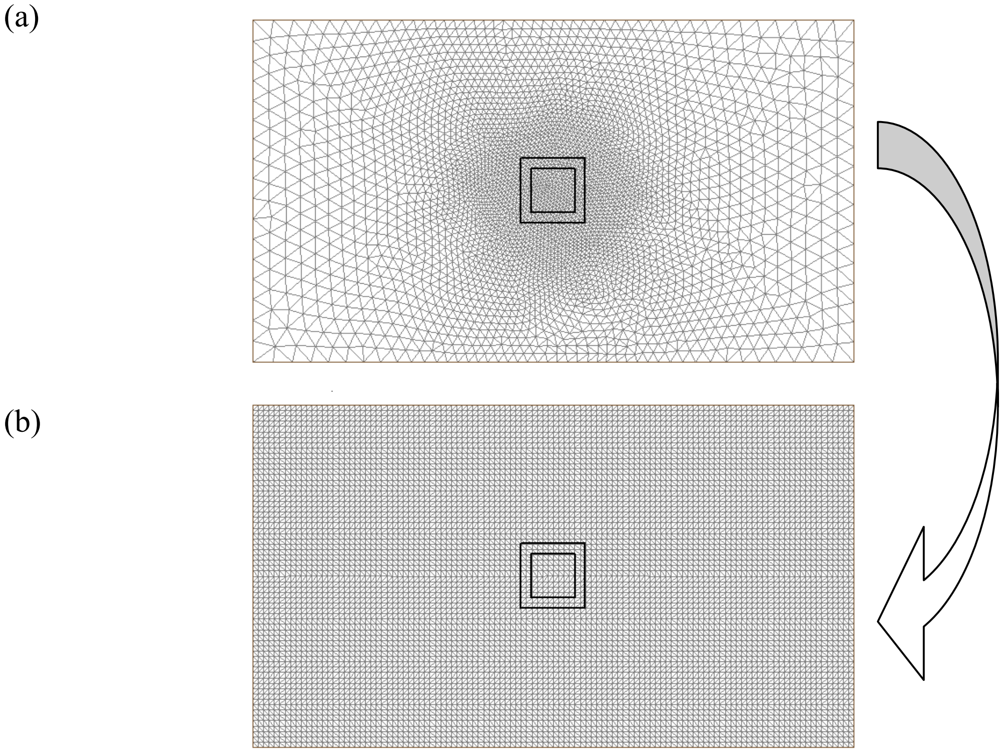

Fig. 5.17. Grid conversion from (a) unstructured to (b) structured grid.

The limitation of the unstructured finite element grid is the difficulty in generating the 3D-view in SMS software. Similarly for the concentration and salinity 3D-plots, the weighted inverse-distance interpolation method is the selected way to transform the bathymetric change output file from the unstructured to the structured grid. As shown in Fig. 5.17, the unstructured capping grid is interpolated to the new 14 by 8 km^2 structured grid, with 113 nodes in east-west direction and 65 nodes in north-south direction, making a total of 7345 nodes. The new grid has 125m-spacing element size. Each node in the new grid will identify the element number of the old grid, and then identify the surrounding three node numbers in that element. Then the inverse-distance weighted interpolation can be computed for the depth value when three distances (or triangular areas) have been computed. Comparison between original and interpolated bathymetric depth values is in agreement (See Appendix B).

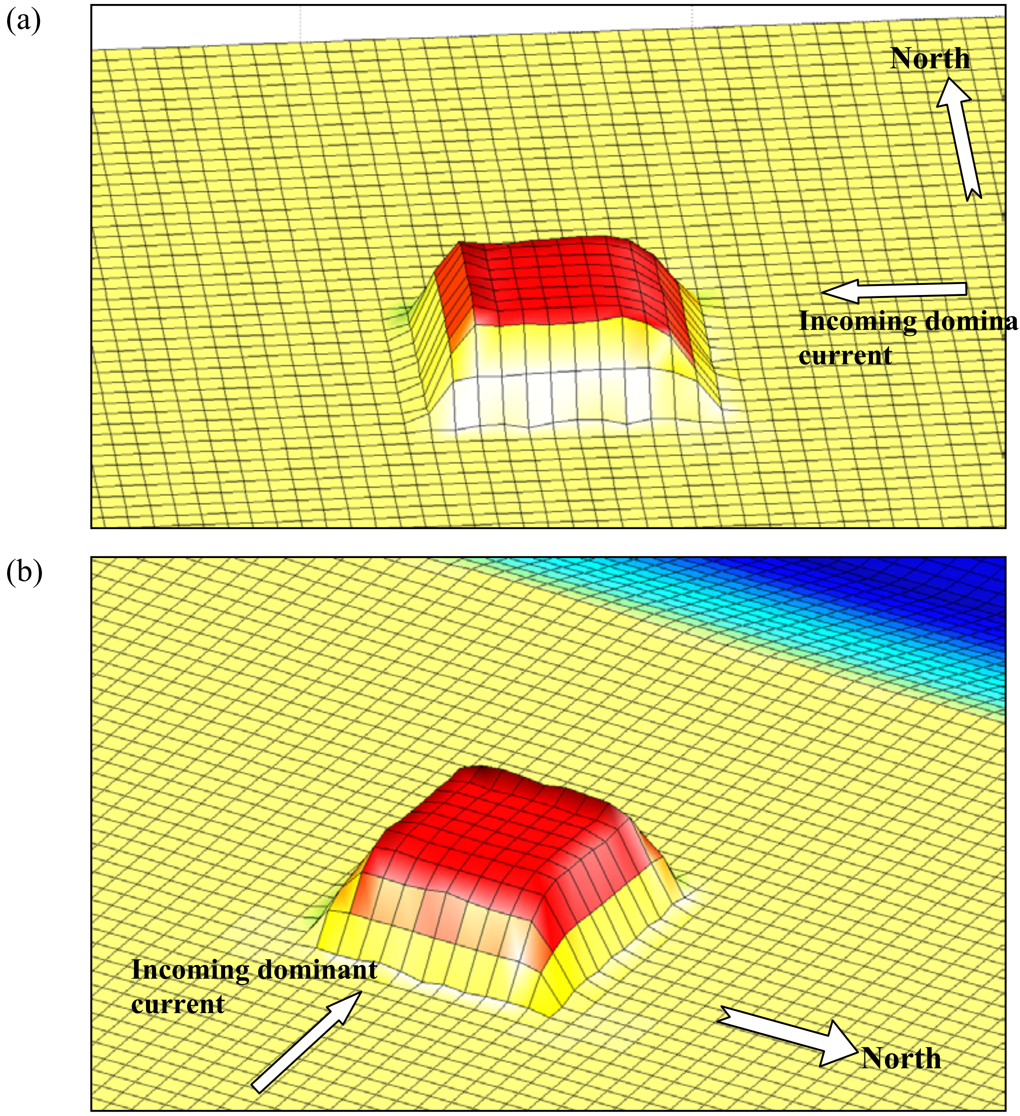

Fig. 5.18. Three-dimensional view of bathymetry around the capping taken at t = 100-hour from two different azimuths: (a) 185°N, and (b) 60°N.

Three-dimensional views of the mound cap between initial time t=1-hour and after t=100-hour are presented in Fig. 5.18a,b, viewed from the southwest site. Comparing the two plots, it is clear that the mound cap shifts westward. There is a possibility of exposing the capped material. Thus, with the developed transport model in this research, one can expect a tool to design cap thickness and a consideration of the appropriate grain size of cap sediments to minimize the erosion due to wave and current.

CHAPTER VI

ANALYSES AND DISCUSSION

A numerical model for simulation of hydrodynamic circulation and sediment transport is described in this study. The model includes baroclinic forces to incorporate density changes found near the coast. The model has been applied to several test cases to demonstrate its applicability to practical problems and to demonstrate its robustness.

6.1. Hydrodynamic Module

An assessment in the ADCIRC 3D-VS model has been performed to include the vertical velocity solution in σ-coordinate system. Comparison to the analytical solutions and numerical results of other researchers in most cases are in good agreement. The solution of hydrodynamic components η, u, v and w is the main source to estimate the sediment and soluble material transport.

The accuracy of the vertical velocity solution is critically dependent on the accuracy of the horizontal velocity solution. At some points from the QATP case, mainly in the region near the lateral boundary at θ=0 and θ=π/2, the presence of tangential velocity may lead to over determined vertical velocity solution. The order of the tangential velocity in this region is nearly in the same order as the vertical velocity.

In another numerical model experiment given in Pandoe and Edge (2003), the ATP case removes the presence of those lateral boundaries. For the case with the selected points located at r=70km, the model demonstrates a significantly reduced tangential velocity down to the order of 10^{-7}m/s. More uniform vertical flows along the circular section have been achieved. However, the cause of the tangential flow near the boundary has not been well studied yet.

Luettich et al. (2002) suggested that to improve the computed vertical velocity is to reduce the errors in the depth-integrated mass conservation. Recent studies by Hagen (2001) and Hagen et al. (2001) indicate that the element configuration and shapes contributes to the truncation error that may lead to the error in the conservation of mass. Therefore, better accuracy and stability of the hydrodynamic solutions are usually achieved by refining the grid resolution, smoothing the bathymetry, reducing the time step, or adjusting the most appropriate τ_o value in GWCE formulation.

6.2. Salinity and Temperature Transport and Baroclinicity

The formulation of 3D transport couples a horizontal (2D) and vertical (1D) finite element method for spatial solution, and applies the two-time level explicit scheme of finite difference method for temporal solution. Thus, in every time step, the model will solve a two-dimensional tri-diagonal matrix for each node, progressing to the adjacent node. The formulation method works well. Some experiences indicate small errors propagating from node to node since the solution is solved sequentially. It is retained in the solution as the conservation mass error.

So far, in all study cases, the model considers only constant temperature. The effect of the temperature change is not studied here. Further assessment for the temperature change has not been fully studied yet, but it is implicitly retained in the saline wedge assessment.

The implementation of the baroclinic forcing terms has been successfully adapted into the momentum equations. The DBP test case shows the process of stratification between fresh and saline water. For comparison, the Rutgers University has developed the Regional Ocean Model System (ROMS) and the Spectral Element Ocean Model (SEOM). Both models performed a gravitational adjustment of density in a flat channel (Rutgers Ocean Modeling Group, 2004), which is exactly similar to the Dam Break Problem in this study discussed in Chapter III. In order to maintain stability and smoothness, their model applied large values of diffusivity from $40m^2/s$ to $100m^2/s$. In the model developed in this study, smaller horizontal diffusivity of $5m^2/s$ was applied to produce the stratification in the DBP with unconditionally stable model run. The technique applied here is that the baroclinic model applies a ramp function for two days on the baroclinic forcing terms to let the density (i.e. salinity) front expand, while the baroclinic forces act in the opposite direction between the upper and lower layers. Thus, at the early time step, the baroclinic terms is not fully forced into the momentum equations, but gradually increases as the time step increases.

Comparison of the arrested saline wedge from the numerical model to the empirical formulation also gives good agreement. The computational saline wedge using the Partheniades empirical formulation (Partheniades, 1990) is very sensitive to the change of both river flow and depth. Thus, very accurate assessment of the model results is required to demonstrate that penetration of the saline wedge agrees with empirical data. The method of finding the length of the arrested saline wedge is efficiently demonstrated here by finding the null point at a near bottom velocity profile.

6.3. Sediment Transport Module

The coupled hydrodynamic-transport model is a good tool that could explain the behavior of sediment transport in the coastal zone. The idealized cases used here can demonstrate and estimate where the higher sediment concentration might exist, or where the converging and diverging zones might exist, which are associated with the sediment concentration.

Comparison between the numerical and the analytical model gives a good correlation. Secondary comparison was made against the ADTRANS 2D-DI model. Exclusion of second order terms in the transport formulation 2D-Transport model causes the deepest part of the channel to move slowly. In the 3D solution where the second order terms are included, the deeper parts of the channel migrate slower than the shallower parts, which agree with the analyses given in Van de Kreeke (2002), Van Rijn (1986) and Walstra et al. (2002). Thus, the channel profile becomes steeper in the upstream direction and gentler in the downstream direction.

Vertical distribution of suspended sediment of non-cohesive type is highly related to the Rouse Number (b_r). High b_r leads higher near bottom concentration than the layers above that produce a high vertical gradient. To reach a vertical stability solution of concentration, more vertical layers or smaller time step is required. On the other hand, depending on the grain size and depth of the water, the more layers will provide closer distance between the vertical layers, and may affect a large vertical Courant Number. Thus, to reach vertical stability, the optimal number of vertical layers should be estimated considering the grain size, minimum depth of the water, and time step. For example in the barred rectangular basin, with minimum depth of 1 m around the bar, six to nine vertical layers and a 6-second internal time step were appropriate. Also a threshold of $b_r<4.0$ was implemented to avoid instability due to large Rouse number b_r that may cause a high vertical gradient of concentration.

Based on the model in the barred-rectangular basin case, it can be inferred that the three-dimensional sediment transport may explain the distribution of sediment considering the flow and transport pattern among the vertical layers may propagate non-uniformly. The upper layer could travel faster or slower relative to the bottom layer, due to both the typical vertical profile of velocity and the effect of the baroclinic pressure term. With neglecting the Coriolis force, it is clearly seen that the deposition between barotropic and baroclinic modes provides different pattern and zone of near bottom high concentration. In the barotropic mode, the deposition is uniformly distributed along the channel, while in the baroclinic mode higher concentration occurred at one particular converging zone.

The inclusion of the baroclinic term in the stratified estuary contributes to a wider distribution pattern of suspended sediment, mainly for cohesive type sediment. However, to reach the stability condition for a large horizontal salinity gradient (i.e. large density gradient) between fresh and saline water, the baroclinic ramp function is required to smoothly applying the baroclinic acceleration term; and the applied horizontal diffusion coefficient, D_h, in most cases of stratified water is mostly less than $10 m^2/s$.

In case of cohesive sediment, it has relatively much smaller settling velocity than a non-cohesive sediment. Thus, the selected number of layers can be higher, or a larger internal time step can be implemented. Even though there was a discrepancy between the numerical and analytical model, the transport model is able to describe a realistic sediment transport, both for cohesive and non-cohesive types with the influence of the baroclinic term. Near future development includes a benchmarking of the model against the laboratory and observational results.

The uncertainty for the cohesive sediment is determined by the exact value of critical bottom stress for erosion τ_{cre} and deposition τ_{crd}. From cited references, those parameters have a large value range, and usually are considered as site-specific constants. This leads to an uncertainty of determining the magnitude of suspended sediment concentration. Thus, site calibration is required to compare the model to the natural estuarine case. In this study, there is no attempt to quantitatively verify the model to the observational result due to difficulties obtaining the data.

The settling velocity for non-cohesive sediment, mainly fine sand and larger size, is considerably large. For example, the settling velocities are 0.005m/s, 0.017m/s and 0.030m/s for grain size 0.1mm, 0.2mm and 0.3mm, respectively. Considering those values, applying the formulation of vertical suspended sediment concentration in Eq. 4.6 will give a relatively large Rouse number, that may indicate significant vertical concentration gradient with high concentration mostly clustered at near bottom. To avoid instability in the model, depth-integrated transport rate formulation is the selected method for non-cohesive sediment transport of the fine sand grain size and larger. Applying a 3D conservation of mass similar to the cohesive sediment was performed with some problem of model instability due to the concentration gradient or large vertical Courant number. Fully 3D formulation for non-cohesive sediment transport can be improved only with smaller time step and dense vertical layers, which will pay off to the longer simulation time.

The conservation of mass is well established in the model with accuracy up to 2% and 6% errors of the conserved mass for cohesive and non-cohesive sediment, respectively. The simulations show that a flat bottom provides better conservation of mass than a sloping bottom. The effect of slope may lead a source of the error, and needs to be investigated further. However, the model is mostly applicable for an estuarine zone with gentle slopes. Therefore, the error discussed is considered to be acceptable to model the sediment transport in the near shore or estuarine zone.

The transport model is able to describe a realistic cohesive sediment transport with the influence of the baroclinic term. The study case for an idealized tidal inlet exhibits reasonable mechanism of erosion, suspended sediment and deposition. As expected, the location of the deposition occurs mostly around the null-point location. The pattern of deposition clearly shows the development of an ebb shoal. Longer run-time simulation might be required to investigate the ebb shoal development around the offshore side of the tidal inlet.

In the tidal inlet case with activating the Coriolis force, salinity difference between ocean water and freshwater discharge from the inlet clearly generates very strong density gradients that also generate the geostrophic flows. After removing the tidal effect, the model has been able to demonstrate the presence of the longshore sediment transport associated with the existing geostrophic flow. This may lead to a future application to study the fresh water and suspended sediment discharges, such as the Mississippi river outflow to the Gulf of Mexico, where a significant amount of suspended sediments are transported along shore towards the Texas coast. Future development includes a benchmarking of the model against the laboratory and observational results.

The early assessment for suspended sediment transport under influence of both wave and current environments is quite promising. In the case of idealized mound cap, so far the model implements time and site independent of wave period T and incoming wave angle θ. The wave height field is site dependent and time independent. Therefore, as the deposition and erosion occur after some time, the wave fields are supposedly to change. This process is not yet available in the model, but possibly in a next step development. Model coupling between the ADCIRC 3D - Transport and STWAVE model becomes the first task of the near future model extension.

The model developed in this study offers the coupled hydrodynamic-transport numerical model ability to the application of the sediment transport. Application to the long-term stability of a dredged material placement site is promising. The idealized mound capping case shows the possibility of such erosion, suspension and deposition of the mound cap under the strong current and relatively high wave conditions. For comparison of available transport model, Gailani et al. (2001) provides a study of long-term stability of a dredged cohesive material placement site under the influence of various storms. The study uses the USACE Long Term Fate (LTFATE) model to compute time series of erosion, transport and deposition, where LTFATE requires hydrograph input of time series of hydrodynamic components provided by ADCIRC. Thus, the hydrodynamic and transport models have not been coupled in their study.

6.4. Model Assessment

Computer run-time is the main problem with the ADCIRC 3D Transport model. The more vertical-layers used, the more time required to run the model. Comparing to the 2D, the model with 9-vertical layers may take 6 to 8 times longer, depending on the selected transport configuration. To speed up computing time, parallel processing is the ultimate candidate for the next generation of 3D ADCIRC-Transport. The parallel ADIRC for three dimensional hydrodynamic is already available, therefore its extension to include the baroclinic mode and sediment transport might be achieved.

As the model is extended, some options are allowed in the model setup. The detail of the model setup is given in Appendix A, and the summary of the model setup include:

- Option for barotropic or baroclinic mode, and applied ramp function for the baroclinic mode.
- The way to compute water density, either $\rho = f(S,T)$ or $\rho = f(S,T,C)$
- Initial condition for salinity, temperature and concentration
- Determine boundary condition type for normal flux of concentration or sediment.
- Determine sediment type either cohesive or non-cohesive. For non-cohesive sediment, the model allows user to use up to 3-grain sizes for from fine to medium grain size. User can also specify the availability of the grain size in the domain, such as given in Fig. 5.12 for example.
- Specify the site dependent wave height, and constant of both wave period and incoming angle.

6.5. Post Processing

Another problem with the 3D ADCIRC-Transport is the large size of the output files listed in Appendix A. All output files are written in ASCII format for future post processing, and are written in the unstructured grid format. SMS software does the job for 2D post processing or 3D post processing for each vertical layer.

Converting the data from an unstructured to a structured grid is required for global 3D post processing which is mostly done in MATLAB codes. Examples of the results of those data conversions are given in Fig. 3.5, 5.4 and 5.14 for salinity, cohesive and non-cohesive suspended sediment concentration, respectively. A 3D movie generation is also possible in the new structured grid.

CHAPTER VII

CONCLUSIONS AND RECOMMENDATIONS

A suspended sediment transport model with the inclusion of the baroclinic forcing term has been successfully developed in this study. Coupled with ADCIRC 3D Hydrodynamic model, the baroclinic sediment transport model has shown a good agreement to analytical solutions. The model has been tested with various configurations of idealized cases, and successfully simulates the stratification and longshore sediment transport. Based on the achieved results, some conclusions and recommendations can be drawn.

7.1. Conclusions

An extended version of the three-dimensional hydrodynamic model, ADCIRC 3D-VS, was utilized to simulate both horizontal and vertical flows in a quarter annular harbor QATP. Comparison of horizontal and vertical solutions to the analytical solution and results of other researchers are in good agreement. The solutions differ in the order of 10^{-4}m/s and 10^{-6}m/s for horizontal and vertical velocities, respectively. The vertical velocity solution is highly sensitive to the horizontal velocity solutions.

A new technique of solving the 3D hydrodynamic-transport model is applied successfully in this study. The formulation couples horizontal (2D) and vertical (1D) in finite element method, and solve temporal variations in a finite difference two-time level explicit scheme. An approach of solving the baroclinic terms also works well, where the model successfully performed the dam break test problem and shows good agreement against the empirical saline wedge solution. Difficulties of getting field data are the main problem in the current study; thus, comparison to analytical solutions has been considered to verify the model results.

Cohesive and non-cohesive sediment transports are coupled to the hydrodynamic module. Both sediment types are treated differently, and it is assumed no interaction between particle sizes. The non-cohesive sediment has considerably larger settling velocity as the grain size increases. Thus, the 2D depth-integrated sediment flux formulation is considered more appropriate to model the suspended non-cohesive sediment transport for fine sand size and larger ($d_{50} \geq 0.1$mm); whereas fully 3D formulation can be applied in the formulation of suspended cohesive sediment (mud) and very fine sand ($d_{50} < 0.1$mm) due to small settling velocity.

For non-cohesive sediment, there is a good agreement between the numerical and analytical model on solving erosion and deposition in a 'Gaussian shape' trench. Longer runs can simulate the downstream travel of the channel, while deeper (trench) parts move slower than the upper (flat) parts. No comparison to the analytical solution was made for cohesive sediment type. The wide range of τ_{cre} and τ_{crd} lead to wide variation of the magnitude of suspended sediment transport, but qualitatively the transport seemed reasonably acceptable. The conservation of mass analysis provides an estimate of accuracy for the mass balance error, which is about 2% and 6% for cohesive and non-cohesive sediment, respectively. Steeper bottom slopes may lead to larger error.

The inclusion of the baroclinic term in stratified water qualitatively shows the development of arrested saline wedge, and leads to the presence of high mud concentration around the null point. The model also provides a longshore transport as expected in the real estuary such as a river sediment discharge from the Mississippi River into the Gulf of Mexico.

Application of the model to a capped dredged material mound is quite promising for design and planning of capping works. The occurring erosion, suspension and deposition of sand due to combined current and wave conditions will assist consideration of capping placement location and its thickness. Coupling the transport to the wave model might be required to obtain the reliable wave height, period and incoming angle of the wave field.

Lastly, the extended 3D ADCIRC-Transport model is ready to be applied in the real estuary or harbor configuration.

7.2. Recommendations

The extended 3D ADCIRC-Transport model provided in this study is open to expansion. Continuing work on the model development should couple the model with a wave model such as STWAVE.

Long run time is one concern of running the simulation in 3D ADCIRC-Transport. Thus, parallelizing the code is considerably important to be done immediately to improve the run time. Further study to apply the model in the natural configuration needs some early work for calibration of the model to the observational or field data.

REFERENCES

Bijvelds, M.D., van Kester, J.A. Stelling, G.S., 1999. A comparison of two 3D shallow-water model sigma-coordinates and z-coordinates in the vertical direction. In: Spaulding, M.L., Butler, H.L. (Eds.), Proceedings 6th Intern. Conf. on Estuarine and Coastal Modeling, ASCE, pp.74-93.

Blain, C.A., 1999. Modeling three-dimensional, thermohaline-driven circulation in the Arabian Gulf. In: Spaulding, M.L., Butler, H.L. (Eds.), Proceedings 6th Intern. Conf. on Estuarine and Coastal Modeling, ASCE, pp.130-147.

Blumberg, A.F., Khan, L.A., St. John, J.P., 1999. Three-dimensional hydrodynamic model of New York Harbour region. Journal of Hydraulic Engineering, 125 (8), 799-816.

Blumberg, A.F., Mellor, G.L., 1987. A Description of a three-dimensional coastal ocean circulation model. In: Heaps, N.S. (Ed.), Three-Dimensional Coastal Ocean Models, American Geophysical Union, Washington, DC, pp. 1-16.

Blumberg, A.F., Galperin, B., O'Connor, D.J., 1992. Modeling vertical structure of open channel flows. Journal of Hydraulic Engineering, 118, 1119-1134.

Camenen, B., Larroude, P., 2003. Comparison of sediment transport formulae for the coastal environment. Coastal Engineering, 48, 111-132.

Cheng, N.S., 1997. Simplified settling velocity formula for sediment particle. Journal of Hydraulic Engineering, 123(2), 149-152.

Fofonoff, N.P., 1985. Physical properties of sea water, a new salinity scale and Equation of State for Seawater. J. Geophys. Res., 90(C2), 3332-3342.

Fredsoe, J., Deigaard, R., 1992. Mechanics of Coastal Sediment Transport, Advanced Series in Ocean Engineering, Vol, 3, World Scientific, Singapore.

Gailani, J.Z., Sturm T.W., Wood, D.G., 2001. Prediction of long term stability of a dredged material placement site in Rhode Island Sound. In: Randall, R.E. (Ed.), Proceedings 21st Technical Conference of Western Dredging Association and 33rd Annual Texas A&M Dredging Seminar, Civil Engineering Department, Texas A&M University, College Station, TX, pp. 71-83.

Grenier, R.R. Jr., Luettich, R.A., Westerink, J.J., 1995. A Comparison of the nonlinear frictional characteristics of two-dimensional and three-dimensional models of a shallow tidal embayment. J. Geophys. Res., 100(C7), 13,719-13,735.

Gross, E.S., Koseff, J.R., Monismith, S.G., 1999. Three-dimensional salinity simulations of South San Fransisco Bay. Journal of Hydraulic Engineering, 125(11), 1199 – 1209.

Hagen, S.C., 2001. Estimation of the truncation error for the linearized, shallow water momentum equations. Engineering with Computers, 17, 354-362.

Hagen, S.C., Westerink, J.J., Kolar, R.L., Horstmann, O., 2001. Two-dimensional, unstructured mesh generation for tidal models. Intern. J. Num. Meth. Fluids, 35, 669-686.

Hayes, S.P., Chang, P., McPhaden, M.J., 1991. Variability of sea surface temperature in eastern equatorial Pacific during 1986-88. J. Geophys. Res. 96 (C6), 10,533 – 10,566.

Helfand, J.S., Podber, D.P., McCormick, M.J., 1999. Effect of heat flux on thermocline formation. In: Spaulding, M.L., Butler H. J. (Eds.), Proceedings on 6th Intern. Conf. on Estuarine and Coastal Modeling, ASCE, pp.130-147.

Hydroqual, Inc, 1998. Development and Application of a Modeling Framework to Evaluate Hurricane Impacts on Surficial Mercury Concentrations in Lavaca Bay. Draft Report, Aluminium Co. of America, Point Comfort, TX.

Ippen, A.T., 1966. Estuary and Coastline Hydrodynamics. McGraw-Hill, New York.

Luettich, R.L., Westerink, J.J., 2003. Formulation and numerical implementation of the 2D/3D ADCIRC finite element model version 43.XX. Paper presented at 2003 ADCIRC Workshop, NRL, Stennis, MS.

Luettich, R.A. Jr., Muccino, J., Foreman, M.G.G., 2002. Consideration in the calculation of vertical velocity in three-dimensional circulation models. J. Atmopheric and Oceanic Technology, 19(12), 2063-2076.

Luettich, R.A. Jr. Muccino, J., 2001. Summary of vertical velocity calculation methods as considered for 3D ADCIRC hydrodynamic model. Paper presented at 2001 ADCIRC Workshop, NRL, Stennis, MS.

Luettich, R.A. Jr., Hu, S., Westerink, J.J., 1994. Development of the direct stress solution technique for three-dimensional hydrodynamic models using finite element. Int. J. Num. Meth. Fluids, 19, 295-319.

Luettich, R.A. Jr., Westerink, J.J., Scheffner, N.W., 1992a. ADCIRC: An Advanced Three-Dimensional Circulation Model for Shelves, Coasts, and Estuaries. Report 1, Technical Report DRP-92-6, Dredging Res. Prog., USACE, Washington, DC.

Luettich, R.A. Jr., Westerink, J.J., Scheffner, N.W., 1992b. ADCIRC: An Advanced Three-Dimensional Circulation Model for Shelves, Coasts, and Estuaries. Report 2, Technical Report DRP-92-6, Dredging Res. Prog., USACE, Washington, DC.

Lynch, D.R., Officer, C.B., 1985. Analytic test case for three-dimensional hydrodynamic models. Int. J. Num. Meth. Fluids, 5, 529-543.

Mellor, G.L., 1998. User guide for a three-dimensional, primitive equation, numerical ocean model. Program in Atmospheric and Ocean Sciences, Princeton Univ., Princeton, NJ.

Mellor, G.L., Oey, L.Y., Ezer, T., 1998. Sigma coordinate pressure gradient and the sea mount problem. J. Atmospheric and Oceanic Technology, 15(5), 1122-1131.

Mellor, G. L., Hakkinen, S., Ezer, T., 1999. A generalization of a sigma coordinate ocean model and an intercomparison of model vertical grids. In: Pinardi, N., Woods, J. (Eds.), Ocean Forecasting: Conceptual Basis and Applications, Springer-Verlag Publ., London, pp. 55-72.

Mellor, G.L. Yamada, T., 1982. Development of a turbulence closure model for geophysical fluid problems. Reviews of Geophysics and Space Physics, 20, 851-875.

Muccino, J.C., Gray, W.G., Foreman, G. G., 1997. Calculation of vertical velocity in three dimensional, shallow water equation, finite elements model. Int. J. Num. Meth. Fluids, 25, 779-802.

Palermo, M.R., Clausner, J.E., Rolling M.P., Williams, G.L., Myers, T.E., Fredete, T.J., Randall, R.E., 1998. Guidance for Subaqueous Dredged Material Capping. Dredging Operations and Environmental Research Program, Technical Report DOER-1, Waterways Experiment Stations, U.S. Army Corps of Engineers, Washington, DC.

Pandoe, W.W., Edge, B.L., 2003. Three-dimensional hydrodynamic model, study cases for quarter annular and idealized ship channel problems. Ocean Engineering, 30, 1117-1135.

Partheniades, E., 1990a. Stratified flow, salinity intrusion, and transport processes. In: Herbich, J.B. (Ed.), Handbook of Coastal and Ocean Engineering, Vol. 3, Gulf Publishing Co., Houston, TX, pp. 881-984.

Partheniades, E., 1990b. Estuarine sediment dynamics and shoaling processes. In: Herbich, J.B. (Ed.), Handbook of Coastal and Ocean Engineering, Vol. 3, Gulf Publishing Co., Houston, TX, pp. 985-1071.

Pond, S., Pickard, G.L., 1995. Introductory Dynamical Oceanography, 2nd ed., Butterworth-Heinemann, Oxford, UK.

Ribbe, J., and Holloway, P. E., 2001. A model of suspended sediment transport by internal tides. Continental Shelf Research, 21, 395-422.

Robertson, R., Padman, L., and Levine, M. D., 2001. A correction of the baroclinic pressure gradient term in the Princeton Ocean Model. J. Atmos. Oceanic Technol.,18 (6), 1068 – 1075.

Rutgers Ocean Modeling Group, 2004. Test problems: Gravitational adjustment of density in a flat channel, Regional Ocean Model System (ROMS). http://www.ocean-modeling.org/index.php, Institute of Marine and Coastal Sciences, Rutgers University, New Brunswick, NJ.

Scheffner, N., 1999. A large domain convection diffusion based finite element transport model. In: Spaulding, M.L., Butler, H.L. (Eds.), Proc. 6th Intern. Conf. Estuarine and Coastal Modeling, ASCE, pp.194-208.

Soulsby, R., 1997. Dynamics of Marine Sands. Thomas Telford Publ., London, UK.

Van Ledden, M., 2003. Sand Mud Segregation in Estuaries and Tidal Basins, Communications on Hydraulic and Geotechnical Engineering. Report No.03-2, Dept. of Civil Engineering and Geoscience, Delft University of Technology, Delft, The Netherlands.

Van de Kreeke, J., 2002. An analytical model for the morphodynamics of a trench in the presence of tidal currents. Continental Shelf Research, 22, 1811-1920.

Van Rijn, L.C., 2003. Sand transport by currents and waves; general approximation formulae. In: Proceedings Coastal Sediments 2003, TRU Consulting and Dand Inc, Clearwater Beach, FL.

Van Rijn, L.C., 1993. Principles of Sediment Transport in Rivers, Estuaries and Coastal Seas. Aqua Publications, Amsterdam, The Netherlands.

Van Rijn, L.C., 1986. Sedimentation of Dredged Channels by Currents and Waves. Delft Hydraulics Communication no. 369, Delft Hydraulics, Delft, The Netherlands.

Walstra, D.J.R., Van Rijn, L.C., Hoogewoning, S.E., Aarnikhof, S.G.J., 1999. Modeling of sedimentation of dredged trenches and channel under the combined action of tidal currents and wave. In: Kraus, N.C., McDougal, W.G. (Eds.), Proceedings Coastal Sediment 1999, ASCE, pp.2355-2370.

Whitehouse, R., Soulsby, R.R., Roberts, W., Mitchener, H., 2000. Dynamics of Estuarine Muds. Thomas Telford Publ., London, UK.

APPENDIX A

ADCIRC 3D – TRANSPORT

DESCRIPTION FOR SETUP AND INPUT FILES

Setup and Input files:

#	File name	Description
A.1	**Fort.15**	General model Setup
A.2	**Fort.11**	Initial condition for Salinity, Temperature and Density (Applicable if IDEN = 1)
A.3	**Fort.13**	Elevation (vertical) of F. E. grid node (if IGC = 0)
A.4	**Fort.10**	Baroclinic and Transport Setup (if IDEN = 10)
A.5	**Icd_sal.grd**	Initial condition for Salinity (Applicable if IDEN = 10 and ISTD = 1, 2)
A.6	**Icd_sal.grd**	Initial condition for Temperature (Applicable if IDEN = 10 and ISTD = 1, 2)
A.7	**Icd_sal.grd**	Initial condition for Suspended Sediment Concentration (Applicable if IDEN = 10 and ISTD = 2)

Example of Fort.15

```
ADCIRC Model                   ! 32 CHARACTER ALPHANUMERIC RUN DESCRIPTION
ADCIRC Run                    ! 24 CHARACTER ALPHANUMERIC RUN IDENTIFICATION
1                             ! NFOVER
1                             ! NABOUT
1                             ! NSCREEN
0                             ! IHOT
1                             ! ICS
1                             ! IM
1                             ! NOLIBF
1                             ! NOLIFA
1                             ! NOLICA
1                             ! NOLICAT
0                             ! NWP
0                             ! NCOR
0                             ! NTIP - TIDAL POTENTIAL OPTION PARAMETER
0                             ! NWS
0.0050                        ! TAU0 - WEIGHTING FACTOR IN GWCE
4.000000                      ! DT - TIME STEP (IN SECONDS)
0.000000                      ! STATIM - STARTING SIMULATION TIME IN DAYS
0.000                         ! REFTIME
10.000000                     ! RNDAY - TOTAL LENGTH OF SIMULATION (IN DAYS)
1.000                         ! DRAMP - DURATION OF RAMP FUNCTION (IN DAYS)
0.350 0.300 0.350             ! TIME WEIGHTING FACTORS FOR THE GWCE EQUATION
0.050                         ! Ho
13089.29 11999.34             ! SLAM0,SFEA0
```

```
0.0025                       ! FFACTOR
2.000                        ! ESL
0.00010                      ! CORI
0                            ! NTIF
1                            ! NBFR
M2                           ! BOUNTAG
0.000140518902509  0.976  146.220   ! CONST.FREQ, NODAL FACTOR,EQUIL. ARG.
M2                                  ! AMPLITUDE AND PHASE
   0.20000000  0.000
       :
       :
   0.20000000  0.000
90.000                          ! ANGINN
1                               ! # OF FREQUENCIES IN SPECIFIED NORMAL FLOW BC
normflow                        ! PERIODIC NORMAL FLOW FORCING ON FLOW BC
0.000000000000000 1.000 0.000   ! FORCING FREQ., NODAL FACTOR, EQUIL. ARGUMENT
M2                              ! PERIODIC NORMAL FLOW
0.20000000 0.000                 ! AMPLITUDE AND PHASE (IN DEGREES)
     :
     :
0.20000000 0.000                 ! AMPLITUDE AND PHASE (IN DEGREES)
-1 0.000 90.000 900             ! NOUTE,TOUTSE,TOUTFE,NSPOOLE
4                               ! TOTAL NUMBER OF ELEVATION RECORDING STATIONS
15617.77971026 12000.58718679   !! 408
21121.00000000 12003.00000000   !! 905
23724.99388844 11982.25459582   !! 1428
26026.81745088 11998.86815195   !! 1759
-1 0.000 90.000 900             ! NOUTV,TOUTSV,TOUTFV,NSPOOLV
4                               ! NSTAV
15617.77971026 12000.58718679   !! 408
21121.00000000 12003.00000000   !! 905
23724.99388844 11982.25459582   !! 1428
26026.81745088 11998.86815195   !! 1759
-1 0.000 90.000 3600            ! NOUTGE,TOUTSGE,TOUTFGE,NSPOOLGE
-1 0.000 90.000 3600            ! NOUTGV,TOUTSGV,TOUTFGV,NSPOOLGV
0                               ! NHARF
0.000 0.000 0 0.000             ! THAS,THAF,NHAINC,FMV
0 0 0 0                         ! NHASE,NHASV,NHAGE,NHAGV
1 1800                          ! NHSTAR,NHSINC
1 0 1.000000000E-005 25         ! ITITER, ISLDIA, CONVCR, ITMAX
0                               ! IDIAG
10                              ! IDEN
2    0.0025                     ! slip code and slip coefficient
0.00001  0.0002                 ! free surface and bottom roughnesses
0.50   0.50   0.50              ! time stepping coefficients (alpha1,2,3)
1    9                          ! f.e. grid code, # nodes in f.e. grid
50  0.0001  0.003               ! e.v. code, evmin, evcon coefficient
0.5  0.5                        ! theta1,theta2
1  0.0  180.0  3600  4          ! DTS station output
 408  905 1428 1759             ! SVHOUT(I), I=1,NHN3DSV; HORZ NODE NUMBER
1  0.0  180.0  3600  4          ! 3D-velocity station output (fort.42)
 408  905 1428 1759             ! SVHOUT(I), I=1,NHN3DSV; HORZ NODE NUMBER
0  0.0  180.0  7200  0          ! turbulence station output
0  0.0  180.000   12            ! DTS global output
1  0.0   180.0  3600            ! velocity global output (fort.45)
0  0.00  180.0  0               ! turbulence global output
```

A.1. File: Fort.15

```
RUNDES                     ! 32 character alphanumeric run description
RUNID                      ! 24 character alphanumeric run identification
NFOVER                     ! Nonfatal error override option
NABOUT                     ! abbreviated output option parameter
NSCREEN                    ! output to unit 6 parameter
IHOT                       ! hot start option parameter
ICS                        ! coordinate system option parameter
IM                         ! model run type: 0=2DDI, 1=3DL(VS), 2=3DL(DSS)
NOLIBF                     ! nonlinear bottom friction option
NOLIFA                     ! option to include finite amplitude terms
NOLICA                     ! option to include convective acceleration terms
NOLICAT                    ! option to consider time derivative of conv acc
                           terms
NWP                        ! variable bottom friction and lateral viscosity
                           option parameter
NCOR                       ! variable coriolis in space option parameter
NTIP                       ! tidal potential option parameter
NWS                        ! wind stress and barometric pressure option
                           parameter
NRAMP                      ! ramp function option
G                          !acceleration due to gravity - determines units
TAU0                       ! weighting factor in GWCE
DT                         ! time step (in seconds)
STATIM                     ! starting simulation time in days
REFTIME                    ! reference time (in days) for nodal factors and
                           equilibrium args
RNDAY                      ! total length of simulation (in days)
DRAMP                      ! duration of ramp function (in days)
A00, B00, C00              ! time weighting factors for the gwce equation
H0, NODEDRYMIN, NODEWETRMP, VELMIN
SLAM0,SFEA0                ! center of cpp projection (not used if ics=1,
                           ntip=0, ncor=0)
FFACTOR,Hb,theta,gamma     ! ffactor - homogeneous linear or nonlinear bottom
                           friction coefficient
ESL, EVC                   ! lateral eddy viscosity coefficient; ignored if
                           NWP=1
CORI                       ! coriolis parameter - ignored if NCOR = 1
NTIF                       ! total number of tidal potential constituents being
                           forced
NBFR                       ! total number of forcing frequencies on open
                           boundaries
BOUNTAG                    ! alpha descriptor of forcing frequency on next line
CONST. FREQ. (Hz*2*pi), NODAL FACTOR, EQUIL. ARG.
AMPLITUDE , PHASE          !amplitude (m) and phase (degrees) of harmonic
                           forcing function
ANGINN                     ! inner angle threshold
NBFR                       ! number of frequencies in specified normal flow
FORCING FREQUENCY, NODAL FACTOR, EQUILIBURIUM ARGUMENT
PERIODIC NORMAL FLOW
AMPLITUDE , PHASE (IN DEGREES)
NOUTE,TOUTSE,TOUTFE,NSPOOLE             !elev station output info (unit 61)
NOUTV,TOUTSV,TOUTFV,NSPOOLV             !vel station output info (unit 62)
NSTAV                                   !total number of velocity recording
                                        stations
NOUTGE,TOUTSGE,TOUTFGE,NSPOOLGE         !global elevation output info (unit 63)
NOUTGV,TOUTSGV,TOUTFGV,NSPOOLGV         !global velocity output info (unit 64)
```

```
NHARF                                   !number of freqencies in harmonic
                                        analysis
THAS,THAF,NHAINC,FMV                    ! harmonic analysis parameters
NHASE,NHASV,NHAGE,NHAGV                 ! control harmonic analysis and output
                                        to units 51,52,53,54
NHSTAR,NHSINC                           ! hot start file generation parameters
ITITER, ISLDIA, CONVCR, ITMAX           ! algebraic solution parameters
------------------------------------------ 3D setup starting below ------------
                           -----------------------------
IDIAG
IDEN
ISLIP, KP
ZOB, ZOS
α1, α2,  α3
IGC, NFEN
IEVC, EVMIN, EVCON
THETA1, THETA2
I3DSD,TO3DSSD,TO3DFSD,NSPO3DSD,NHN3DSD
ISDHOUT(I), I=1,NHN3DSD
I3DSV,TO3DSSV,TO3DFSV,NSPO3DSV,NHN3DSV
SVHOUT(I), I=1,NHN3DSV
I3DST,TO3DSST,TO3DFST,NSPO3DST,NHN3DST
STHOUT(I), I=1,NHN3DST
I3DGD,TO3DSGD,TO3DFGD,NSPO3DGD
I3DGV,TO3DSGV,TO3DFGV,NSPO3DGV
I3DGT,TO3DSGT,TO3DFGT,NSPO3DGT
```

Description (additional) of input variables required for 3D Setup of UNIT 15 (fort.15):

Variable	Type	Description (Fort.15)
IDIAG	Integer	= 0 no nonfatal diagnostic output printed to units 2 or 16 = 1 serious, nonfatal diagnostic output printed to unit 16 = 2 serious, nonfatal diagnostic output printed to unit 16
IDEN	Integer	= 0 barotropic model run = 1 diagnostic baroclinic model run = 2 prognostic baroclinic model run, salinity only = 3 prognostic baroclinic model run, temperature only = 4 prognostic baroclinic model run, salinity and temperature = 10 TAMU's baroclinic model run Note: For all baroclinic model runs, the initial density field is read in from UNIT 11
ISLIP, KP	Integer, Real	slip code & slip coefficient islip = 0, no slip bottom b.c. islip = 1, linear slip bottom b.c. islip = 2, quadratic slip bottom b.c
Z0S, Z0B	Real, Real	free surface & bottom roughnesses (const over horiz); if the turbulent length scale is determined by q2l eqn and a slip coefficient is used, this should be the thickness of the constraint stress layer (e.g., 1 m) below the bottom boundary node.
ALP1,ALP2,ALP3	Real,	time weighting coefficients for the velocity solution.

	Real, Real	0.= fully explicit, 0.5=time centered, 1.= fully implicit ALP1 weights the Coriolis term ALP2 weights the bottom friction terms ALP3 weights the vertical diffusion term

IGC,NFEN	Integer, Integer	f.e. grid code and # nodes in f.e. grid
		IGC = 0, f.e. grid read from UNIT 13 (fort.13)
		IGC = 1, uniform f.e. grid generated
		IGC = 2, log f.e. grid generated
		IGC = 3, log linear f.e. grid generated
		IGC = 4, double log f.e. grid generated
		IGC = 5, P-grid generated
		IGC = 6, sine grid generated

IEVC, EVMIN, EVCON	Integer, Real, Real	E.V. code, E.V. minimum value and E.V. constant NOTE: • EVCON is only used for some of the E.V. formulations as discussed below. • In cases where EV is specified to vary linearly over the lower 20% of the water column, it actually varies linearly with a constant slope up to the vertical FE grid node that is less than or equal to the 20% location. The value is constant as specified at all FE grid nodes above the 20% location. The E.V. above and below the 20% level is joined by one additional linearly varying segment. • The E.V. is constrained to always be greater than or equal to EVMIN as specified in the UNIT 15 file. ievc = 0-9, EV constant in time & horizontal space 0 - EV read in from UNIT 12 (may vary vertically) - EVCON is not used 1 - EV = EVCON ievc = 10-19 EV proportional to omega*h*h (Lynch and Officer (1986) Lynch and Werner (1987, 1991)) * 10 - EV = omega*h*h/10 over the entire water column 11 - EV = omega*h*h/1000 at bottom varies linear over lower 20% of wc = omega*h*h/10 in upper 80% of w.c. NOTE:For this EV formulation, evcon is not used and omega is hardwired for a 12.42 hour tide. ievc = 20-29 EV proportional to kappa U* z 20 - EV = 0.41U*Zo at bottom = 0.41U*Z over entire water column 21 - EV = 0.41U*Zo at bottom = 0.41U*Z in lower 20% of water col = 0.082U*h in upper 80% of water col where: U* is the friction velocity Note: For this EV formulation, evcon is not used.

		ievc=30-39, EV proportional to Uh (Davies 1990) 30 - EV = 0.025|U|h/9.001 over entire water column 31 - EV = evcon|U|h over entire water column 32 - EV = 0.025|U|h/9.001 in upper 80% of wc = 0.000025h|U|/9.001 at bottom varies linear over lower 20% of wc 33 - EV = evcon|U|h in upper 80% of wc = evcon|U|h/1000. at bottom varies linear over lower 20% of wc where: U is depth averaged velocity Note: For this EV formluation, evcon is used only for ievc=31,33 * ievc=40-49, EV proportional to U*U (Davies 1990) 40 - EV = 2|UU|/9.001 over entire water column 41 - EV = evcon|UU| over entire water column 42 - EV = 2|UU|/9.001 in upper 80% of wc = 0.002|UU|/9.001 at bottom varies linear over lower 20% of wc 43 - EV = evcon|UU| in upper 80% of wc = evcon|UU|/1000. at bottom varies linear over lower 20% of wc where: U is depth averaged velocity Note: For this EV formluation, evcon is used only for ievc = 41 or 43 Ievc = 50, EV computed from Mellor-Yamada 2.5 Turbulence closure. Note: For this EV formulation, evcon is not used.
THETA1, THETA2	Real, Real	time weighting coefficients for the MY2.5 turbulence soln. (applicable if IEVC = 50) 0.= fully explicit, 0.5=time centered, 1.= fully implicit * THETA1 weights the dissipation term THETA2 weights the vertical diffusion term
I3DSD	Integer	= 0 no station 3D T,S,D info is output to unit 41 = 1 station 3D T,S,D info is output in ASCII format
TO3DSSD	Real	the number of days after which station 3d T,S,D are written to unit 41.
TO3DFSD	Real	the number of days after which station 3d T,S,D cease to be written to unit 41.
NSPO3DSD	Integer	the number of time steps at which data is written to unit 41. (i.e., data is output to unit 41 every NSPO3DSD time steps after TO3DSSD.)
NHN3DSD	Integer	the number of stations in the horizontal to output station 3d T,S,D
ISDHOUT(I), I=1,NHN3DSD	Integer	horizontal node numbers (from external mode grid) to be used as 3d T,S,D output stations (only include this line if I3DSD is not = 0)

I3DSV	Integer	= 0 no station 3d velocities are output to unit 42 = 1 station 3d velocities are output in ASCII format = 2 station 3d velocities are output in binary format
TO3DSSV	Real	The number of days after which station 3d velocities are written to unit 42.
TO3DFSV	Real	The number of days after which station 3d velocities to be written to unit 42.
NSPO3DSV	Integer	The number of time steps at which data is written to unit 42. (i.e., data is output to unit 42 every NSPO3DSV time steps after TO3DSSV.)
NHN3DSV	Integer	The number of stations in the horizontal to output station 3d velocities.
ISVHOUT(I), I=1,NHN3DSV	Integer	horizontal node numbers (from external mode grid) to be used as 3d velocity output stations (only include this line if I3DSV is not = 0)
I3DST	Integer	= 0 no station 3d turbulence variables output to unit 43 = 1 station 3d turbulence variables output in ASCII format
TO3DSST	Real	The number of days after which station 3d turbulence variables are written to unit 43.
TO3DFST	Real	The number of days after which station 3d turbulence variables cease to be written to unit 43.
NSPO3DST	Integer	The number of time steps at which data is written to unit 43. (i.e., data is output to unit 43 every NSPO3DSV time steps after TO3DSSV.)
NHN3DST	Integer	The number of stations in the horizontal to output station 3d velocities.
ISTHOUT(I), I=1,NHN3DST	Integer	Horizontal node numbers (from external mode grid) to be used as 3d velocity output stations (only include this line if I3DST is not = 0)
I3DGD	Integer	= 0, no global 3d T,S,D info is output to unit 44 = 1, global 3d T,S,D info is output in ASCII format
TO3DSGD	Real	The number of days after which global 3d T,S,D are written to unit 44.
TO3DFGD	Real	The number of days after which global 3d T,S,D cease to be written to unit 44.
NSPO3DGD	Integer	the number of time steps at which data is written to unit 44. (i.e., data is output to unit 44 every NSPO3DGD time steps after TO3DSGD.)
I3DGV	Integer	= 0 no global 3d velocities are output to unit 45 = 1 global 3d velocities are output in ASCII format = 2 global 3d velocities are output in binary format
TO3DSGV	Real	The number of days after which global 3d velocity data is written to unit 45.
TO3DFGV	Real	The number of days after which global 3d velocity data ceases to be written to unit 45.
NSPO3DGV	Integer	The number of time steps at which data is written to unit 45. (i.e., data is output to unit 45 every NSPO3DGV time steps

		after TO3DSGV.)
I3DGT	Integer	= 0 no global 3d turbulence variables output to unit 46 = 1 global 3d turbulence variables output in ASCII format
TO3DSGT	Real	The number of days after which global 3d turbulence variables are written to unit 46.
TO3DFGT	Real	The number of days after which global 3d turbulence variables cease to be written to unit 46
NSPO3DGT	Integer	The number of time steps at which data is written to unit 46. (i.e., data is output to unit 46 every NSPO3DGT time steps after TO3DSGT.)

A.2. Description of Input Variables from UNIT 11 (FORT.11)

(Note, this is used only if IDEN=1)

```
   HEADER LINE 1
   HEADER LINE 2
   NVN - number of nodes in vertical, must match NFEN
   DO I=1,NP
     DO J=1,NFEN
       NHNN,NVNN,SIGT(NHNN,NVNN),TEMP(NHNN,NVNN),SAL(NHNN,NVNN)
       END DO
     END DO

   NHNN = HORIZONTAL NODE NUMBER
   NVNN = VERTICAL NODE NUMBER
   SIGT(NHNN,NVNN) = SIGMA T VALUE (KG/M^3) (=DENSITY-1000)
   TEMP(NHNN,NVNN) = TEMPERATURE (DEG C)
   SAL(NHNN,NVNN) = SALINITY (PSU)

NOTE: J=1 AT BOTTOM, J=NFEN AT SURFACE
```

A.3. Description of Input Variables from UNIT 13 (FORT.13)

(Note, this is used only if IGC=0)

```
SIGMA(I), I=1,NFEN
SIGMA(I) = ELEVATION OF F.E. GRID NODE I (FROM b TO a)
```

A.4. Description of Input Variables from UNIT 10 (FORT.10)

(Note, this is used only if IDEN=10)

A.4.1. Example Fort.10:

```
2                           ! ISTD
12                          ! DelTr
0  9                        ! IGC, NFEN
0.5   0.5                   ! theta1, theta2;
20.0   0.00001              ! Dh, Dv
5.0 0.001 0.5        ! # of day for DTRAMP function, BCRAMPmin, BCRAMPmax
const                       ! ALPHA NUMERIC DESCRIPTION OF NORMAL FLOW
```

```
3.0  19.0  0.000
       :
       :
3.0  19.0  0.000
0                          !IFLOWBC: 0 = essential; 1 = natural
0                          !ICON2DEN (only if ISTD = 2)
sediment transport setup (ie. ISTD = 2)
4                          ! ISEDTYPE: 1-3 = Cohesive; 4-6 = noncohesive
3  0.1  0.2 0.3            ! NDI (# of D50), D50(i=1,NDI); in mm unit
1  8.0  45.0               ! iwave, Twave, Dirwav
1                          ! ierospec
0.0 180. 900 4             ! STD station output parameters(FORT.141)
408  905 1428 1759         ! SSHOUT(I), I=1,NHN3DSS; HORZ NODE NUMBER
1 0.0 180. 10800 4         ! Turb station output parameters(FORT.151)
408  905 1428 1759         ! SSHOUT(I), I=1,NHN3DST; HORZ NODE NUMBER
1 0.0 180. 900 4           ! Conc. station output parameters(FORT.181)
408  905 1428 1759         ! SSHOUT(I), I=1,NHN3DSS; HORZ NODE NUMBER
1 0.0 180. 3600            ! Global STD output parameters(FORT.144)
1 0.0 180. 21600           ! Global TURB output parameters(FORT.154)
1 0.0 180. 3600            ! Global Conc. output parameters(FORT.184)
sediment transport setup (ie. ISTD = 2)
2                          ! ISEDTYPE: 1-3 = Cohesive; 4-6 = noncohesive
1200.0                     ! grain size in mm unit, to compute TAUcre only
                            baroclinic setup (ie. IDEN = 1 or 10)
1 0.0 180. 21600 4         ! Baroclinic station output parameters(FORT.161)
408  905 1428 1759         ! SSHOUT(I), I=1,NHN3DSB; HORZ NODE NUMBER
0 0.0 180. 21600           ! Global Baroclinic output parameters(FORT.163)
```

A.4.2. VARIABLES on Fort.10:

```
ISTD
DelTr
IGC,NFEN
theta1, theta2
Dh, Dvmin
DTRAMP, BCRAMPmin, BCRAMPmax
ALPHANORM
QSAM(I,J), QTAM(I,J), QCAM(I,J)
IFLOWBC
ICON2DEN
‘Sediment Transport Setup (e.g. ISTD = 2)’     ! ALPHANUMSED; Alpha numeric for
sediment
ISEDTYPE
NDI, DI1, DI2, …, DI(NDI)
IWAVE, TWAVE, DIRWAVE
IEROSPEC
I3DSD, TO3DSSD, TO3DFSD, NSPO3DSD, NHN3DSD
ISDHOUT(I), I=1,NHN3DSD
I3DST, TO3DSST, TO3DFST, NSPO3DST, NHN3DST
ISTHOUT(I), I=1,NHN3DST
I3DSC, TO3DSSC, TO3DFSC, NSPO3DSC, NHN3DSC
ISCHOUT(I), I=1,NHN3DSC
I3DGD, TO3DSGD, TO3DFGD, NSPO3DGD
I3DGT, TO3DSGT, TO3DFGT, NSPO3DGT
I3DGC, TO3DSGC, TO3DFGC, NSPO3DGC
 ‘Baroclinic setup (e.g. IDEN=10)’             ! ALPHANUMBC; Alpha numeric for
baroclinic
I3DSB, TO3DSSB, TO3DFSB, NSPO3DSB, NHN3DSB
ISBHOUT(I), I=1,NHN3DSB
I3DGB, TO3DSGB, TO3DFGB, NSPO3DGB
```

A.4.3. Description of Input Variables from UNIT 10

Variable	Type	Description (Fort.10)
ISTD	Integer	0=no Transport sol; 1=S, T, D sols; 2=S,T,D and C sols Note: For all transport model runs, the initial constituents fields are read in from initial condition files: *icd_sal.grd*, *icd_temp*.grd and *icd_conc.grd*.
DelTr	Real	internal transport time step in second

IGC,NFEN	Integer,
	Integer
		f.e. grid code and # nodes in f.e. grid
		igc = 0, f.e. grid read from UNIT 13 (fort.13)
		igc = 1, uniform f.e. grid generated
		igc = 2, log f.e. grid generated
		igc = 3, log linear f.e. grid generated
		igc = 4, double log f.e. grid generated
		igc = 5, P-grid generated
		igc = 6, sine grid generated

theta1, theta2	Real, Real	Time weighting the dissipation the vertical diffusion terms, applicable to subroutine TURB. 0 = fully explicit, 0.5 = time centered, 1 = implicit
Dh, Dv_{min}	Real, Real	Horizontal and Vertical Transport Diffusion coefficients
DTRAMP	Real	Number of day for Baroclinic RAMP function
BCRAMPmin	Real	Minimum ramp function for BCPG term; for dam break case this value is 0.01
BCRAMPmax	Real	Maximum ramp function for BCPG term; for dam break case this value is 1.0
ALPHANORM	Alpha-numeric	Alpha numeric description of normal flow forcing data set (32 characters)
QSAM(I)	Real	Boundary forcing data for Constituent #1 (SALINITY) Note: only include this line if NBFR (in fort.15) is not = 0
QTAM(I)	Real	Boundary forcing data for Constituent #2 (TEMPERATURE) Note: only include this line if NBFR (in fort.15) is not = 0
QCAM(I)	Real	Boundary forcing data for Constituent #3 (CONCENTRATION) Note: only include this line if NBFR (in fort.15) is not = 0, and ISTD = 2
IFLOWBC	integer	Boundary forcing type: = 0 = essential, = 1 = natural
ICON2DEN	integer	Density function: 0 = RHO(S, T); 1 = RHO (S, T, C)
I3DSD	Integer	= 0 NO station 3D T,S,D info = 1 station 3D T,S,D info is output in ASCII format to fort.141, fort 142 and fort.143 for Salinity, Temperature and Density, respectively
TO3DSSD	Real	The number of days after which station 3D T, S, D are

		written to output units.
TO3DFSD	Real	the number of days after which station 3D T, S, D cease to be written to output units.
NSPO3DSD	Integer	The number of time steps at which data is written to output units (i.e., data is written to output units every NSPO3DSD time steps after TO3DSSD.)
NHN3DSD	Integer	The number of stations in the horizontal to output station 3D T, S, D.
ISDHOUT(I), I=1,NHN3DSD	Integer	Horizontal node numbers (from external mode grid) to be used as 3D T, S, D output stations (only include this line if I3DSD is not = 0)
I3DST	Integer	= 0 NO station 3D Turbulence info output = 1 station 3D Turbulence info is output in ASCII format fort.151 for q20, l_t and Dv; and fort.153 for BV freq. and Ri
TO3DSST	Real	The number of days after which station 3D Turbulence is written to output units.
TO3DFST	Real	The number of days after which station 3D Turbulence cease to be written to output units.
NSPO3DST	Integer	The number of time steps at which data is written to output units (i.e., data is written to output units every NSPO3DST time steps after TO3DSST.)
NHN3DST	Integer	The number of stations in the horizontal to output station 3D Turbulence
STHOUT(I), I=1,NHN3DST	Integer	Horizontal node numbers (from external mode grid) to be used as 3D turbulence output stations (only include this line if I3DST is not = 0)
I3DSC	Integer	= 0 NO station 3D Concentration info output = 1 station 3D Concentration info is output in ASCII format fort.181
TO3DSSC	Real	The number of days after which station 3D Concentration are written to output units.
TO3DFSC	Real	the number of days after which station 3D Concentration cease to be written to output units.
NSPO3DSC	Integer	The number of time steps at which data is written to output units (i.e., data is written to output units every NSPO3DSC time steps after TO3DSSC.)
NHN3DSC	Integer	The number of stations in the horizontal to output station 3D Concentration
ISCHOUT(I), I=1,NHN3DSC	Integer	Horizontal node numbers (from external mode grid) to be used as 3D Concentration output stations (only include this line if I3DSC is not = 0)
I3DGD	Integer	= 0 no Global 3D T,S,D info output. = 1 Global 3D T,S,D info are written in ASCII format to output units fort.143, fort 144 and fort.145 for Salinity, Temperature and Density, respectively
TO3DSGD	Real	The number of days after which global 3D T, S, D is written to output units.

TO3DFGD	Real	The number of days after which global 3D T, S, D cease to be written to output units.
NSPO3DGD	Integer	The number of time steps at which data is written to output units. (i.e. data is written to output units every NSPO3DGD time steps after TO3DSGD.)
I3DGT	Integer	= 0 no Global 3D T,S,D info output. = 1 Global 3D T,S,D info are written in ASCII format to output units fort.154 for q20, l_t and Dv; and fort.156 for BV freq. and Ri#
TO3DSGT	Real	The number of days after which global 3D turbulence is written to output units.
TO3DFGT	Real	The number of days after which global 3D turbulence cease to be written to output units.
NSPO3DGT	Integer	The number of time steps at which data is written to output units. (i.e. data is written to output units every NSPO3DGT time steps after TO3DSGT.)
I3DGD	Integer	= 0 no Global 3D Concentration info output. = 1 Global 3D Concentration info are written in ASCII format to FORT.184.
TO3DSGD	Real	The number of days after which global 3D Concentration is written to output units.
TO3DFGD	Real	The number of days after which global 3D Concentration cease to be written to output units.
NSPO3DGD	Integer	The number of time steps at which data is written to output units. (i.e. data is written to output units every NSPO3DGC time steps after TO3DSGC.)
ALPHANUMSED	Alpha-numeric	'sediment transport setup (ie. ISTD = 2)' → Alpha Numeric Description
ISEDTYPE	Integer	SEDIMENT Type: 1 = Cohesive; Partheniades fomulation 2 and 3 = n/a yet 4 = noncohesive – Van Rijn fomulation 5 and 6 = n/a yet
NDI	Integer	Number grain sizes will be used
Di(i)	Real	The ith grain size [mm] if ISEDTYPE = 1-3 (cohesive) rho mud [kg/m3] if ISEDTYPE = 4-6 (non-cohesive)
IWAVE	Integer	Whether the wave field is specified (=1) or not (=0)
TWAVE,	Real	Wave period (assumed constant for entire domain)
DIRWAV	Real	Angle between incoming wave and current, and assumed constant for entire domain.
IEROSPEC	integer	Option whether different grain size at different location (=1), then the distribution of grain size (in percentage) must be specified from external file called **ierocode(*i*).grd**, where (*i*) is the index of grain size
ALPHANUMBC	Alpha-numeric	'baroclinic setup (ie. IDEN = 10)' → Alpha Numeric Description
I3DSB	Integer	= 0 NO station 3D Baroclinic info output

		= 1 station 3D Baroclinic info is output in ASCII format to fort.161
TO3DSSB	Real	The number of days after which station 3D Baroclinic are written to output units.
TO3DFSB	Real	the number of days after which station 3D Baroclinic cease to be written to output units.
NSPO3DSB	Integer	The number of time steps at which data is written to output units (i.e., data is written to output units every NSPO3DSB time steps after TO3DSSB.)
NHN3DSB	Integer	The number of stations in the horizontal to output station 3D Baroclinic
ISBHOUT(I), I=1,NHN3DSB	Integer	Horizontal node numbers (from external mode grid) to be used as 3D Baroclinic output stations (only include this line if I3DSB is not = 0)
I3DGB	Integer	= 0 no Global 3D Baroclinic info output. = 1 Global 3D Baroclinic info are written in ASCII format to fort.163
TO3DSGB	Real	The number of days after which global 3D Baroclinic is written to output units.
TO3DFGB	Real	The number of days after which global 3D Baroclinic cease to be written to output units.
NSPO3DGB	Integer	The number of time steps at which data is written to output units. (i.e. data is written to output units every NSPO3DGB time steps after TO3DSGB.)

A.5. File: icd_sal.grd

(*note, this is used only if istd > 0*)

Description input variables listed by the line sequence within the line:

AGRID
NE,NP
JKI,X(JKI),Y(JKI),SAL(JKI) , JKI=1,NP
JKI,NHY,NM(JKI,1),NM(JKI,2),NM(JKI,3) , JKI=1,NE

Description (additional) of input variables ***icd_sal.grd***:

Variable	Type	Description
AGRID	Alpha Numeric	Alpahanumeric grid identification (<=24 characters)
NE,NP	Integer	Number of elements and number of nodal points respectively
X(JKI),Y(JKI) JKI=1,NP	Real	Coordinates; nodes must be input in as-cending order; if ics=1 in unit 15 then x,y represent standard cartesian coordinates specified in length units consistent with other unit 15 input (typically meters or feet); if ics=2 in unit 15, then x,y represent degrees longitude (degrees east of greenwich is positive and degrees west of greenwich is negative) and degrees latitude (degrees north of the equator being positive

		and degrees south of the equator is negative) respectively. Bathymetric values are w.r.t. The geoid and are positive below the geoid and negative above the geoid. Bathymetric values above the geoid or any depth sufficiently small that nodes will dry, requires that the user enable the wetting/drying feature (nolifa=2 or 3) in the unit 15 input file.
SAL(JKI) JKI=1,NP	Real	Initial Salinity value for each node; defined uniform vertically.
NM(JKI,1), NM(JKI,2), NM(JKI,3), JKI=1,NE	Integer	Element connectivity specified with a counterclockwise orientation; elements must be read in in ascending order.
NHY	Integer	element type; note that the element type is not an active variable and that only 3 node linear triangles are operational in this version of the code
JKI	Integer	Index

A.6. File: icd_temp.grd

(*Note, this is used only if ISTD > 0*)

Description input variables listed by the line sequence within the line:

AGRID
NE,NP
JKI,X(JKI),Y(JKI),TEMP(JKI) , JKI=1,NP
JKI,NHY,NM(JKI,1),NM(JKI,2),NM(JKI,3) , JKI=1,NE

Description (additional) of input variables ***icd_temp.grd***:

Variable	Type	Description
AGRID	Alpha Numeric	Alpahanumeric grid identification (<=24 characters)
NE,NP	Integer	Number of elements and number of nodal points respectively
X(JKI),Y(JKI) JKI=1,NP	Real	Coordinates; nodes must be input in as-cending order; if ics=1 in unit 15 then x,y represent standard cartesian coordinates specified in length units consistent with other unit 15 input (typically meters or feet); if ics=2 in unit 15, then x,y represent degrees longitude (degrees east of greenwich is positive and degrees west of greenwich is negative) and degrees latitude (degrees north of the equator being positive and degrees south of the equator is negative) respectively. Bathymetric values are w.r.t. The geoid and are positive below the geoid and negative above the geoid. Bathymetric values above the geoid or any depth sufficiently small that nodes will dry, requires that the user enable the wetting/drying feature (nolifa=2 or 3) in the unit 15 input file.
TEMP(JKI) JKI=1,NP	Real	Initial water temperature value for each node; defined uniform vertically.

NM(JKI,1), NM(JKI,2), NM(JKI,3), JKI=1,NE	Integer	Element connectivity specified with a counterclockwise orientation; elements must be read in in ascending order.
NHY	Integer	Element type; note that the element type is not an active variable and that only 3 node linear triangles are operational in this version of the code
JKI	Integer	Index

A.7. File: icd_conc.grd

(*note, this is used only if ISTD =2*)

Description input variables listed by the line sequence within the line:

```
AGRID
NE,NP
JKI,X(JKI),Y(JKI),CONC(JKI) , JKI=1,NP
JKI,NHY,NM(JKI,1),NM(JKI,2),NM(JKI,3) , JKI=1,NE
```

Description (additional) of input variables ***icd_temp.grd***:

Variable	**Type**	**Description**
AGRID	Alpha Numeric	Alpahanumeric grid identification (<=24 characters)
NE,NP	Integer	Number of elements and number of nodal points respectively
X(JKI),Y(JKI) JKI=1,NP	Real	Coordinates; nodes must be input in as-cending order; if ics=1 in unit 15 then x,y represent standard cartesian coordinates specified in length units consistent with other unit 15 input (typically meters or feet); if ics=2 in unit 15, then x,y represent degrees longitude (degrees east of greenwich is positive and degrees west of greenwich is negative) and degrees latitude (degrees north of the equator being positive and degrees south of the equator is negative) respectively. Bathymetric values are w.r.t. The geoid and are positive below the geoid and negative above the geoid. Bathymetric values above the geoid or any depth sufficiently small that nodes will dry, requires that the user enable the wetting/drying feature (nolifa=2 or 3) in the unit 15 input file.
CONC(JKI) JKI=1,NP	Real	Initial suspended sediment concentration value (gr/l or kg/m ^{3}) for each node; defined uniform vertically.
NM(JKI,1), NM(JKI,2), NM(JKI,3), JKI=1,NE	Integer	Element connectivity specified with a counterclockwise orientation; elements must be read in in ascending order.

NHY	Integer	Element type; note that the element type is not an active variable and that only 3 node linear triangles are operational in this version of the code
JKI	Integer	Index

APPENDIX B

COMPARISON

BETWEEN STRUCTURED AND UNSTRUCTURED GRIDS

B.1. Source Code to Interpolate from Unstructured Grid Output File Fort.77 to Structured Grid Fort_regxxx.77

```
c************************************************************************c
c                                                                        c
c                        Data Conversion                                 c
c                   Irregular to Regular Grid                            c
c                         for FORT.77                                    c
c                                                                        c
c                     Wahyu Pandoe, Dec 2003                             c
c                                                                        c
c************************************************************************c

        PARAMETER(MNP=18500)
        PARAMETER(MNPI=18500)
        PARAMETER(MNE=36500)
        PARAMETER(MNEI=36500)
        PARAMETER(MNODES=16)
         PARAMETER(MNXX=100)
         PARAMETER(MNYY=100)

      DIMENSION STAID1(MNPI),STAID2(MNPI),STAID3(MNPI)
      real VALNOD(MNP,MNODES)
      real VALNODI(MNP,MNODES)
       REAL VAL(MNP*MNODES)
       REAL DIST(MNP*MNODES)
       REAL DISTMIN(MNODES)
       REAL VALMIN(MNODES)
       REAL*8 AREAS(MNE)
       real slayer(MNODES)
       real xnod(MNP,MNODES), ynod(MNP,MNODES), znod(MNP,MNODES)
      real X(MNP),Y(MNP),Z(MNP)
      real XI(MNPI),YI(MNPI),ZI(MNPI)
      real XI3(MNXX,MNYY,MNODES),YI3(MNXX,MNYY,MNODES)
       REAL ZI3(MNXX,MNYY,MNODES)
       REAL VALI(MNXX,MNYY,MNODES)
       REAL SUMVALODIST,SUMODIST
       REAL ZT(MNP),ZTI(MNPI)

       INTEGER LAY(MNODES)
       integer KDMIN(MNODES)
       INTEGER NFLAG(MNPI)
       INTEGER NM(MNE,3)
       INTEGER NNE(MNPI)
       INTEGER NFLG3(MNXX,MNYY)
```

```
      OPEN (UNIT=14,FILE='fort.14')
      OPEN (UNIT=15,FILE='fort_reg125.14')
      OPEN (UNIT=77,FILE='fort3.77')
      OPEN (UNIT=78,FILE='fort3_reg125.77')

c... original/irregular grid
       NLAY=1

c...regular grid
       NXX=113
       NYY=65
       NLAYI=1

c...READ FORT.14.TXT
      READ(14,'(A24)') AGRID
      READ(14,*) NE,NP
       WRITE(*,*) 'READ ORIGINAL/IRREGULAR GRID FORT.14 !!'
       do I=1,NP
         read(14,*) IDX,X(I),Y(I),Z(I)
         end do

C...READ THE GLOBAL CONNECTIVITY TABLE FROM UNIT 14
C...COMPUTE ELEMENT AREAS
      DO I=1,NE
        READ(14,*) JKI,NHY,NM(JKI,1),NM(JKI,2),NM(JKI,3)
        IF(JKI.NE.I) THEN
          WRITE(*,1228)
 1228     FORMAT(////,1X,'!!!!!!!!!!  WARNING - NONFATAL ',
     &                       'INPUT ERROR  !!!!!!!!!',
     &      //,1X,'YOUR ELEMENT NUMBERING IS NOT SEQUENTIAL ',
     &      /,1X,'CHECK YOUR UNIT 14 INPUT FILE CAREFULLY',//)
          ENDIF
        X1=X(NM(JKI,1))
        X2=X(NM(JKI,2))
        X3=X(NM(JKI,3))
        Y1=Y(NM(JKI,1))
        Y2=Y(NM(JKI,2))
        Y3=Y(NM(JKI,3))
        AREAS(JKI)=(X1-X3)*(Y2-Y3)+(X3-X2)*(Y1-Y3)  !2 X ACTUAL ELEMENT AREA
        IF(AREAS(JKI).LT.0.0) THEN
          WRITE(*,9899) JKI
 9899     FORMAT(////,1X,'!!!!!!!!!!  WARNING - FATAL ERROR !!!!!!!!!',
     &      //,1X,'THE CONNECTIVITY FOR ELEMENT ',I6,
     &            '  HAS BEEN INCORRECTLY SPECIFIED ',
     &      /,1X,'CHECK INPUT AND ENSURE THAT COUNTERCLOCKWISE',
     &           ' CONVENTION HAS BEEN USED ',
     &      //,1X,'!!!!!! EXECUTION WILL NOW BE TERMINATED !!!!!!',//)
          STOP
          ENDIF
        END DO      !FOR I=1,NE

       CLOSE(14)

c...read fort_reg125_14.txt
      READ(15,'(A24)') AGRIDI
      READ(15,*) NEI,NPI
       WRITE(*,*) 'READ NEW REGULAR GRID FORT_REGxxx.14'
       do I=1,NPI
         read(15,*) IDX,XI(I),YI(I),ZI(I)
         end do
```

```
       CLOSE(15)

c...define sigma layers
       slayer(1)=-1.00
       IF(NLAY.GT.1) THEN
         do nsig=2,nlay
           slayer(nsig)=slayer(nsig-1)+0.25
           end do
         END IF

c...define 3D domain of irreg grid
       do NH=1,NP
         do K=1,nlay
           zcoef=(slayer(K)-1.0)/(2.0)
           XNOD(NH,K)=X(NH)/1000.0
           YNOD(NH,K)=Y(NH)/1000.0
           ZNOD(NH,K)=Z(NH)*zcoef
           end do
         end do

c...read ADCIRC output data
       ICOUNT=0
       ITOTAL=0
c... LOOP over time step
c************************
      READ(77,'(A24)') AGRIDI
      READ(77,*) IN1,IN2,TIN3,IN4,IN5

C...WRITE TO OUTPUT
      WRITE(78,'(A24)') AGRIDI
      WRITE(78,*) IN1,NPI,TIN3,IN4,IN5

      DO WHILE (.NOT. EOF(77))
        READ (77, *) TSEC, NTIM
         WRITE(*,*) 'TIMESTEP =',NTIM
        ICOUNT = ICOUNT + 1
         DO I=1,NP
          READ (77, *) NOM, ZT(I)
          ITOTAL=ITOTAL+1
           END DO

C...DETERMINE THE NODES IN THE REG.GRID WHETHER INSIDE OR OUTSIDE THE DOMAIN
C...USING TRIANGULAR AREA METHODS.

C....INPUT COORDINATES OF ELEVATION RECORDING STATIONS THEN COMPUTE
C....THE ELEMENT NO. THE STATION LIES IN

      DO I=1,NPI
        NNE(I)=0
C         XEL(I)=XI(I)
C          YEL(I)=YI(I)
        AEMIN=1.0E+25
        KMIN=0

        DO K=1,NE
          N1=NM(K,1)
          N2=NM(K,2)
          N3=NM(K,3)
          X1=X(N1)
          X2=X(N2)
```

```
          X3=X(N3)
          X4=XI(I)
          Y1=Y(N1)
          Y2=Y(N2)
          Y3=Y(N3)
          Y4=YI(I)
          A1=(X4-X3)*(Y2-Y3)+(X2-X3)*(Y3-Y4)
          A2=(X4-X1)*(Y3-Y1)-(Y4-Y1)*(X3-X1)
          A3=(Y4-Y1)*(X2-X1)-(X4-X1)*(Y2-Y1)
          AA=ABS(A1)+ABS(A2)+ABS(A3)
          AE=ABS(AA-AREAS(K))/AREAS(K)
          IF(AE.LT.AEMIN) THEN
            AEMIN=AE
            KMIN=K
            ENDIF
          IF(AE.LT.1.0E-5) NNE(I)=K
          END DO

        IF(NNE(I).EQ.0) THEN
           NFLAG(I)=0             ! NODES OUTSIDE DOMAIN
          WRITE(*,9784) I
9784      FORMAT(/,1X,'NEW NODES ',I6,' DOES NOT LIE',
     &                 ' WITHIN ANY ELEMENT IN THE DEFINED OLD DOMAIN')
           ELSE
           NFLAG(I)=1             ! NODES INSIDE DOMAIN
          ENDIF

C....PRE-COMPUTE INFORMATION REQUIRED TO INTERPOLATE AT ELEV. RECORDING
STATIONS
        N1=NM(NNE(I),1)
        N2=NM(NNE(I),2)
        N3=NM(NNE(I),3)
        X1=X(N1)
        X2=X(N2)
        X3=X(N3)
        X4=XI(I)
        Y1=Y(N1)
        Y2=Y(N2)
        Y3=Y(N3)
        Y4=YI(I)
        STAID1(I)=((X4-X3)*(Y2-Y3)+(X2-X3)*(Y3-Y4))/AREAS(NNE(I))
        STAID2(I)=((X4-X1)*(Y3-Y1)-(Y4-Y1)*(X3-X1))/AREAS(NNE(I))
        STAID3(I)=(-(X4-X1)*(Y2-Y1)+(Y4-Y1)*(X2-X1))/AREAS(NNE(I))
         WEIGH1=ABS(STAID1(I))
         WEIGH2=ABS(STAID2(I))
         WEIGH3=ABS(STAID3(I))

C...******************************
C...COMPUTE ZA, ZI
C...******************************
C... FIND X1,X2,X3, Y1,Y2,Y3
C.....SET NODAL VALUES FOR EACH ELEMENT
           IE=NNE(I)
          NM1=NM(IE,1)
          NM2=NM(IE,2)
          NM3=NM(IE,3)

          ZN1=ZT(NM1)
          ZN2=ZT(NM2)
          ZN3=ZT(NM3)
```

```
C.....COMPUTE ELEMENT AVERAGES QUANTITIES (UNWEIGHTED)
              ZA=(ZN1+ZN2+ZN3)/3.

C.....COMPUTE ELEMENT AVERAGES QUANTITIES (WEIGHTED)
              ZTI(I)=(WEIGH1*ZN1+WEIGH2*ZN2+WEIGH3*ZN3)
        END DO      !FOR I=1,NPI

C...WRITE NEW OUTPUT
         WRITE(78,1109) TSEC, NTIM
         DO NH=1,NPI
           WRITE(78,1111) NH,ZTI(NH)
           END DO
 1109   FORMAT(2X,E12.6,4X,I8,2X)
 1111   FORMAT(2X,I7,4X,100(E12.6,2X))
         end do     !END OF DO WHILE NOT EOF(77) LOOP

      stop
      END
```

B.2. Comparison Contour Map Results between Structured and Unstructured Grid

B.2.1. Case #1 : CAPPING

Unstructured (irregular) grid

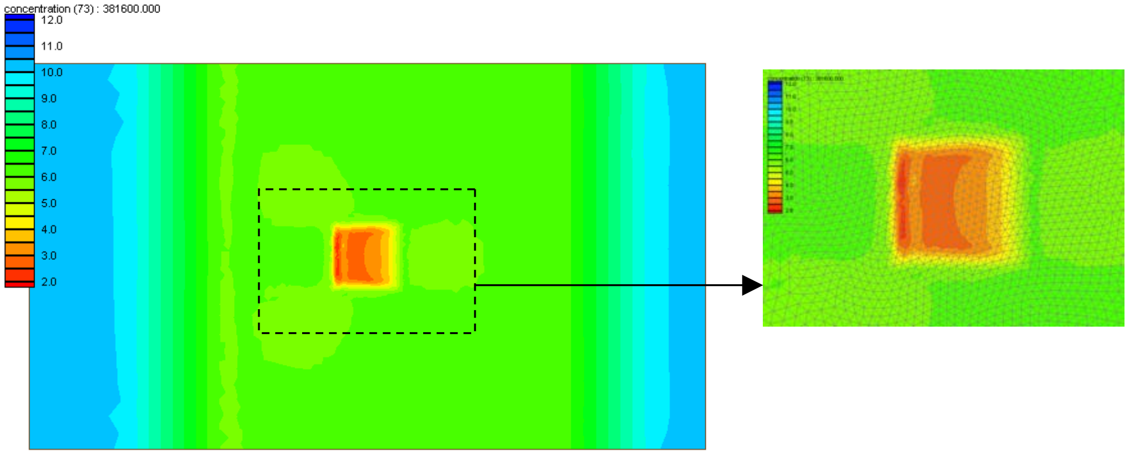

Structured (interpolated) grid

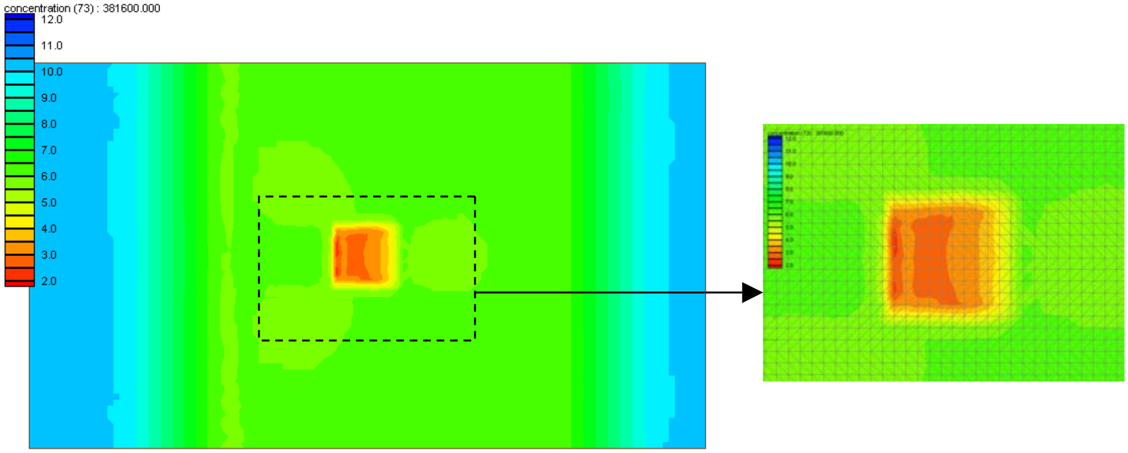

B.2.2. Case #2: RIVERINE

Purpose: Convert from 3D salinity output files from unstructured to structured grid
 # vertical layers: 9 layers

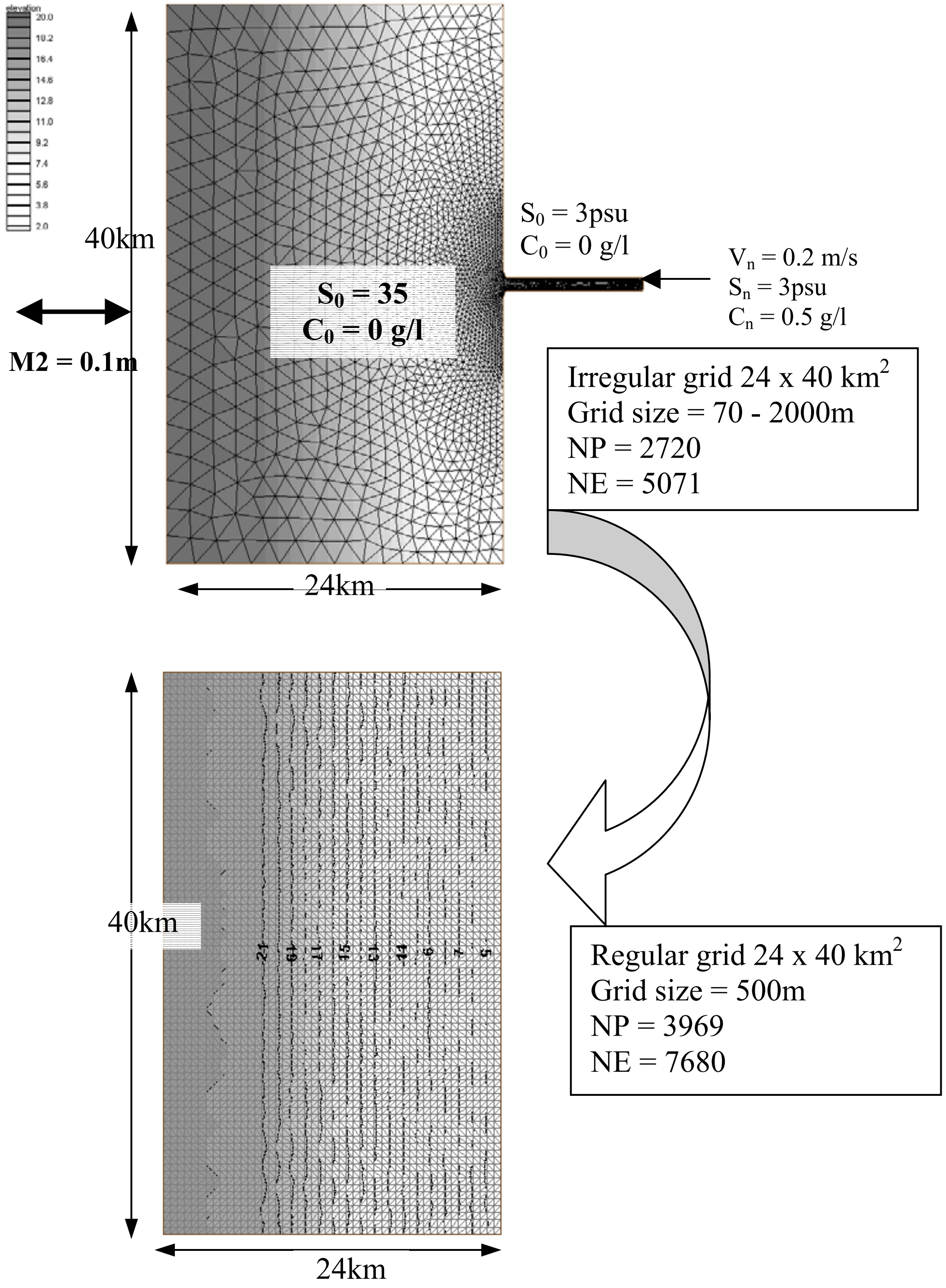

Near bottom ($\sigma = 2$)

Unstructured/Original grid → Structured /Interpolated grid

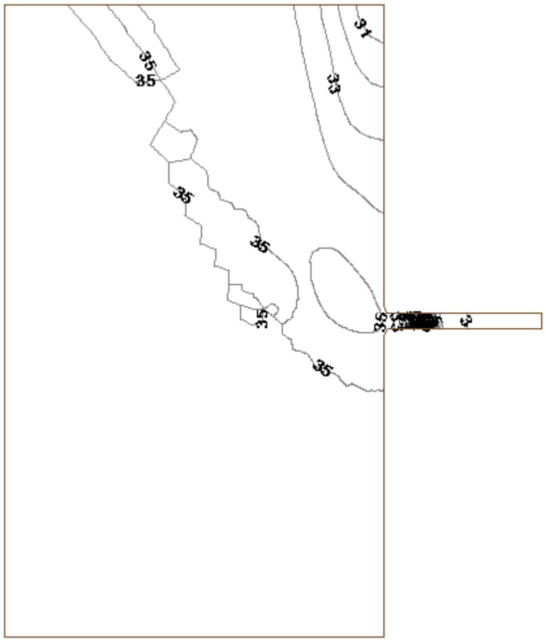

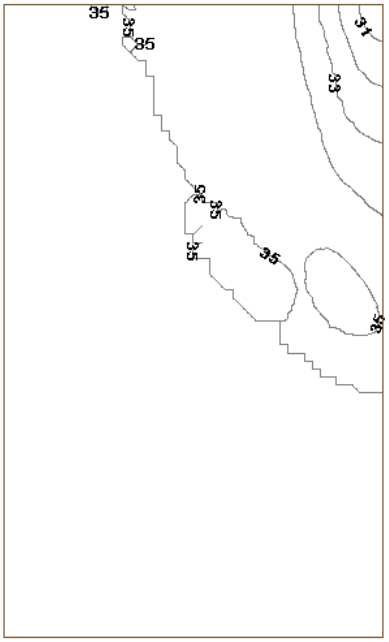

Near surface ($\sigma = 8$)

Unstructured/Original grid → Structured /Interpolated grid

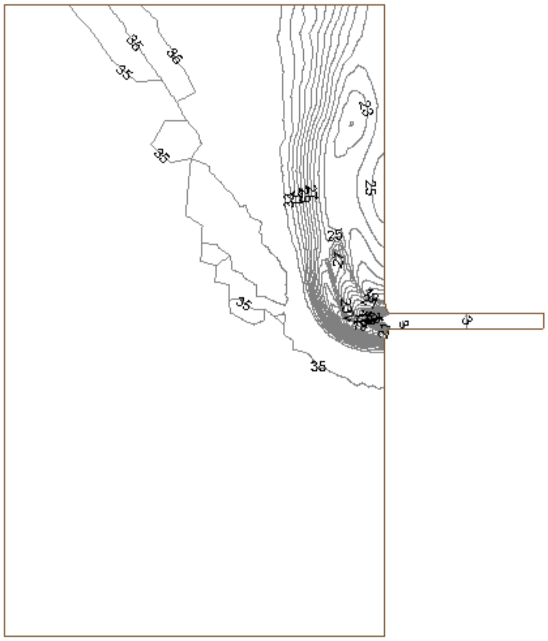

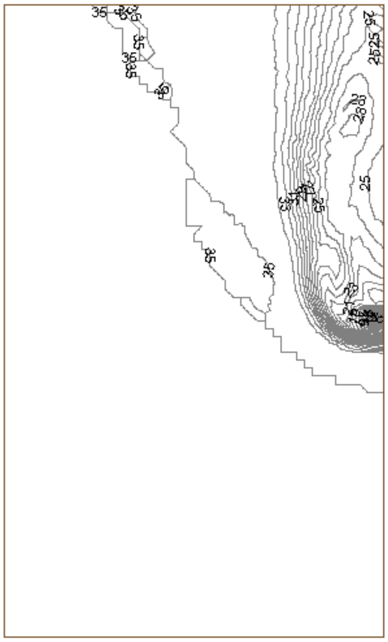

Surface ($\sigma = 9$)

Unstructured/Original grid → Structured /Interpolated grid

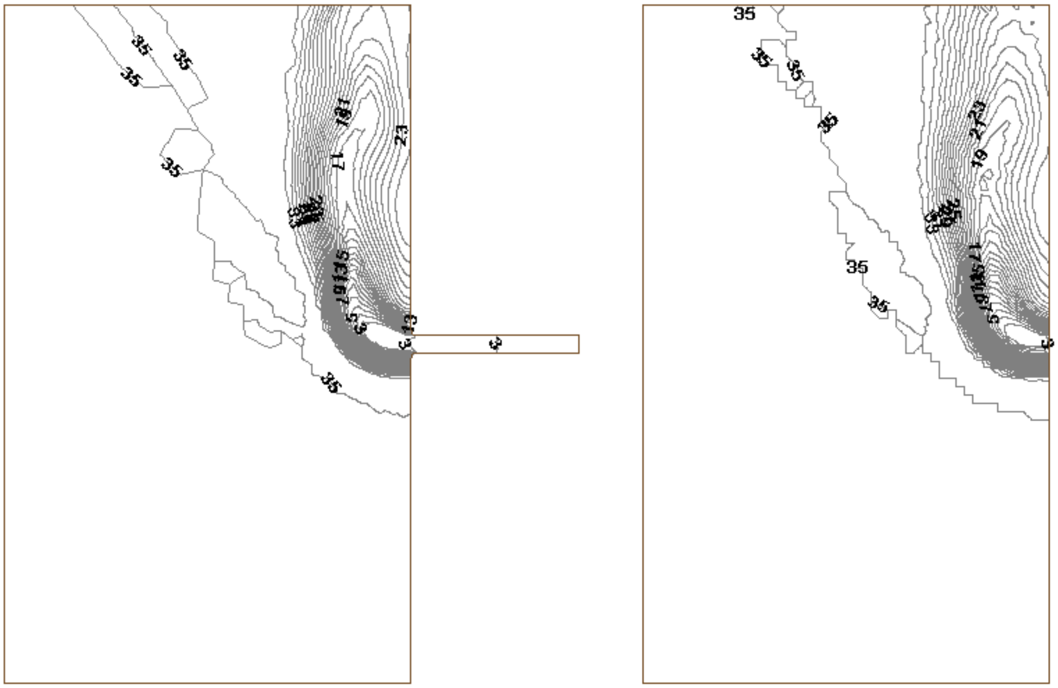

APPENDIX C

ANALYTICAL SOLUTION FOR HYDRODYNAMIC WITH CONSTANT AMPLITUDE FORCING AND WITHOUT ROTATION

Nomenclature:

j	imaginary unit = $\sqrt{-1}$
η	the amplitude of the water surface elevation
Ur	the amplitude of velocity component in radial direction
$\overline{U}$	depth-averaged velocity Ur.
ω	frequency of tide
h	bathymetric depth
E_v	eddy viscosity coefficient
τ	linear slip coefficient
k	bottom friction
K and λ	constants.

C.1. Lynch-Officer Analytical Solution (1985)

The analytical solution is applicable to the quarter annular test problem (QATP), where the variation occurs in the radial and vertical directions only, and hereafter is referred as Lynch and Officer (LO) analytical solution. There is no-flow boundaries at $r=r_1$, $\theta=0$, and $\theta=\pi/2$. Open boundary at $r=r_2$ is subject to periodic forcing M2 tide with an amplitude η. A linear slip condition is applied at the bottom based on the bottom velocity.

The linearized form of mass and momentum conservation, with Coriolis force neglected, are given as:

$$j\omega\eta + \nabla.\left(h\overline{U}\right) = 0 \qquad \text{(C-1)}$$

$$j\omega U_r + g\nabla\eta - \frac{\partial}{\partial z}\left(E_v \frac{\partial U}{\partial z}\right) = 0 \qquad \text{(C-2)}$$

The boundary conditions are enforced at the surface and at the bottom. In this case, the bottom stress is related to the average velocity.

$$E_v \frac{\partial U}{\partial z} = 0 \qquad \text{at } z = \eta \qquad \text{(surface)} \tag{C-3}$$

$$E_v \frac{\partial U}{\partial z} = \tau h \overline{U} \qquad \text{at } z = -h \qquad \text{(bottom)} \tag{C-4}$$

where:

$$\tau = \frac{E_v}{h^2}\left(\frac{\lambda^2 \tanh\lambda}{\lambda + \left(\frac{\lambda^2}{K} - 1\right)\tanh\lambda}\right) \qquad \text{C-5)}$$

The eddy viscosity E$_v$ and bottom friction k vary with h such that λ and K are constant; i.e. τ will be constant.

$$K = \frac{kh}{E_v} \qquad \text{and} \qquad \lambda = \sqrt{\frac{i\omega h^2}{E_v}} \tag{C-6}$$

Similar to the one example case in Muccino (1997) and Luettich et al. (2002), the values for K and λ are given as:

An M2 tide with frequency $\omega = 1.405 \times 10^{-4}\ \mathrm{s}^{-1}$ and amplitude $\eta = 0.1$m.

K = 2.836 and $\lambda = 9.206 + 9.206i$.

The eddy viscosity can be determined from Eq. (C-6) :

$$E_v = \frac{i\omega h^2}{\lambda^2} \text{ or } E_v = \Omega h^2 \tag{C-7}$$

with $\Omega = \frac{i\omega}{\lambda^2}$

The linear slip coefficient, τ, is computed using Eq. C-5. Thus, the bottom stress is expressed in terms of depth-averaged velocity and linear slip coefficient τ as:

$$\tau_b = \tau h \overline{U} \tag{C-8}$$

Based on the formulation above, the analytical solution for horizontal and vertical velocities as given in Lynch and Officer (1985), Muccino et al. (1997), or Luettich et al. (2002) and stated in σ-coordinate system are:

$$v(r,\sigma,t) = \mathrm{Re}\left\{v_o(r)\left[1-\delta\cosh(\lambda\sigma)\right]e^{i\omega t}\right\} \tag{C-9}$$

$$w(r,\sigma,t) = \mathrm{Re}\left\{\begin{array}{l} 2\gamma\alpha_1\delta\left[\left(\sigma\cosh(\lambda\sigma)+\cosh(\lambda)\right)-\dfrac{\delta\left[\sinh(\lambda\sigma)+\sinh(\lambda)\right]}{\lambda}\right] \\ +\gamma\alpha_2\left[\sigma+1-\dfrac{\delta\left[\sinh(\lambda\sigma)+\sinh(\lambda)\right]}{\lambda}\right] \\ +2\gamma\alpha_1\left[1-\delta\cosh(\lambda\right] \\ \end{array}\right\} \tag{C-10}$$

where:

$$v_o(r) = -\frac{g}{i\omega r}\left(s_1 A r^{s_1} + s_2 B r^{s_2}\right)$$

$$\sigma = z/h$$

$$\gamma = \frac{gh_o}{i\omega}\exp(i\omega t)$$

$$\alpha_1 = s_1 A r^{s_1} + s_2 B r^{s_2} \text{ and } \alpha_2 = s_1^2 A r^{s_1} + s_2^2 B r^{s_2}$$

$$\delta = \frac{1}{\cosh(\lambda)\left[1+\dfrac{\lambda}{K}\tanh(\lambda)\right]}$$

$$A = \frac{\eta_o s_2 r_1^{s_2}}{s_2 r_2^{s_1} r_1^{s_2} - s_1 r_1^{s_1} r_2^{s_2}}$$

$$B = \frac{-\eta_o s_1 r_1^{s_1}}{s_2 r_2^{s_1} r_1^{s_2} - s_1 r_1^{s_1} r_2^{s_2}}$$

$$s_1 = -1+\sqrt{1-\beta^2} \qquad \text{and} \qquad s_2 = -1-\sqrt{1-\beta^2}$$

$$\beta^2 = \frac{\left(\omega^2 - i\omega\tau\right)}{gh_o}$$

C.2. ADCIRC 3D Hydrodynamic Module Setup

Currently existing ADCIRC version provides three options for the bottom shear stress formulation (provided for x-axes only):

- ***ISLIP = 0*** (No-slip bottom b.c.)

The bottom stress τ_b is computed as $\tau_{bx} = E_v \left.\frac{\partial u}{\partial z}\right|_{z=-h}$

- ***ISLIP = 1*** (linear slip bottom b.c.)

$\tau_{bx} = KSLIP * u(z)_{z=-h}$

where: *KSLIP* = *KP*, and *KP* is specified in fort.15 file setup

- ***ISLIP = 2*** (quadratic slip bottom b.c.)

$\tau_{bx} = KSLIP * u_b$

where: $KSLIP = KP * \sqrt{u_b^2 + v_b^2}$

KP is specified on fort.15 file setup

To accommodate the comparison to the LO analytical solution, an additional ISLIP option was added into the ADCIRC 3D Hydrodynamic module:

- ***ISLIP = 3*** (linear slip bottom b.c.)

$$\tau_{bx} = KSLIP * \overline{U}_r \qquad \text{(C-11)}$$

where: $KSLIP = \tau.h$; thus, Eq. (C-11) resembles the Eq. (C-8)

Eddy viscosity for this ISLIP option is computed using Eq. (C-7).

VITA

Wahyu Widodo Pandoe was born in Bandung City, Indonesia, 29 July 1966. He received his B.Eng. degree in Geodetic Engineering from Bandung Institute of Technology (ITB), Bandung, Indonesia in April 1991. He has worked for the Indonesian government as a research assistant in Baruna Jaya Research Vessels Group of BPPT (The Agency for the Assessment and Application of Technology) Indonesia since 1992. He spent about 50-100 days per year as a scientist/engineer on board Baruna Jaya R/Vs conducting various oceanographic research and engineering surveys within the Indonesian seas.

He began his graduate studies at Texas A&M University in August 1998. He received his M.S. degree in physical oceanography in December 2000. He continued pursuing his Ph.D. program in the Ocean Engineering Division, Civil Engineering Department at Texas A&M University starting in January 2001, and received his Ph.D. degree in May 2004.

Wahyu Widodo Pandoe can be contacted through BPPT 1st Building, 18th Floor, Jl. M.H. Thamrin no.8, Jakarta, Indonesia 10340; phone: 62-21-316-8813 or 62-21-316-8818; email: wpandoe@bppt.go.id or wpandoe@hotmail.com.